Università Politecnica delle Marche

Biomolecular Sciences XXXIV cycle

Doctoral thesis

First Project

Structural and biochemical characterization of the aIF5A-DHS complex

Second Project

SARS-CoV-2 graphene biosensor based on engineered dimeric ACE2 receptor

Mattia D'Agostino

Tutor: Prof. Anna La Teana

Co-Tutor: Prof. Daniele Di Marino

2022

CONTENTS

List of Figures

Publications

D'Agostino M., Motta S., Romagnoli A., Orlando P., Tiano L., La Teana A., Di Marino D. (2020)
"Insights Into the Binding Mechanism of GC7 to Deoxyhypusine Synthase in Sulfolobus solfataricus: A Thermophilic Model for the Design of New Hypusination Inhibitors"
Front. Chem., 17 December 2020 https://doi.org/10.3389/fchem.2020.609942

Romagnoli A., Maracci C., D'Agostino M., La Teana A., Di Marino D. (2021)
"Targeting mTOR and eIF4E: a feasible scenario in ovarian cancer therapy"
Cancer Drug Resist 2021;4: http://dx.doi.org/10.20517/cdr.2021.20

D'Agostino M., Romagnoli A., Ardiccioni C., Maracci C., Motta S., La Teana A., Di Marino D. (2021)
"Control of the eIF4E activity: structural insights and pharmacological implications"
Cell Mol Life Sci. 2021;10: doi:10.1007/s00018-021-03938-z

D'Agostino M., Pavoni E., Romagnoli A., Ardiccioni C., et al. (2022)
"SARS-CoV-2 multi-variant graphene biosensor based on engineered dimeric ACE2 receptor"
Under revision on Science Advance

Oral presentations

1st MaSBiC-DiSVA Annual Symposium – Ancona (Italy)

"SARS-CoV-2 multi-variant graphene biosensor based on engineered dimeric ACE2 receptor"
D'Agostino M.

15/02/20-19/02/20

Posters

64th Annual Meeting of the Biophysical Society – San Diego (California)

"Insights into the binding mechanism of GC7 to Deoxyhypusine Synthase in Sulfolobus solfataricus: a thermophilic model for the design of new hypusination inhibition"
D'Agostino M., Motta, S., Romagnoli, A., Benelli D., Orlando P., Tiano L., Di Marino D., La Teana A.

60th Congress of the Italian Society of Biochemistry and Molecular Biology (SIB) – Lecce (IT)
"Characterization of the aIF5A-DHS protein complex"
D'Agostino M., Romagnoli A., La Teana A., Di Marino D.

Grants

20/09/21-20/12/21

Recipient of an EMBO Short Term Fellowship for the project "*Structural and biophysical characterization of the IF5A-DHS complex*"

FIRST PROJECT

Structural and biochemical characterization of the aIF5A-DHS complex

1 INTRODUCTION

1.1 The Translation Initiation Factor 5A

In 1976, a translation factor called IF-M2B was purified for the first time from rabbit reticulocytes (Kemper et al., 1976). IF-M2B was initially shown to be required for haemoglobin synthesis (Kemper et al., 1976). Later on, the name of IF-M2B was changed in Eukaryotic Initiation Factor 5A (eIF5A) to conform to the uniform nomenclature of initiation factors.

eIF5A is an abundant, small (17 kDa) and acidic protein of 157 amino acids, highly conserved in all three primary domains, with homologues in Archaea (aIF5A) and in Bacteria (EF-P). This initiation factor was shown to be essential in Eukarya and Archaea but not in Bacteria (Nishimura et al., 2010; Balibar et al., 2013; Gäbel et al., 2013; Zhang et al., 2019).

Two peculiarities render eIF5A an extremely interesting protein: 1. its conservation between Eukarya (including plants), Archaea and Bacteria (Wolff et al., 2007) which allocates the protein to the small group of universally conserved translation factors belonging to the primordial translation apparatus present in LUCA (Benelli et al., 2016); 2. its unique, unusual, and conserved post-translational modification called hypusination in Eukarya and Archaea (Park and Wolff, 2018a) and β-lysilynation in Bacteria (Bullwinkle et al., 2013) which is essential for the factor to perform its physiologically role in the cell (Turpaev, 2018; Tauc et al., 2021a). To date, eukaryotic translation factor 5A is the sole protein known to contain hypusine [Nε-(4-amino-2-hydroxybutyl) lysine], a unique polyamine-derived amino acid discovered in 1971 (Shiba et al., 1971). Hypusination consists in the conversion of a conserved lysine residue (Lys 50 in human eIF5A) into a nonstandard amino acid called

hypusine using spermidine as a substrate (Shiba et al., 1971; Park et al., 1981; Igarashi and Kashiwagi, 2018). Spermidine is a polyamine synthesized from putrescine, itself deriving from the urea cycle by the catalytic decarboxylation of ornithine (Igarashi and Kashiwagi, 2018). In Eukarya, the hypusination reaction is carried out by two different enzymes: deoxyhypusine synthase (DHS) and deoxyhypusine hydroxylase (DOHH) (Fig. 1).

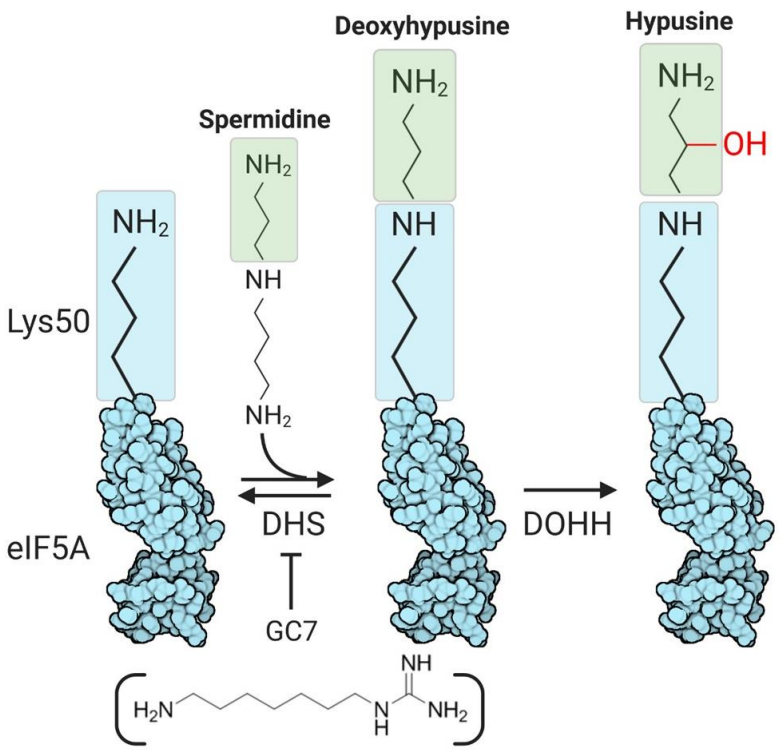

Figure 1 Scheme of hypusination reaction.

DHS is a homotetrameric protein consisting of four identical monomers of 41 kDa each (Liao et al., 1998). DOHH is a monooxygenase containing nonheme iron (two Fe^{II} atoms) (Wolff et al., 2007).

The first step of hypusine synthesis is represented by the covalent binding of diaminobutane, obtained by spermidine cleavage, to the ε-amino group of Lys329 of DHS with the formation of an imine intermediate. Diaminobutane is then transferred from DHS to eIF5A. This reaction step can be blocked by one of the most potent hypusination inhibitor, N1-guanyl-1,7-diaminoheptane (GC7) (Fig. 1).

At the final step of the hypusination, DOHH in the presence of O_2 and NADH hydroxylates deoxyhypusine with the formation of the active hypusinated form of eIF5A (Wolff et al., 2007).

The focus of this thesis will be concentrated mainly on the functional and structural characteristics of IF5A and DHS.

1.1.1 The role of the a/eIF5A in translation

At first, eIF5A was associated to the initiation phase of protein translation because it promotes the synthesis of methionyl-puromycin, indicative of a role in the formation of the first peptide bond (Benne et al., 1978). Nevertheless, the role for eIF5A as initiation factor has been questioned when it was shown that depletion of eIF5A in yeast caused only a minor decrease in the global protein synthesis rate (Kang and Hershey, 1994). Later on, Pelechano V. and colleagues (Pelechano and Alepuz, 2017) have shown that eIF5A is a key factor required for the translation of a subset of specific mRNAs. Other evidence that eIF5A is involved in the elongation step of the translation instead of in the translation initiation were gave by polysome profile analysis in yeast upon depletion of the gene. Saini P. and colleagues (Saini et al., 2009) have shown that a depletion of eIF5A in yeast resulted in the increase in ribosomal transit

times and an accumulation of polysomes. They also have demonstrated *in-vitro* an enhancing of rate of tripeptide synthesis after the addition of recombinant hypusinated-eIF5A. Moreover, eIF5A inactivation mimicked the effects of sordarin, an important eEF2 inhibitor, suggesting that eIF5A might work together with eEF2 to promote ribosomal translocation (Saini et al., 2009). Jao and Chen (Jao and Chen, 2006) also confirmed the interaction between eIF5A and a ribosome presenting a list of eIF5A-tagged interacting partners in which 14 out of 19 proteins are ribosomal proteins from either 40S or 60S. Their theory was that eIF5A binds 80S ribosome during the elongation phase of translation and this binding needs both RNA and the hypusinated-form of eIF5A (Jao and Chen, 2006). Indications of a function in translation elongation came from its bacterial ortholog EF-P which was shown to prevent ribosome stalling during the synthesis of proteins containing particular amino acid sequences, such as consecutive prolines (Doerfel et al., 2013). Considering this, Gutierrez and colleagues used *in-vivo* and *in-vitro* assays to reveal that eIF5A plays the same role as EF-P by promoting the elongation rate of specific proteins containing consecutive stretches of polyproline (Gutierrez et al., 2013). These sequences, in the absence of eIF5A, would cause a stalling of the ribosome because the constrained cyclic geometry of the proline side chain makes it a poor acceptor as well as a poor donor in the peptidyl transferase reaction. In 2016 two different model structures from cryo-EM (Schmidt et al., 2016) and X-Ray diffraction (Melnikov et al., 2016) of eIF5A bound to 80S yeast ribosome have shown that the protein binds to the E-site of the ribosomes and extends the hypusine-containing domain into the P-site where, interacting

with the tRNA CCA-end, it allosterically allows the formation of the proline-proline peptide bond (Fig. 2).

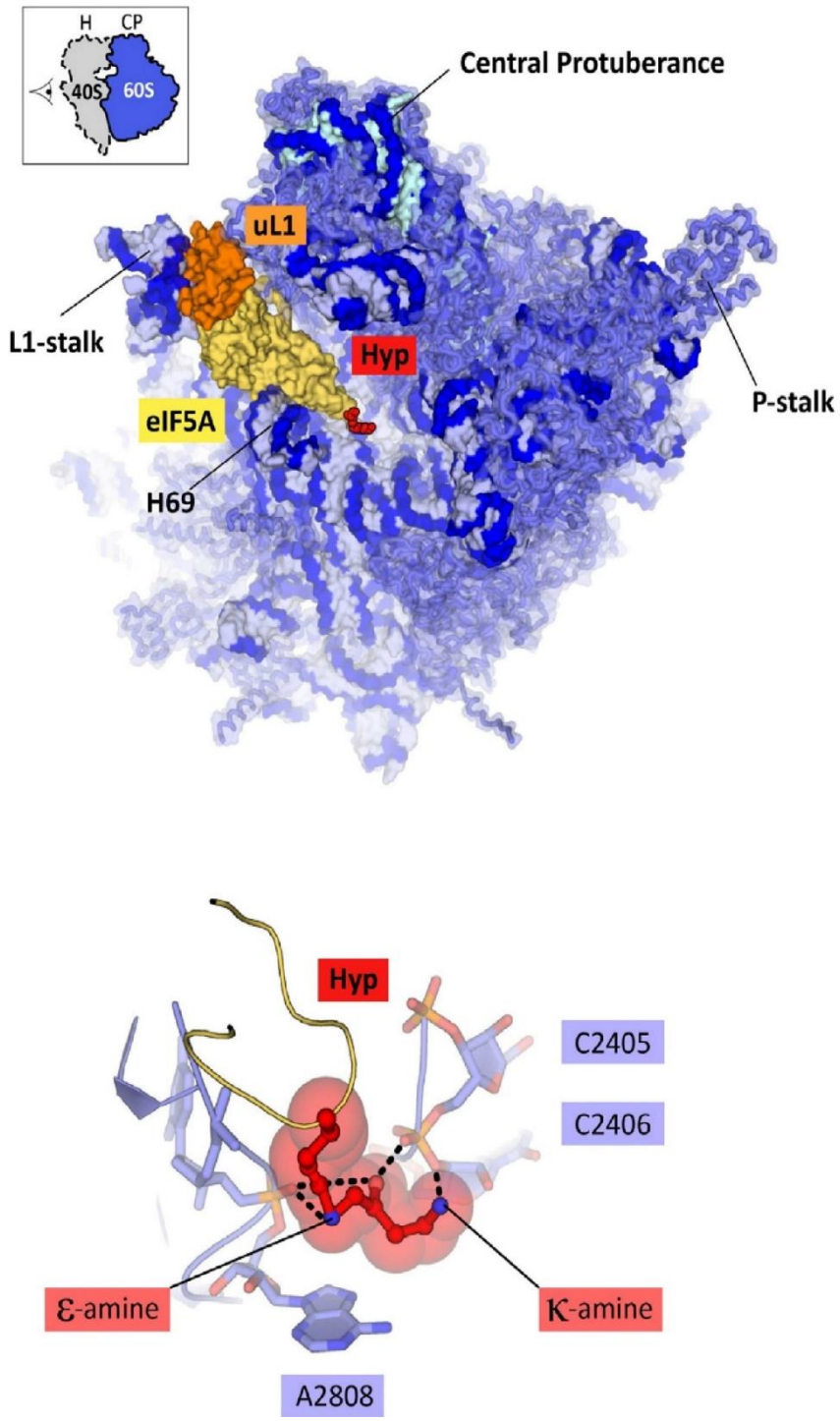

Figure 2 Electron density map reveals ribosome-bound eIF5A.

Views of the 80S ribosome/eIF5A structure. (upper), View of the 60S ribosomal subunit shows the eIF5A-binding site and eIF5A; (lower) The hypusine-binding site. The hypusine conformation is stabilized by extensive contacts with the 25S rRNA (Schmidt et al., 2016).

Successive studies have contributed to improve our knowledge on this factor by showing that eIF5A can facilitate peptide bond formation not only at polyproline stretches, but also at many other tri-peptide motifs (combination of aspartic acid, glycine, and other amino acids) (Park and Wolff, 2018b) and that, in addition to being involved in elongation, eIF5A participates also in the initiation and termination steps of translation. During the initiation phase, eIF5A is involved in controlling the fidelity of start codon selection (Manjunath et al., 2019) (Fig. 3). By studying the regulation of the growth-promoting gene MYC, the authors revealed that depletion of eIF5A gene increased upstream translation within 5′ untranslated regions in yeast and human transcriptomes, resulting in an enhanced production of an N-terminally extended protein (Manjunath et al., 2019). During the termination step, eIF5A improved the rate of peptidyl-tRNA hydrolysis mediated by eRF1 (Schuller et al., 2017) (Fig. 3).

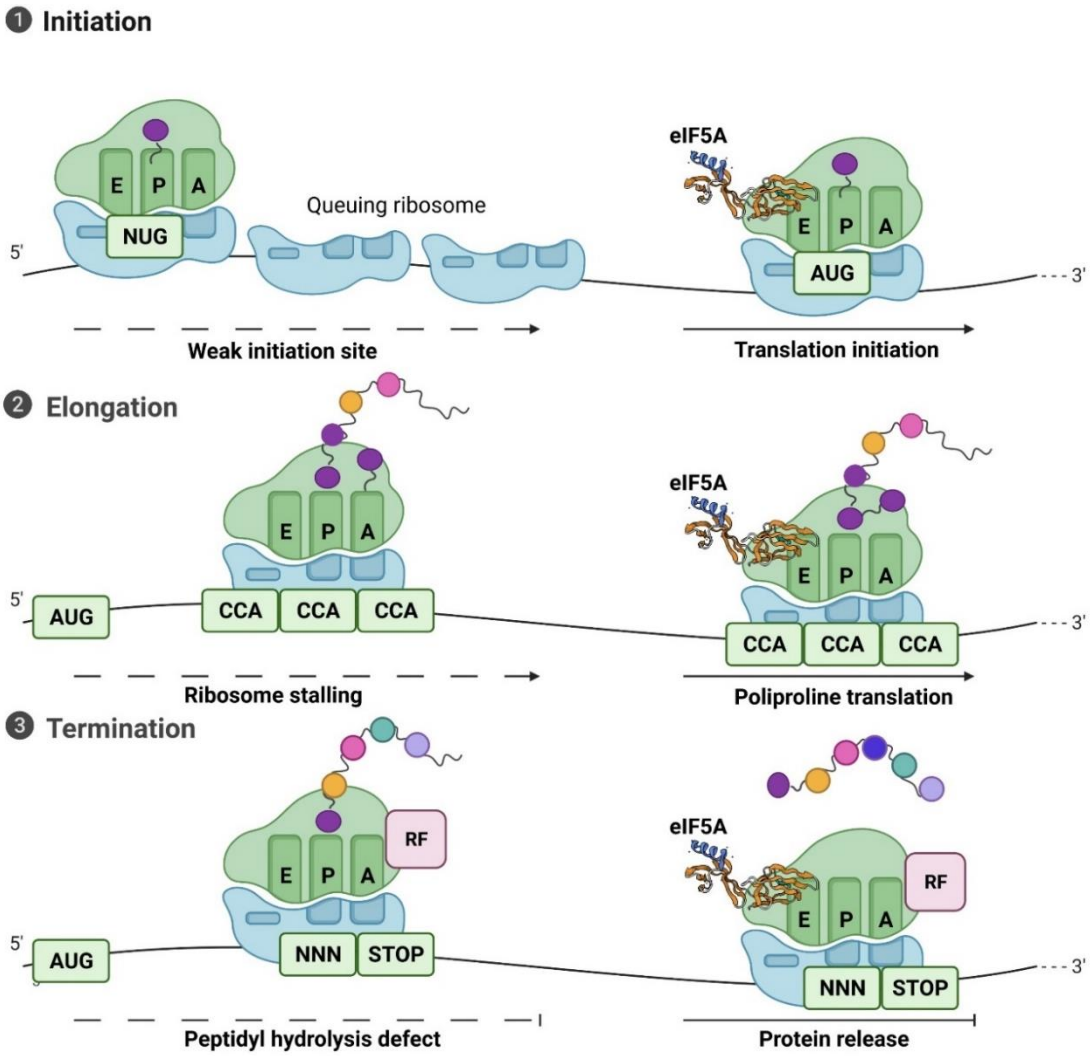

Figure 3 Different roles of eIF5A in translation.

(**1**) **Initiation.** Repression of ribosomal pausing by eIF5A is necessary to preserve the fidelity of start codon selection and thus maintaining efficient scanning and translation initiation. (**2**) **Elongation.** Without eIF5A, the stalled ribosomes obstruct scanning, and initiation at upstream leading to sub-optimal start codons (left). eIF5A is vital in elongation step of protein containing stretches of polyproline by preserving from ribosome stalling. (**3**) **Termination.** eIF5A contributes to translation termination at STOP codon by promoting peptidyl hydrolysis due to the release of factor activity (RF)

1.1.2 Other physiological roles of eIF5A

These last few years it was shown that eIF5A is implicated in other several physiological processes including metabolic adaptation (Levasseur et al., 2019; Turpaev et al., 2019), aging (Zhang et al., 2019; Liang et al., 2021), and immune cell differentiation (Luchessi et al., 2009; Parreiras-e-Silva et al., 2010; Tauc et al., 2021b). Concerning this last process, Puleston et al. (Puleston et al., 2019), in a recent study, analysed the role of polyamines in the differentiation of CD4+ TH cells into distinct subsets (TH1, TH2 and TH17 cells). They found that synthesis of hypusine through DHS triggers the core requisite for polyamine metabolism in controlling TH lineage fidelity. Moreover, eIF5A expression was confirmed at all mice embryonic post-implantation stages in regions which undergo active differentiation (Parreiras-e-Silva et al., 2010). Talking about metabolism, Cougnon et al. (Cougnon et al., 2021) described that hypusination inhibitor GC7 is able to decrease protein expression of the renal GLUT1 glucose transporter in cultured proximal cells causing a decrease of trans-cellular glucose flux. However, the reason why eIF5A can repress GLUT1 expression remains to be determined given that the GLUT1 protein sequence does not contains any polyproline motif and its mRNA sequence does not harbour the consensus sequence necessary to link eIF5A. eIF5A is shown to be involved also in apoptotic process but with controversial functions. It seems that the function of hypusinated eIF5A in apoptosis depends on the stress that the cells have to deal with. For example, GC7, that inactive eIF5A, has been demonstrated to have a synergistic effect on apoptosis together with the apoptotic inducer IFNα (Caraglia et al., 2003). On the contrary, it has an anti-apoptotic effect in renal cell in anoxia (Melis et al., 2017) due to a shift in

metabolism to anaerobic glycolysis and a mitochondrial alteration described by a drop in the expression of OXPHOS mitochondrial complexes. Interestingly, the modulation of OXPHOS was demonstrated to be related with hypusintaed eIF5A (Puleston et al., 2019).

In Archaea, more specifically in crenarchaeon *Sulfolobus solfataricus,* Bassani et al (2019) have indicated for the first time an endoribonucleolytic activity of the protein, opening to the possibility that aIF5A is a moonlighting protein (Bassani et al., 2019).

Taken together, all these data show that the Initiation factor 5A is an extremely interesting translation factor which is involved in several and different cellular functions.

1.1.3 Implications of eIF5A in pathological cellular processes

Human eIF5A exists in two isoforms, eIF5A1 and eIF5A2, that share 80% of their cDNA sequences and 94% of their amino acid sequences (Clement et al., 2003). eIF5A1 and eIF5A2 genes are located on different chromosomes (17p12-p13 and 3q25-q27 respectively). eIF5A1 is expressed in almost all cells and tissues (Clement et al., 2006), on the other hand, eIF5A2 is expressed mainly in testis, brain, and cancer cell lines (Wang et al., 2013; Mathews and Hershey, 2015). Moreover, both isoforms of eIF5A are overexpressed in many types of cancer (Mathews and Hershey, 2015), such as glioblastoma and adenocarcinomas (For review see Mathews and Hershey, 2015). In these pathological processes, the protein may promote cell proliferation facilitating the translation of specific, growth-promoting mRNAs, which support DNA replication and hyperproliferation of tumour cells (Slowinska et al., 1995).

eIF5A is also involved in many others pathological processes such as diabetes, malaria and HIV-1 infections (Bevec et al., 1996; Kaiser et al., 2007; Turpaev, 2018). Concerning HIV-1, eIF5A simplify the nucleocytoplasmic transport of viral mRNAs through the RRE (Rev responsive elements) or IRES (iron responsive elements) binding and excites their translation initiation events, contributing to human immunodeficiency virus type 1 replication (Bevec et al., 1996). Hypusinated eIF5A is also necessary for nuclear export and translation of iNos-encoding mRNA, which are crucial stages during the inflammatory damage of islet β cells in the diabetic disease; eIF5A depletion as well as the inhibition of hypusination through GC7 avoids hyperglycaemia in diabetic mice models (Maier et al., 2010).

1.1.4 Structural features of IF5A

Structurally, the human eIF5A is composed by two different domains: an N-terminal domain, where the hypusine residue is located; it is dominated by β-strands (denominated β1- β6), it is also present a one-turn 3_{10}-helix in the loop connecting β1 and β2; and a C-terminal domain consisting of a three-turn α-helix α2 and five strands β7-β11 (Tong et al., 2009) (Fig. 4). The hypusination site (Lys50) in the human eIF5A, is placed on the loop connecting β3 and β4. This hypusination loop is disordered. Interestingly, the C-terminal domain accommodate an OB-fold (oligonucleotide-binding fold), a five-stranded beta-barrel known to bind nucleic acids that might allow the protein to bind RNA.

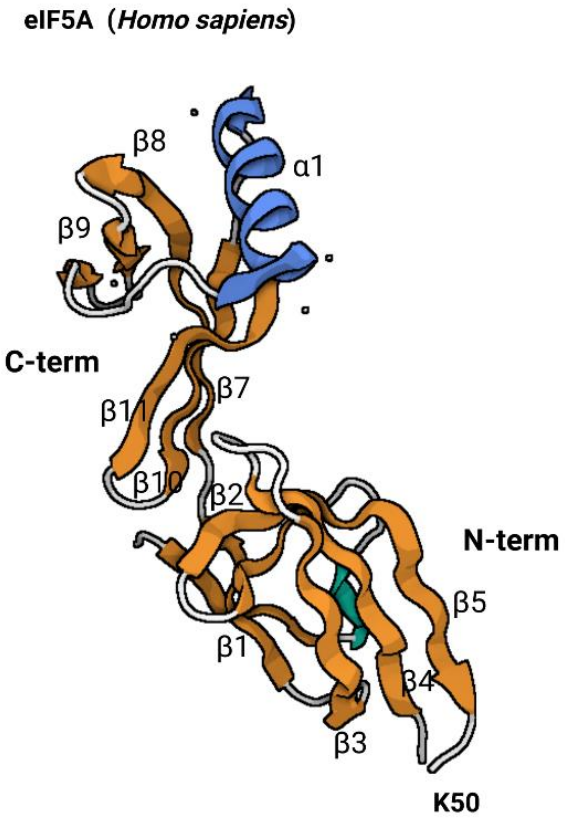

Figure 4 Structure of human eIF5A1.

Secondary structural elements are colored differently and labelled. The location of the specific lysine for hypusination is indicated (K50).

As said before, the sequence of eIF5A, as well as the structure, are extremely conserved among Eukarya and Archaea (Fig. 5). In addition, the ortholog EF-P shows a structural similarity with a/eIF5A, but with some divergences (Hanawa-Suetsugu et al., 2004). As shown in figure 5, eukaryotic (human) and archaeal (from *Pyrococcus horikoshii* and *Metanhococcus jannaschii*) IF5A share a very similar conformation in which, as described before, there are two different domains: the C-terminal domain and the N-terminal domain, site of hypusination region. On the other hand, EF-P consists of three β-barrel domains with a global shape that resembles the L-shape of the tRNA (Hanawa-Suetsugu et al., 2004) (Fig. 5). One arm of the L contains domain I and II, whereas the other one is formed by domain II and III. Fascinatingly, both N-terminal and C-terminal domain of the eukaryotic and archaeal IF5A have an identical topology of the N-terminal domain I and domain II of EF-P respectively (Fig. 5) and, these domains also share the same core flexibility. The alignment of the bacterial EF-P and the eukaryotic and archaeal counterpart 5A highlights that near the hypusinated lysine resides the highest conservation of amino acidic residues, but neither DHS nor DOHH homologs has been identified in bacteria (Clement et al., 2003). In bacteria, the β-lysinylation modification pathway, which, in some bacteria, replaces the hypusination, occurs in three steps and requires three enzymes YjeK, YjeA and YfcM (Navarre et al., 2010; Yanagisawa et al., 2010; Peil et al., 2012). Human eIF5A has a very similar structures compared to *Leishmania braziliensis* (1X6O) and Leishmania *mexicana* (1XTD) eIF5A (RMSD of 1.28Å for 129 a.a. residues and RMSD of 1.28Å for 131 a.a residues, respectively) in which the one-turn 3_{10}-helix is conserved (Tong et al., 2009). As described before, human eIF5A is also similar

to the structures of *Pyrococcus horikoshii* (1IZ6) and *Methanococcus jannaschii* (2EIF) (Fig. 5). aIF5A from *Pyrococcus horikoshii* is mainly composed of β-strands and includes two distinctive domains (Fig. 5), an N-terminal domain in which is present a SH3-like barrel, containing a 3_{10}-helix and a six-β-stranded anti-parallel β-sheets. This domain also contains a loop called L1, that includes residues 33-41, which carry a specific lysine (Lys37), that is supposed to be modified into hypusine, as it occurs in eukaryotes. On the contrary, the C-terminal domain, as well as the eukaryotic one, contains an OB-fold motif, consist of two short α-helices (α2- α3) and five stranded anti parallel ß-sheets. Taken together, all these crystal structures confirm once again the extreme conservation of IF5A among the three primary domains.

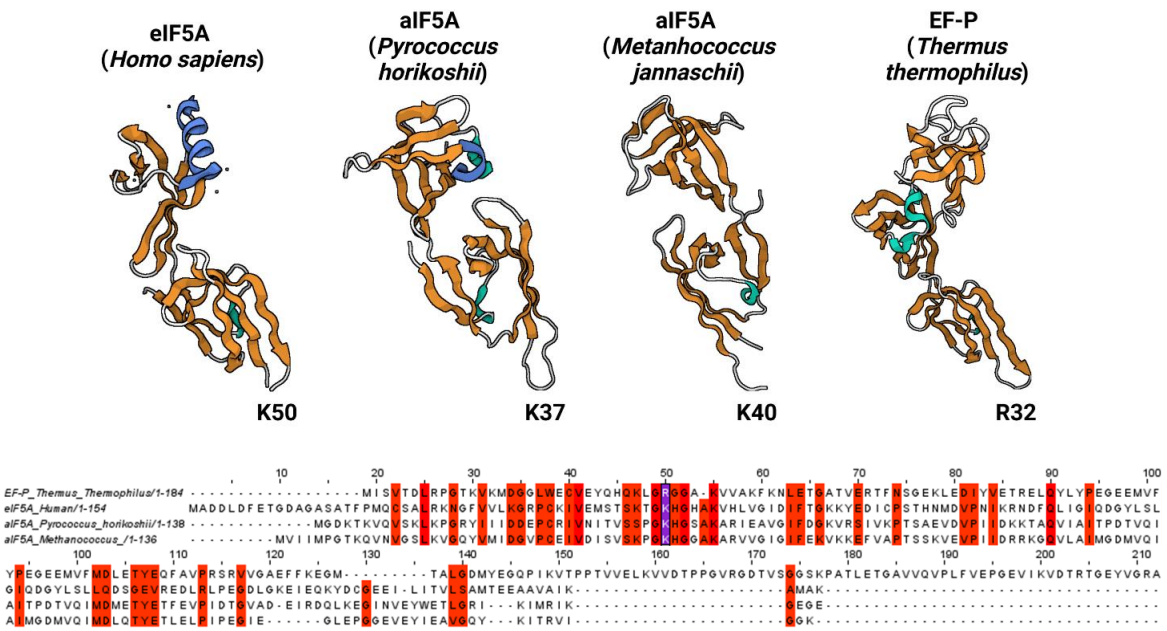

Figure 5 IF5A is conserved between Eukarya, Archaea and Bacteria.

(**upper**) Structural comparison of the eukaryotic eIF5A with two archaeal aIF5A and the bacterial elongation factor EF-P. Specific lysine residues that undergo hypusination are shown. (**lower**) Amino acid sequences alignment (CLUSTAL Omega) of 5A protein from *Homo sapiens*, *Pyrococcus horikoshii*, *Methanococcus jannaschii*. Modified lysines are highlighted in violet. Conserved residues are shown in red.

1.2 The Deoxhyhypusine Synthase

1.2.1 Function and role of DHS and implications in hypusination reaction

DHS is a cytosolic transferase involved in the hypusination process and is responsible of the first part of the reaction, the deoxyhypusination of the specific lysine. DHS is encoded by the *dhps* gene (located on chromosome 19) in humans (Jones et al., 1996). As well as hypusinated eIF5A, also DHS is essential. It was shown that the null mutation in the single copy of yeast *dhs* gene results in the loss of cell viability in *Saccharomyces cerevisiae* (Kang and Chung, 1999). DHS presents specificity for eIF5A and a very limited specificity toward spermidine and few of its closely associated molecules, such as homospermidine, aminopropyl cadaverine, cis- and trans-unsaturated spermidine, and N8-methyl- and N8-ethyl spermidines (Park and Wolff, 2018c). All the steps catalysed by DHS are reversible (Park et al., 2003). DHS exists as a homotetramer composed of four identical monomers of 41 kDa each. As well as the initiation factor 5A, also DHS is an extremely conserved protein, both in function and structure. The deoxyhypusine reaction has been studied in detail (Turpaev, 2018). It occurs in four different steps (Figure 6): in the first step, DHS catalyzes the formation of dehydrospermidine through the oxidation of spermidine in a NAD-dependent manner, resulting also in the formation of NADH (Wolff et al., 1990). In the second step, the dehydrospermidine is cleaved to produce diaminopropane, and the residual butyloamine moiety is linked to the DHS Lys329 through an imine bond (Joe et al., 1997). Interestingly, if the specific residue Lys329 is mutated this will lead to a totally inactive human enzyme (Joe et al., 1997; Umland et al., 2004). After eIF5A

recognition, the imine group is added to the -amino moiety of eIF5A Lys50 (in human). In the last step of the reaction, DHS catalyzes the reduction of the eIF5A Lys50 imine-intermediate to deoxyhypusine via NAD regeneration (Wolff et al., 1990).

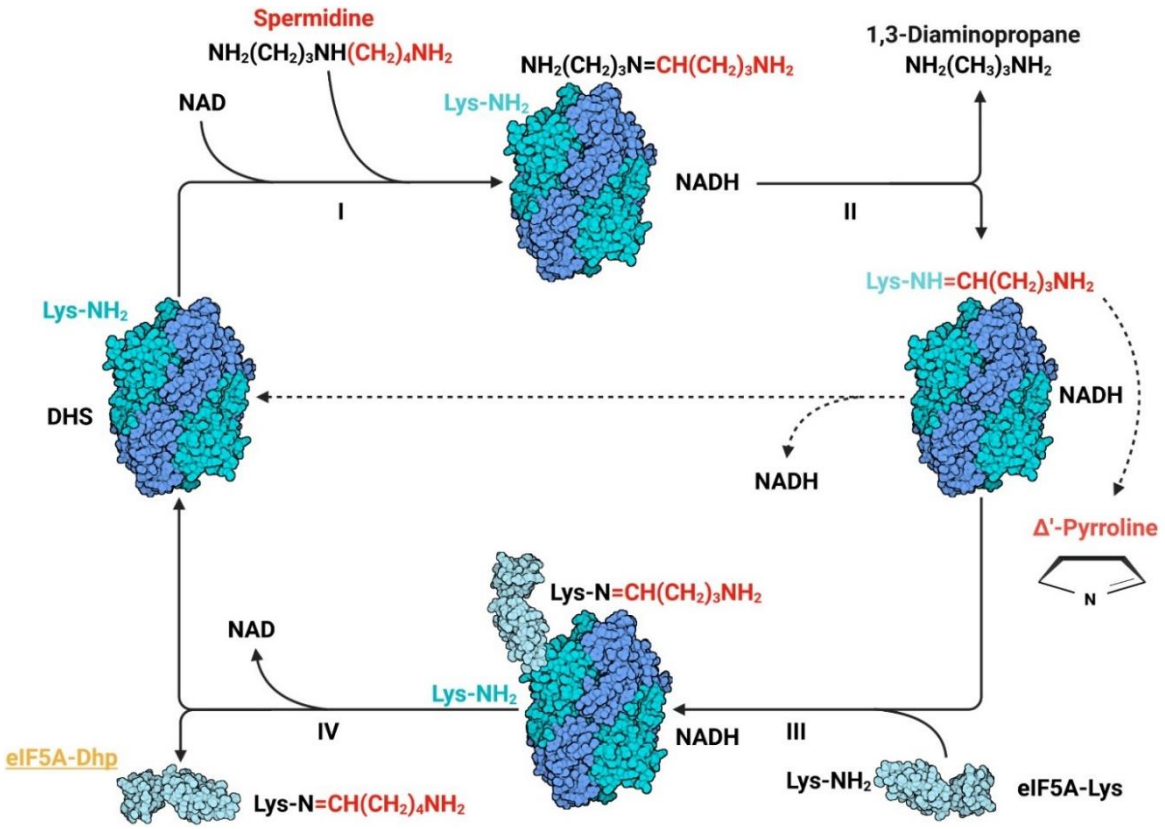

Figure 6 Schematic representation of the DHS reaction.

The reaction takes place in four steps (I–IV) to form deoxyhypusine in eIF5A. However, if eIF5A(Lys) is excluded, DHS catalyzes the cleavage of spermidine and generates 1,3-diaminopropane, Δ1-pyrroline, and NADH (dotted arrows).

Nevertheless, the full role and the mechanism of hypusination in archaea in unclear yet, there are evidence that DHS is essential also in these organisms (Jansson et al., 2000).

As already mentioned, the DHS is conserved among eukarya and between eukarya and archaea. In fact, *dhps* gene has been found in all archaeal genomes sequenced so far (Park and Wolff, 2018c), and modified aIF5A is supposed to be present in all archaeal organisms although with same variations, some contain the hypusinated version, while others only the deoxyhypusinated form and very few contain both versions of the protein (Park and Wolff, 2018c).

In our lab, Bassani et al (Bassani et al., 2018), has proved that aIF5A from the crenarchaeon *Sulfolobus solfataricus* is hypusinated. Moreover, the archaeal DHS (aDHS) shares with the human one 31 and 52% of amino acid identity and similarity, respectively. and it is shown that aDHS forms a complex *in-vitro* and *in-vivo* with aIF5A catalyzing the formation of deoxyhypusine in the ligand suggesting that the first step of hypusination modification is conserved in this organism (Bassani et al., 2018).

Also the enzymatic mechanism appears to be conserved, in fact a comparison of the different DHS structures shows that residues present in the active site of the enzyme, such as those involved in the interaction with NAD and spermidine, are conserved (Fig. 7) even though some archaea seem to present some peculiarities (Umland et al., 2004; Prunetti et al., 2016; Chen et al., 2020; Wątor et al., 2020).

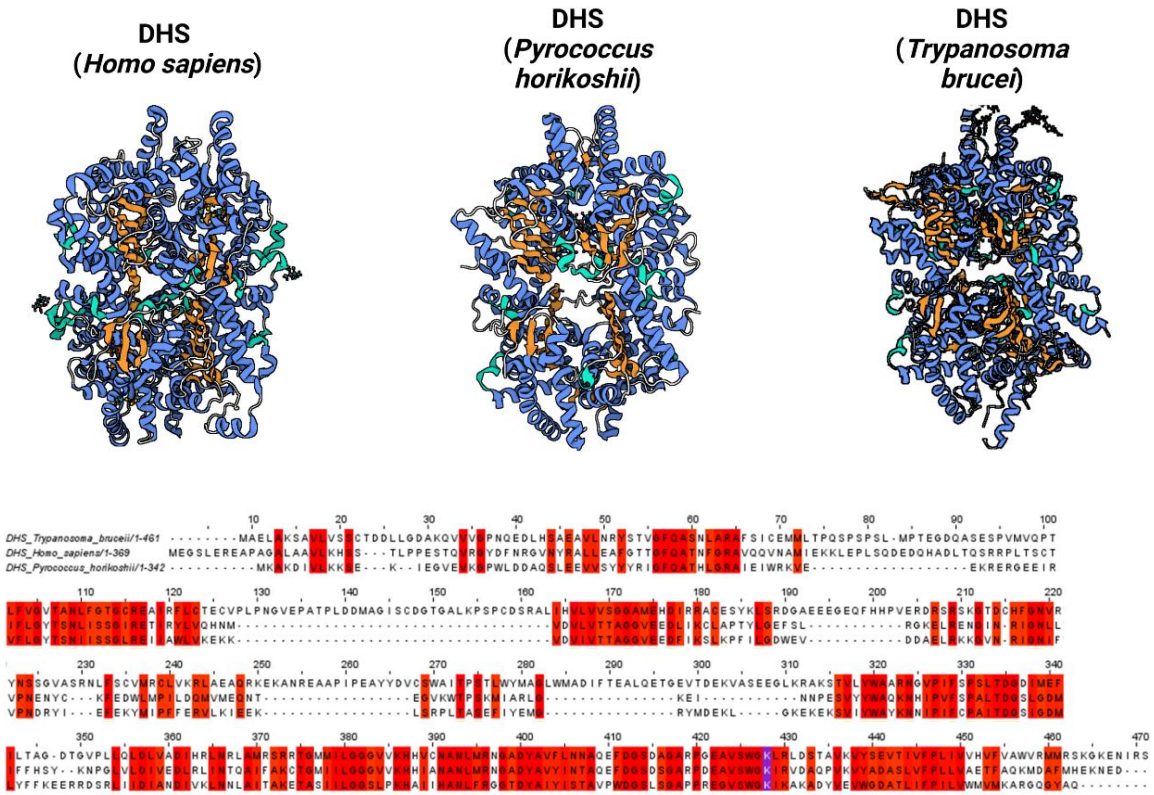

Figure 7 DHS is conserved between Eukarya and Archaea

(**upper**) Structural comparison of the eukaryotic DHS with *T. brucei* and *P. horikoshii* DHS; (**lower**) Amino acid sequences alignment (CLUSTAL Omega) of DHS protein from *Homo sapiens*, *Pyrococcus horikoshii* and *Trypanosoma bruceii*. Specific Lysine residues involved in hypusination are highlighted in violet. Conserved residues are shown in red.

1.2.2 Pharmacological molecules targeting DHS and hypusination reaction

Considering the involvement in several pathological conditions together with the high specificity and functional significance of the hypusination reaction, eIF5A, as well as the DHS and DOHH, have been designated as extremely interesting therapeutic targets. To date, different inhibitors of the two enzymes have been developed, while no molecule targeting enzyme-protein complexes are present yet. The most powerful inhibitor of hypsuination reaction is N1-guanyl-1,7-diaminoheptane (GC7) able to target the DHS during the first step of hypusination (Fig. 1). GC7 is a spermidine analogue composed by a guanidino moiety and an amino group. GC7 was described for the first time by Jakus and collegues (Jakus et al., 1993) who examined several spermidine analogues as potential inhibitors of DHS and found that GC7 had a Ki value around 10 nM, which is 400-fold lower than the Km of spermidine. GC7 therapeutic capacity has been widely tested through both *in-vitro* and *in-vivo* experiments. Although with excellent experimental results in different cell lines (Nakanishi and Cleveland, 2016; Schultz et al., 2018a; Martella et al., 2020) and tumour models, GC7 is not appropriately selective and have side effects or reduced bioavailability due to the presence of polyamine oxidases present in blood (Turpaev, 2018). It should be kept in mind that inhibiting hypusination, and therefore inhibit the activity of eIF5A will necessarily have various physiological collateral effects because, as described before, eIF5A regulates the expression of different mRNAs. Moreover, GC7 is a spermidine analogue and as such, it might influence the overall cellular polyamines pool (Pegg and McCann, 1982). GC7 effect was also investigated in Archaea and Bacteria

(Jansson et al., 2000). Interestingly, DHS enzyme from euryarchaeon *Haloferax volcanii* is not able to transfer the 4-aminobutyl moiety from spermidine to aIF5A and thus it is not inhibited by GC7 (Prunetti et al., 2016). In addition, in *Haloferax volcanii* the agmatinase enzyme may have a role in the hypusination modification pathway. Based on this, Prunetti L., and colleagues proposed a model in which the *Haloferax volcanii* DHS transfers directly the aminobutyl group from agmatine to aIF5A and the agmatinase enzyme lastly hydrolyzes the agmatine moiety of the mature deoxyhypusine protein. GC7 was also tested in different archaeal organisms and in *Escherichia coli* by Jansson et al (Jansson et al., 2000), providing further hints on the physiological role of the archaeal hypusinated aIF5A. They showed that GC7 was able to inhibit the growth of four different archaeal organisms, namely two *Sulfolobus* species (*acidocaldarius* and *solfataricus*), *Halobacterium halobium* and *Haloferax mediterranei* but not the growth of *Escherichia coli,* being devoid of the *dhps* gene.

These studies led the way to the characterization of IF5A and DHS using different models than eukaryotic ones, such as archaeal and bacterial systems that might offers easier and cheaper ways to study hypusination.

In addition to GC7, other hypusination inhibitors targeting both DHS and DOHH were also studied. Nishimura and colleagues (Nishimura et al., 2002) evaluated the antiproliferative effect of deoxyspergualin, a synthetic product of spergualin produced by *Bacillus laterosporus.* This molecule can inhibit the hypusination of eIF5A resulting in inhibition of cell growth, through the inhibition of DHS. However, to be effective deoxyspergualin needs high molar concentration (millimolar) and several days of incubation. Another molecule

targeting DHS is called CNI-1493 identified while looking for an antiretroviral therapy against HIV-1. In fact, as is written before, eIF5A has been described as a co-factor of the Rev pathway involved in HIV-1 replication (Bevec et al., 1996). Hauber et al. (Hauber et al., 2005) have shown that CNI-1493 suppressed the retroviral replication cycle in cultures of cell lines and primary cells through the inhibition of DHS. Concerning the inhibition of DOHH, the second enzyme involved in hypusination, the best characterized inhibitor agent is the antifungal Ciclopirox. This molecule blocks DOHH activity in the micromolar range by blocking the binding of DOHH to eIF5A (Abbruzzese et al., 1991).

In summary GC7 remains, to date, the most effective molecule in inhibiting the hypusination reaction and was also used in different DHS structures to structurally characterize the spermidine binding site of the enzyme (Umland et al., 2004; Wątor et al., 2020).

To now, there are no inhibitors able to target eIF5A-DHS complex. To reach this important goal will be fundamental to solve the three-dimensional structure of the eIF5A-DHS complex.

1.2.3 Structural features of eukaryotic DHS

The first DHS structure was resolved in 1998 by Liao et al. (Liao et al., 1998) showing for the first time the three-dimensional organization of the enzyme. DHS exists as a tetramer with four identical monomers (Fig. 8 A). Two of these monomers are tightly associated to form a pair of dimers, A1A2 and B1B2, with two active sites, located in each dimer interface for a total of four active sites. Each monomer comprises a central six-stranded parallel β-sheet, a small antiparallel β-sheet and 16 helices (Fig. 8 B). Close to the N-terminus of each monomer there is an insertion of 35 residues which consist of two helices, α2 and α3, with helix α3 packed parallel to the C-terminal helix α7. Between β2 and αC2 there is a group of helices (α4, α6 αB1, αB2 and αC1) grouped on the side of the parallel sheet on the opposite edge from the N-terminal tail (Fig. 8 B). A three-stranded antiparallel β-sheet (composed of strands βa, βb and βc) and helix α5 are incorporated between helix α4 and helix α6, located at the C-terminus of the parallel sheet. One part of this domain is part of the dimer interface containing two active sites. A very interesting feature of DHS is the buried nature of the active site which is accessible from the surface by a funnel about 16.4 Å long that it opens up into a long inner chamber (Fig. 8 C). The deoxyhypusine modification of eIF5A takes place within this site where it is present the Lys329 of the enzyme involved in the second step of the reaction (Fig. 1). Each active sites accommodate up to one NAD molecule and one spermidine. In this three-dimensional conformation each active-site entrance is blocked by a ball-and-chain motif composed of a region of extended structure covered by a two-turn α-helix. Liao and co-workers have made a great contribution in understanding most of details of DHS and hypusination,

however their conformation of the enzyme could be inactive due to the crystallization conditions (pH 4.5 and high salt concentrations). This has led in 2004, Umland and colleagues to apply different (and more physiologic) DHS crystallization conditions in order to describe the enzyme in active state (Umland et al., 2004). They obtained a new conformation (called Form II) crystal of the DHS grown at low ionic strength and pH 8.0, near the optimal pH for enzymatic activity. In this structure, each active site is no longer blocked by a ball-and-chain motif and two complete, but antiparallel active sites are present at each dimeric interface. In this work GC7 was used to mimic spermidine and to characterize its binding mechanism within the active site of the enzyme. Lys329 of human DHS was identify as the residue to which the butylamine moiety of spermidine is transferred in the second reaction step (Fig. 1 and Fig. 8 D). Structurally, the active site has been described in a similar way to the first DHS structure, that is contained within a deep narrow tunnel (about 17 Å long) present at a dimer interface. Concerning GC7, its guanidino moiety is positioned toward the bottom of the active-site tunnel, and its amino group is close to the tunnel entrance. Wator et al. (Wątor et al., 2020) in a very recent paper took a further step forward in characterizing the DHS three-dimensional structure. Their studies showed DHS in its apo form, as well as a detailed mode of binding of different polyamines, such as spermidine, spermine and putrescine. The structure from Wator and colleagues is the first one solved with spermidine in the active site. DHS, as well as for GC7, accommodates 4 different spermidine molecules, two for each the two neighbouring active sites cooperatively created by two DHS monomers. From this study it also emerged that DHS is able to bind other polyamines beyond the spermidine, such as

spermine and putrescine, although the latter is significantly shorter than the physiological substrate.

Among the various eukaryotic DHS structure, the one from *Trypanosoma brucei* (TbDHS) is quite interesting (Afanador et al., 2018). TbDHS is a tetramer but, differently from human enzyme, it is formed from two heterodimers which together form a shared active site with a single functional catalytic site per heterodimer.

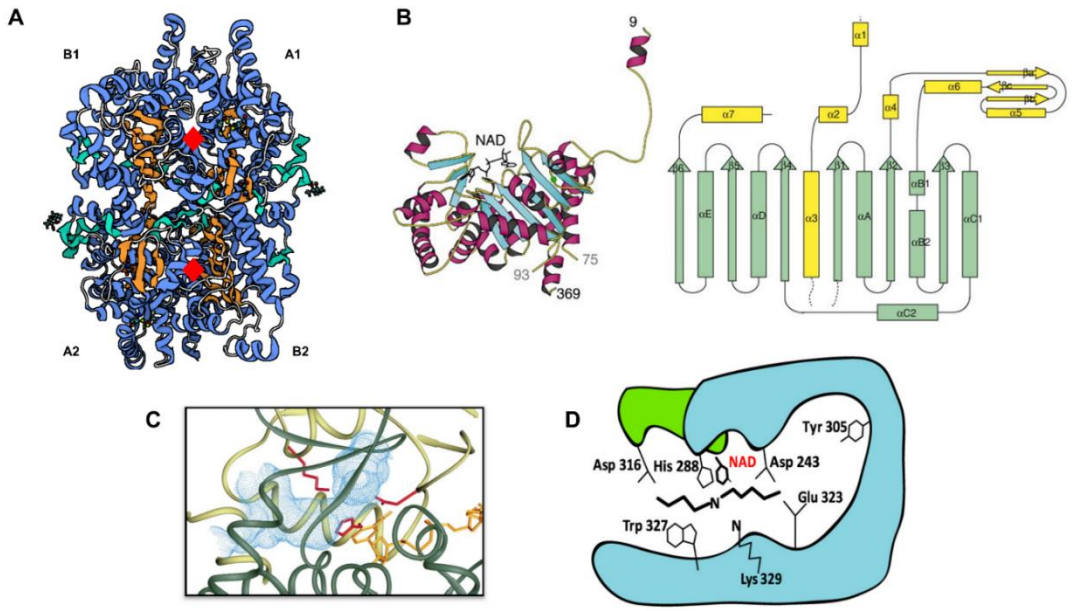

Figure 8 Deoxhyhypusine synthase and its active site.

(**A**) Crystal structure of tetramer DHS (PDB: 1DHS) with different monomer labelled; The red diamonds indicate the general location of the active sites; (**B**) Ribbon representation of the monomer of DHS with bound NAD (shown as a black stick model) and a schematic diagram of the secondary structure of the enzyme. DHS contains a Rossmann fold (shown in green) with insertions (in yellow) at the N and C terminus and between the second β-strand and the second α-helix of the Rossmann fold (Liao et al., 1998); (**C**) Dot surface of the active site tunnel. The two subunits are colored light and dark green; NAD molecule in in yellow and the Lys329 and His288 involved in hypusination in red (Liao et al., 1998); (**D**) Schematic representation of the active site of DHS with critical residues for catalysis (Lys329 and His288) and binding of spermidine (Asp243, Asp316, Glu323, and Trp327) (Park and Wolff, 2018a).

1.2.4 Structural features of archaeal DHS

The three-dimensional structure of the archaeal enzyme has been recently resolved. Chen et al. (Chen et al., 2020) have used *Pyrococcus horikoshii* DHS (PhoDHS) to characterized three different DHS conformations. In fact, they proposed a model in which DHS presents a dynamical structure at the NAD and spermidine binding site, with conformational changes that may be a consequence of variations in NAD concentration. More in details, DHS might be represented in three different conformational states: 1. Apo-form, before NAD binding; 2. Open-form with two NAD bound to two active sites waiting for the binding of the substrate; 3. reaction/closed form with all the 4 binding sites linked with as many NAD molecules (Fig. 9). Their proposed theory suggests that the conformational dynamics represents a mechanism by which DHS can respond to variations in cellular NAD concentration through IF5A modification.

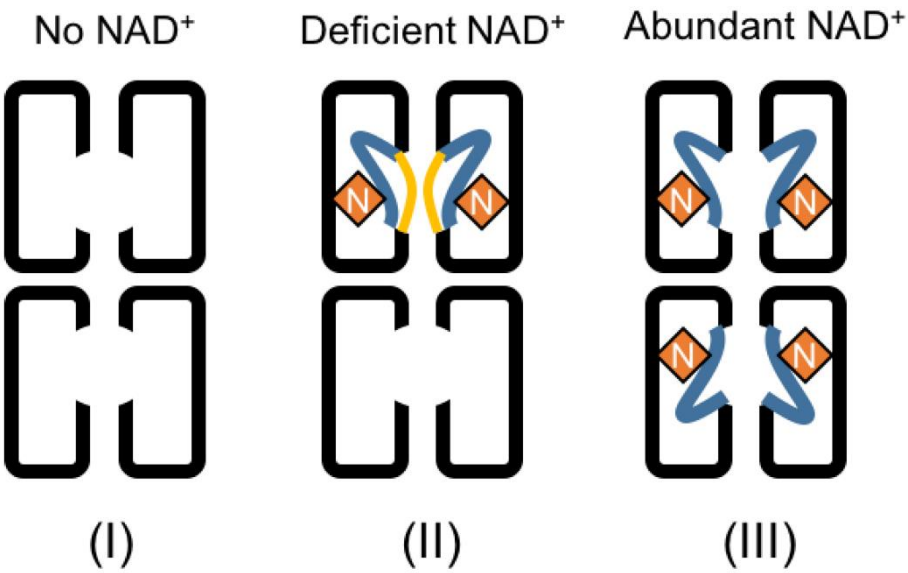

Figure 9 NAD-regulated conformational dynamics model of PhoDHS.

On the left, the **Apo-form** of DHS when there is no NAD+ binding to DHS**;** on the middle, **Open-form** with two NAD bound to two active sites waiting for the binding of the substrate; on the right, **reaction/closed form** with all the 4 binding sites linked with as many NAD molecules (Chen et al., 2020).

All DHS structures solved so far have allowed to understand many details of the hypusination reaction. However, to fully characterize this important feature of the initiation factor 5A and its relationship with the DHS enzyme and in order to design new hypusination inhibitors able to target in a more specific way the reaction and/or the interaction between eIF5A and the enzyme, it will be fundamental to solve the IF5A/DHS three-dimensional structure. This very challenging goal was the first aim of my PhD.

2 AIM of the work

Since the demonstration of its involvement in cell proliferation, eIF5A has been examined mainly in relation to the development of cancers in which it might be highly expressed. However, an increasing number of studies states that eIF5A is involved in several other disease such as diabetes, malaria and HIV-1 infections. Due to its involvement in physiological processes, as well as its very special and unique post-translational modification, eIF5A became an important and promising therapeutic target stimulating the design and development of inhibitors able to target the hypusination process, including DHS that is the first enzyme involved in this reaction. GC7, a spermidine analogue, is the most potent DHS and then hypusination inhibitor, with a Ki of 10 nM, which is ~500 times lower than the Km of the physiological spermidine. Several studies have confirmed the extremely effectiveness of the molecule on different types of cancer cell lines. However, GC7 and all currently known DHS inhibitors are not sufficiently selective and have side effects or limited bioavailability. In order to open new roads in the drug design and then find new specific inhibitors of eIF5A, a more in-depth structural and biochemical characterization of the protein, as well as of the hypusination path is strictly required. Moreover, an important lack for the discovery of new inhibitory molecules is certainly the absence of the three-dimensional structure of the eIF5A-DHS complex that is an essential prerequisite for success in drug design.

Before COVID-19 pandemic changed everyone's lives, the deep structural and biochemical understanding of IF5A in relationship with the DHS, was precisely the starting AIM of my PhD, or at least of the first part.

3 MATERIALS AND METHODS

3.1 Expression and purification of recombinant S. solfataricus aIF5A in E. coli

The gene coding for *S. solfataricus* IF5A (ORF Sso0970) was cloned into pMCSG7 expression vector using Ligation Independent Cloning (LIC). LIC is an alternative technique to restriction enzyme/ligase cloning that uses the 3' → 5' exo activity of T4 DNA Polymerase to create overhangs with complementarity between the vector and insert.

ORF Sso0970 was PCR amplified using primers suitable for LIC cloning, (Forward: 5'-TACTTCCAATCCAATGCCGCATAACGTACACG-3'; Reverse: 5'-TTATCCACTTCCAATGCTTAACCCTAACTATT-3'; underlined regions represent LIC tails). 50 ng of genomic DNA was used as a template for the PCR, performed with KOD Hot Start DNA Polymerase (71086 Sigma-Aldrich) and 0.3 μM primers were added to the reaction mixture. The amplification product, purified with the PCR purification kit (Quiagen), was treated with T4 DNA polymerase (0.0375 Units/μl final) in a 10× Buffer 2 (New England Biolabs) in the presence of dCTP (2.5 mM) to produce the LIC overhang. The reaction was performed at 22°C for 60' and then the enzyme was inactivated at 75°C for 20°. In parallel, the vector (150 ng) was linearized with NdeI and gel purified. Subsequently, the vector, similarly to the insert, was incubated with T4 DNA polymerase but in the presence of dGTP (as opposed to dCTP of the insert). Then, 2 μl of vector (30 ng) and 4 μl of insert (60 ng) were combined and incubated at 20°C for 60' to perform the annealing. Finally, 2 μl of this annealing mix was used to transform Escherichia coli ROSETTA (DE3)/ pLysS cells.

The cloned 5A gene encoded a protein that consists of the full-length initiation factor plus six histidine residues in the N-terminal position, a peptide linker of ten amino acids and the specific cleavage site (ENLYFQ) for the Tobacco Etch Virus (TEV) protease.

One of the positive colonies was inoculated in 2 l LB medium containing 34 μg/ml chloramphenicol, 100 μg/ml ampicillin and grown at 37 °C until an OD600 of 0.7, then the culture was induced by adding 0.5 mM IPTG. After 4 hours cells were harvested, pelleted, resuspended in 20 ml of lysis buffer (50 mM Tris-HCl pH 7.8, 150 mM NaCl, 15 mM imidazole, 1mM PMSF, 10 μg/mL DNase I, 25 μg/mL lysozyme).

Cells were lysed by sonication and the lysate was clarified by centrifugation at 100.000 g for 40 min at 4°C.

The supernatant was loaded into pre-equilibrated PROTINO Ni-NTA column (Macherey-Nagel) installed on ÄKTA start chromatography system to allow the binding of the His-tagged aIF5A. The lysate and the beads were washed with washing buffer (50 mM Tris-HCl pH 7.8, 500 mM NaCl, 40 mM imidazole) until the absorbance signal (A_{280}) has reached the baseline. Then, aIF5A was eluted in 4 ml elution buffer (50 mM Tris-HCl pH 7.8; 150 mM NaCl; 250 mM imidazole) and the eluted protein digested using TEV protease to remove the His-tag. The TEV protease was added in a 1:50 ratio (TEV/aIF5A) and they were incubated overnight at 4°C. Therefore, the cleaved protein was purified again using PROTINO Ni-NTA column that has held the TEV and the HIS-tag tails in excess.

Purified aIF5A was dialyzed overnight at 4 °C in dialysis buffer (50 mM Tris-HCl pH 7.8, 150 mM NaCl) and collected in small aliquots.

All the steps were analysed by SDS-PAGE, followed by coomassie-blue staining.

3.2 Expression and purification of recombinant *S. islandicus* DHS from *E. coli*

ORF M1627_1306 was amplified by PCR using 100 ng genomic DNA of *S. islandicus* using following primers:

forward
5'AAAAGCATGCGCATAAATAGAGAGGACTTGTTAAAAAACCC3'
(SphI restriction site)
reverse 5'AAAAGGATCCGCTTAATAAAGACGCGGCCAAAATAGG3'
(BamHI restriction site).

Amplified ORF was cloned in the plasmid pQE-70 (Quiagen) which adds a C-terminal His-tag to the recombinant protein.

The C-terminal His-tagged DHS protein was purified with the same protocol described above, except for the TEV cleavage, impossible to perform with this expression plasmid.

The purified protein was dialyzed against DHS dialysis buffer (50 mM Tris HCl pH 8.5, 500 mM NaCl, 80 mM Imidazole, 10% Glycerol).

3.3 Size-Exclusion chromatography

Recombinant aIF5A and DHS were loaded in different formulation on 3 ml Superdex 200 increase 5/150 GL Tricorn column (GE Life Science) to identify the complex formation between the two proteins. BSA (67 kDa), lactate-dehydrogenase (140 kDa) and myoglobin (17 kDa) were used as mass standard proteins, each at a concentration of 1 mg/ml. The chromatographic buffer formulation was 50 mM Tris-HCl pH 7.4, 150 mM NaCl. The column was

equilibrated with 3 volumes of buffer, then 0.25 mg/ml of different aIF5A preparations and 0.5 mg/ml of DHS were pre-heated at 65°C for 10 min and centrifuged at 10000 g for 10 min and finally they were separated on a size-exclusion column using 1.5 volumes of buffer (4.5 ml).

3.4 Native polyacrylamide gel

Purified recombinant aIF5A (5 μg, 300 pmol), DHS (10 μg, 80 pmol) and a mixture of aIF5A-DHS in a molar ratio of 0.5:1 (35 pmol:70 pmol) were subjected to 10% Native Polyacrylamide gel (Native-PAGE) after the addition of native gel sample buffer 6x (187.5 mM Tris HCl pH 8.8, 75% glycerol, 3% bromophenolblue). The gel was prepared as described (Weydert).

Polyacrylamide Gel was in 25 mM Tris base, 192 mM glycine running buffer at 150 V for 120 minutes at RT after a pre-run of 30 minutes at the same conditions. Proteins were visualized through Comassie Brilliant Blue staining.

3.5 Dynamic light scattering

After each purification, solubility of purified proteins was checked through Dynamic light scattering (DLS). DLS experiments were carried out with a DynaPro NanoStar (Wyatt Technology) dynamic light scattering instrument at 30°C and 65°C with protein concentration of 20 mg/ml for aIF5A, 2 mg/ml for DHS, 0.4 mg/ml for 6xHis-aIF5A-DHS complex and 7 mg/ml for aIF5A-DHS complex, using a laser wavelength of 780 nm and a scattering angle of 90°.

3.6 Isothermal Titration Calorimetry

ITC measurements were performed at 30°C on a MicroCal PEAQ-ITC (Malvern Panalytical). The buffer was composed by 50 mM Tris/HCl pH 8.5,

150 mM NaCl, 50 mM Imidazole, 10% Glycerol. A low amount of imidazole was added to correctly maintain the solubility of DHS. In a typical experiment, aliquots of 350 μM of aIF5A were injected into a 35 μM DHS present into the sample cell. The duration of each injection was 10 s and the delay between injections was 120 s. ITC titration curves were analyzed using the software AFFINImeter (Santiago de Compostela. Spain). The titration curve of kcal mol^{-1} vs. molar ratio (ligand/sample) is produced by the integration of each heat pulse with time and normalized for concentration. Standard free energies of binding and entropic contributions were obtained, respectively, as $\Delta G = -RT \ln(Ka)$ and $T\Delta S = \Delta H - \Delta G$, from the Ka and ΔH values derived from ITC curve fitting.

3.7 aIF5A-DHS Complex Purification

In order to find the best conditions for protein complex purification we have set up different protocols

3.7.1 Protocol A

We develop a system to purify the aIF5A-DHS complex through the exploitation of his-tag present on DHS C-terminus. Briefly, we have incubated an excess of recombinant aIF5A without His-tag with recombinant 6xHis-DHS (molar ratio 6:1; aIF5A:DHS) in a thermoshaker for 30' at 30°C (same temperature of ITC experiments) to facilitate the protein-protein complex formation. The binding buffer was composed of 50 mM Tris/HCl pH 8.5, 200 mM NaCl, 50 mM Imidazole, 5% Glycerol. After that, the sample was loaded into a pre-equilibrated Protino Ni-NTA column using AKTA chromatography system. The beads were washed using a wash buffer composed of 50 mM

Tris/HCl pH 8.5, 150 mM NaCl, 50 mM Imidazole and then the bounded complex was eluted using 50 mM Tris/HCl pH 8.5, 150 mM NaCl, 250 mM Imidazole. After an O.N. dialysis against a storage buffer (Tris-HCl pH 8.5 50 mM, NaCl 150 mM, Imidazole 50 mM, Glycerol 10%) the purified complex was tested using DLS. All purification steps were checked through SDS-PAGE.

3.7.2 Protocol B

In order to obtain a purified DHS-aIF5A complex without His-tags, we develop a second purification protocol. pQE70 plasmid does not contain a protease cleavage-site so it would be impossible to remove the His-tag. To overcome this issue, we have used the QuickChange site-directed mutagenesis method to introduce a Stop codon (TAA) in the region before the sequence coding for the 6xHis-tag.

The following primers were used for the mutagenesis and themutated nucleotides are shown in red:

Forward: 5'-GGCCGCGTCTTTATTAAGCTAATCCAGATCTCATCACCATC-3'

Reverse: 5'-GATGGTGATGAGATCTGGATTAGCTTAATAAAGACGCGGCC-3'

Two different *E. coli* cultures carrying the two recombinant plasmid (for DHS and 6xHis-aIF5A) were induced with IPTG. For DHS, 2 l of LB medium containing 100 µg/ml ampicillin were inoculated and grown at the same conditions of aIF5A culture, then the culture was induced by adding 1 mM IPTG. After 4 hours both cultures were harvested and centrifuged together to

obtain a single pellet. After that, the pellet was resuspended in 20 ml of lysis buffer (50 mM Tris-HCl pH 8.5, 150 mM NaCl, 15 mM imidazole, 1mM PMSF, 10 μg/mL DNase I, 25 μg/mL lysozyme).

Cells were lysed by sonication and the lysate was clarified by centrifugation at 100.000 g for 40 min at 4°C.

The supernatant was loaded into pre-equilibrated PROTINO Ni-NTA column (Macherey-Nagel) installed on ÄKTA start chromatography system to allow the binding of the His-tagged aIF5A and DHS bound to it. The beads were washed with washing buffer (50 mM Tris-HCl pH 8.5, 150 mM NaCl, 40 mM imidazole) until the absorbance signal (A280) has reached the baseline. Then, 6xHis-aIF5A-DHS complex was eluted in 4 ml elution buffer (50 mM Tris-HCl pH 7.8; 150 mM NaCl; 250 mM imidazole) and the eluted sample digested using TEV protease to remove the His-tag on aIF5A. The TEV protease was added in a 1:50 ratio (TEV/complex) and they were incubated overnight at 4°C. Therefore, the cleaved complex was purified again using PROTINO Ni-NTA column to remove the TEV and the HIS-tag tails in excess. Finally, the sample was concentrated with Amicon Ultra 10 kDa, to a final volume of 500 μL and loaded into a Superdex 200 10/300. The column was equilibrated with 3 volumes (75 ml) of buffer (50 mM Tris-HCl pH 8.5, 150 mM NaCl, 10% Glycerol), then 500 μl of sample were centrifuged at 10000 g for 10 min and then separated on column using 1.5 volumes of buffer (40 ml) with a flow rate of 0.3 ml/min. Positive peaks were recovered and subjected to SDS-PAGE and comassie staning. MW standards were from Bio-Rad (1511901).

3.8 Crystallization and data collection

Preliminary crystallization trials were performed using a crystallization screening kit from Hampton Research (Index, Natrix and PEG/ION kits). A crystallization drop containing 100 nL of protein solution recovered after ITC analysis (7 mg/ml), and 100 nL of reservoir solution was set up and equilibrated against 40 µL of reservoir solution in different plates incubated at 20°C and 4°C using the vapor-diffusion method. Initial crystals were grown in the presence of 200 mM sodium trihydrate acetate pH 8, 20% PEG 3350 at 4°C. After the optimization of crystallization conditions, well diffracting crystals were obtained in a condition containing 200 mM sodium trihydrate acetate pH 8, 16% PEG 3350. All diffraction data were collected at the synchrotron Swiss Light Source, Villigen, Switzerland. Initial phases were obtained by molecular replacement with Coot using DHS (PDB 6XXH) and aIF5A (PDB 3CPF) as search models.

4 RESULTS

4.1 Summary of the first part of the project

Part of my PhD project has focused on the *in-depth* study of DHS, the first enzyme involved in the hypusination reaction, with the purpose to gain structural information which could help to design and develope new potential therapeutic molecules able to block hypusination and then eIF5A activity. In order to reach this goal, we have performed both biochemical assays and bioinformatic analysis to get a complete overview of the protein behaviour. The obtained results have been published in 2020 in Frontiers in Chemistry (D'Agostino et al., 2020) and are summarized below.

Briefly, we sought to analyze the interaction between DHS and GC7, that is the most potent inhibitor of the enzyme. We used as a model the thermophilic protein of the crenarchaeon *Sulfolobus solfataricus* that is hypusinated and conserved in comparison with the eukaryotic version (archaeal one shares with the human homolog 33 and 58% of amino acid identity and similarity, respectively (Bassani et al., 2018, 2019). We believed that the archaeal protein might represent a model system that can offer biochemical and structural information, which can be useful in the design of new inhibitors of both hypusination process and DHS–eIF5A complex formation. Furthermore, we suppose that understanding of the molecular details of the DHS inhibition in extremophile models such as *S. solfataricus* gives further insights for a more accurate drug design of therapeutic molecule, useful to treat different diseases. As mentioned above, we have analysed different aspects of the binding mode of GC7 within the active site in both *H. sapiens* and *S. solfataricus* DHS using a multidisciplinary approach based on advanced computational (molecular

dynamic simulation and metadynamic simulation) and experimental techniques.

Results from metadynamic (MetaD) simulations show that the GC7 interaction is less stable in the thermophilic enzyme compared to the human one which can mean a lower inhibitory ability of the hypusination reaction in *Sulfolobus solfataricus.* To confirm this hypothesis, we have investigated GC7 effect (in different molar concentrations) on *S. solfataricus* by evaluating cellular growth and results have shown absence of inhibition of aIF5A hypusination in contrast to the established effect on eukaryotic cellular growth (Nakanishi and Cleveland, 2016; Schultz et al., 2018b; Martella et al., 2020). We have also analyzed *in-vivo* the level of hypusinated aIF5A after 48 h of treatment with different concentrations of GC7 showing no inhibitory effects, confirming the different behaviour of GC7 on archaeal and eukaryotic DHS enzymes, as previously predicted by MetaD simulations.

Finally, MetaD simulations provided two different unbinding paths of GC7 within the active site of DHS, defined Path A and Path B. The path A, that has never been described before, occurs more frequently (i.e., 70%), and it implies a protein conformational rearrangement to allow GC7 to exit; on the contrary, in path B GC7 exit happens through the preformed tunnel that is already visible in the previous discussed X-ray structures (Liao et al., 1998; Umland et al., 2004; Wątor et al., 2020). The identification of a new unbinding path of GC7, together with the comparative description of the structural, dynamical and biochemical differences between archaeal DHS and human DHS, provides an extensive set of key information for the design of a new class of inhibitors, not

only able to block the hypusination process but also the formation of the DHS–eIF5A complex.

4.2 Insights Into the Binding Mechanism of GC7 to Deoxyhypusine Synthase in Sulfolobus solfataricus: A Thermophilic Model for the Design of New Hypusination Inhibitors

Mattia D'Agostino [1], Stefano Motta [2], Alice Romagnoli [1,3], Patrick Orlando [1], Luca Tiano [1],Anna La Teana [1,3] and Daniele Di Marino [1,3]**

[1] Department of Life and Environmental Sciences, Polytechnic University of Marche, Ancona, Italy, [2] Department of Earth and Environmental Sciences, University of Milano-Bicocca, Milan, Italy, [3] New York-Marche Structural Biology Center (Ny-Masbic), Polytechnic University of Marche, Ancona, Italy

Translation factor 5A (eIF5A) is one of the most conserved proteins involved in protein synthesis. It plays a key role during the elongation of polypeptide chains, and its activity is critically dependent on hypusination, a post-translational modification of a specific lysine residue through two consecutive enzymatic steps carried out by deoxyhypusine synthase (DHS), with spermidine as substrate, and deoxyhypusine hydroxylase (DOHH). It is well-established that eIF5A is overexpressed in several cancer types, and it is involved in various diseases such as HIV-1 infection, malaria, and diabetes; therefore, the development of inhibitors targeting both steps of the hypusination process is considered a promising and challenging therapeutic strategy. One of the most efficient inhibitors of the hypusination process is the spermidine analog N1-guanyl- 1,7-diaminoheptane (GC7). GC7 interacts in a specific binding pocket of the DHS completely blocking its activity; however, its therapeutic use is limited by poor selectivity and restricted bioavailability. Here we have performed a comparative study between human DHS (hDHS) and archaeal DHS from crenarchaeon Sulfolobus solfataricus (aDHS) to understand the structural and dynamical features of the GC7 inhibition. The advanced metadynamics (MetaD) classical molecular dynamics simulations show that the GC7 interaction is less stable in the thermophilic enzyme compared to hDHS that could underlie a lower inhibitory capacity of the hypusination process in Sulfolobus solfataricus. To confirm this hypothesis,

we have tested GC7 activity on S. solfataricus by measuring cellular growth, and results have shown the lack of inhibition of aIF5A hypusination in contrast to the established effect on eukaryotic cellular growth. These results provide, for the first time, detailed molecular insights into the binding mechanism of GC7 to aDHS generating the basis for the design of new and more specific DHS inhibitors.

published: 17 December 2020 doi:
10.3389/fchem.2020.609942

INTRODUCTION

Protein synthesis represents the final step of gene expression and, being one of the most energy-consuming process in cells, not surprisingly, it is highly regulated in all domains of life.

Regulation can be exerted either on the whole translation process or on specific mRNAs, and it can be mediated by different cis-acting elements present on the mRNAs, as well as by trans-acting factors (Sonenberg and Hinnebusch, 2009; Bhat et al., 2015).

Several of the regulatory proteins belong to the group of translation factors (Bhat et al., 2015), and one of the most important ones is the protein called Initiation Factor 5A in Eukarya and Archaea (eIF5A/aIF5A) and EF-P in Bacteria (Dever et al., 2014; Rossi et al., 2014; Benelli et al., 2017).

IF5A belongs to the small group of the universally conserved translation factors (Kyrpides and Woese, 1998). It is an abundant, acidic protein, which plays a fundamental role by promoting recovery of translation on ribosomes, which are stalling during synthesis of proteins containing particular sequences (for example, stretches of polyproline) (Park and Wolff, 2018). In addition to its function in translation, IF5A has been proposedto play other roles (Park et al., 2010; Bassani et al., 2019).

In order to correctly perform its function in translation, IF5A must undergo a unique and characteristic posttranslational modification called hypusination in Eukarya and Archaea, and β-lysinylation in Bacteria (Rajkovic and Ibba, 2017; Park and Wolff, 2018).

For the aims of this work, we will focus only on the eukaryaland the archaeal proteins.

Hypusination consists in the transformation of a conserved lysine residue (Lys 50 in human eIF5A) into a nonstandard amino acid called hypusine using spermidine as a substrate(Park et al., 1981; Park and Wolff, 2018), and this modification pathway, as characterized in Eukarya, is carried out by two enzymes: deoxyhypusine synthase (DHS) and deoxyhypusine hydroxylase (DOHH) (**Figure 1A**). The first step of the reaction ischaracterized by the transfer of the aminobutyl moiety, producedby the cleavage of spermidine, on the conserved lysine with the formation of deoxy-hypusine (**Figure 1B**). The DOHH catalyzes the oxidation of the deoxy-hypusine converting it to hypusine (**Figure 1A**) (Park et al., 1981).

The modification pathway is conserved in all Eukarya, while Archaea show some heterogeneity (Bartig, 1992; Prunetti et al., 2016). In some organisms, aIF5A is hypusinated; in others, only the deoxyhypusinated version is present and very few contain both versions of the protein. A DHS gene hasbeen found in all archaeal genomes sequenced so far, whileno DOHH homolog has been identified. Nevertheless, several archaeal strains contain the hypusine modification, leaving the question of how this posttranslational modification occurs in these organisms unanswered (Park and Wolff, 2018).

Our group has demonstrated that aIF5A from the hyperthermophilic crenarchaeon *Sulfolobus solfataricus* is hypusinated, as its eukaryotic counterpart and that *S. solfataricus* DHS (aDHS), that shares with the human homolog 31 and 52% of amino acid identity and similarity, respectively, interacts with aIF5A catalyzing the formation of deoxyhypusine, suggesting that the first step of hypusination is conserved in this organism (Bassani et al., 2018) (**Figure 1B**). Recently, crystal structuresof two eukaryotic, *H. sapiens* (Umland et al., 2004; Wator et al., 2020) and *T. brucei*, and one archaeal, *P. horikoshii* (Chen et al., 2020), DHS enzymes have been solved. All three enzymes share a similar folding being organized in tetramers composed by four monomers of ∼40 kDa, with two active sites located at the dimer interface (Umland et al., 2004; Chen et al., 2020). In addition, the structure of the human enzymein complex with different ligands like spermidine, spermine, putrescine, NAD+, and GC7 is also available (Umland et al., 2004; Wator et al., 2020). Spermidine binds DHS into a small cavity composed of amino acids with specific physicochemical properties able to establish a characteristic network of interaction with the ligand. Indeed, the two terminal groups of spermidine interact with three acidic residues of DHS (Asp243-, Asp316-, and Glu323) anchoring it into the narrow binding pocket (Lee et al., 2001; Wator et al., 2020).

The eIF5A structure from several organisms has also been solved (Dever et al., 2014), and despite the bunch of structural and biochemical information available, the three-dimensional (3D) organization of the DHS–eIF5A complex is still unknown. The strong geometric complementarity of DHS and eIF5A structures provides some useful clues for potential organization of the complex. In fact, the DHS binding pocket for spermidine isa narrow cavity, whereas the conserved lysine on eIF5A is located at the peak of a loop connecting two β-strands (**Figure 2B**).

Human eIF5A exists in two isoforms, eIF5A1 and eIF5A2, and both have been related to several diseases. In particular, both isoforms of eIF5A are overexpressed in many types of cancer [for review, see Mathews and Hershey (2015)] and in various others diseases such as HIV-1 infection (Bevec et al., 1996), malaria (Kaiser et al., 2007), and diabetes (Maier et al., 2010).

The involvement in pathogenesis together with the high specificity and functional relevance of the hypusination reaction have prompted researchers to consider eIF5A and its modification pathway as an important and promising therapeutic target stimulating the design and development of eIF5A inhibitors able to target the hypusination process (Olsen and Connor, 2017; Turpaev, 2018), including the DHS–eIF5A complex formation (**Figure 1B**).

Different molecules have already been developed as specific inhibitors of both DHS (Jakus et al., 1993; Nakanishi and Cleveland, 2016; Schultz et al., 2018) and DOHH (Hoque et al., 2009; Olsen and Connor, 2017), but those targeting DHS are characterized the best. To date, no inhibitors targeting the DHS–eIF5A complex formation have been discovered.

The most powerful DHS inhibitor, among the various spermidine analogs is N1-guanyl-1,7-diaminoheptane (GC7) (**Figure 1C**), a compound showing a Ki = 10 nM, which is ∼500times lower than the Km of the physiological spermidine (Jakus et al., 1993).

The use of GC7, alone or in combination with other drugs, was demonstrated to inhibit the growth of various mammalian cells (Nakanishi and Cleveland, 2016; Schultz et al., 2018; Martella et al., 2020). However, GC7 and other DHS inhibitors

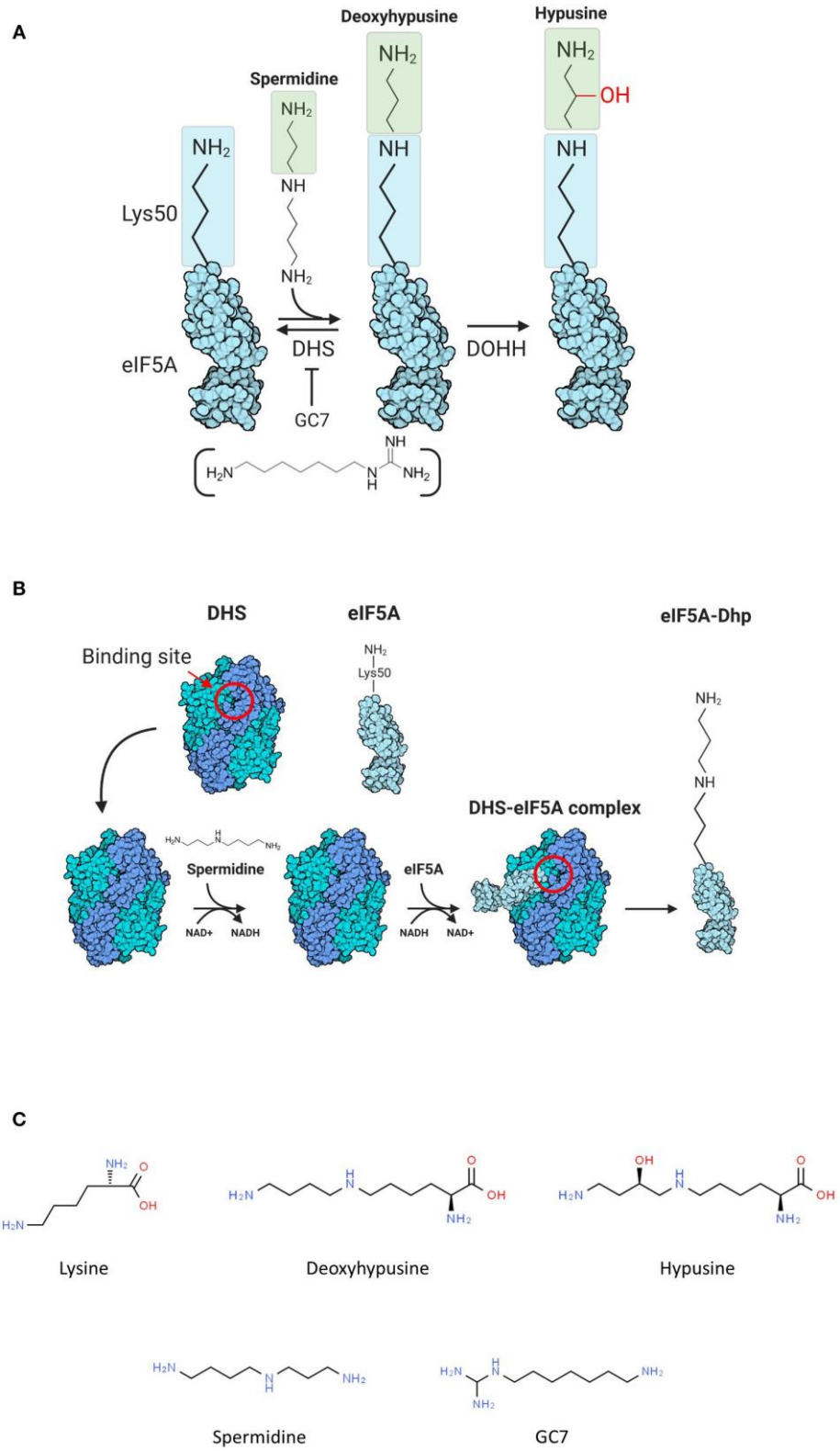

FIGURE 1 | (A) Scheme of hypusination reaction. (B) Scheme of the first part of hypusination reaction. The binding site of deoxyhypusine synthase (DHS) is reported (red circle). (C) Chemical formulations of molecules involved in the hypusination pathway.

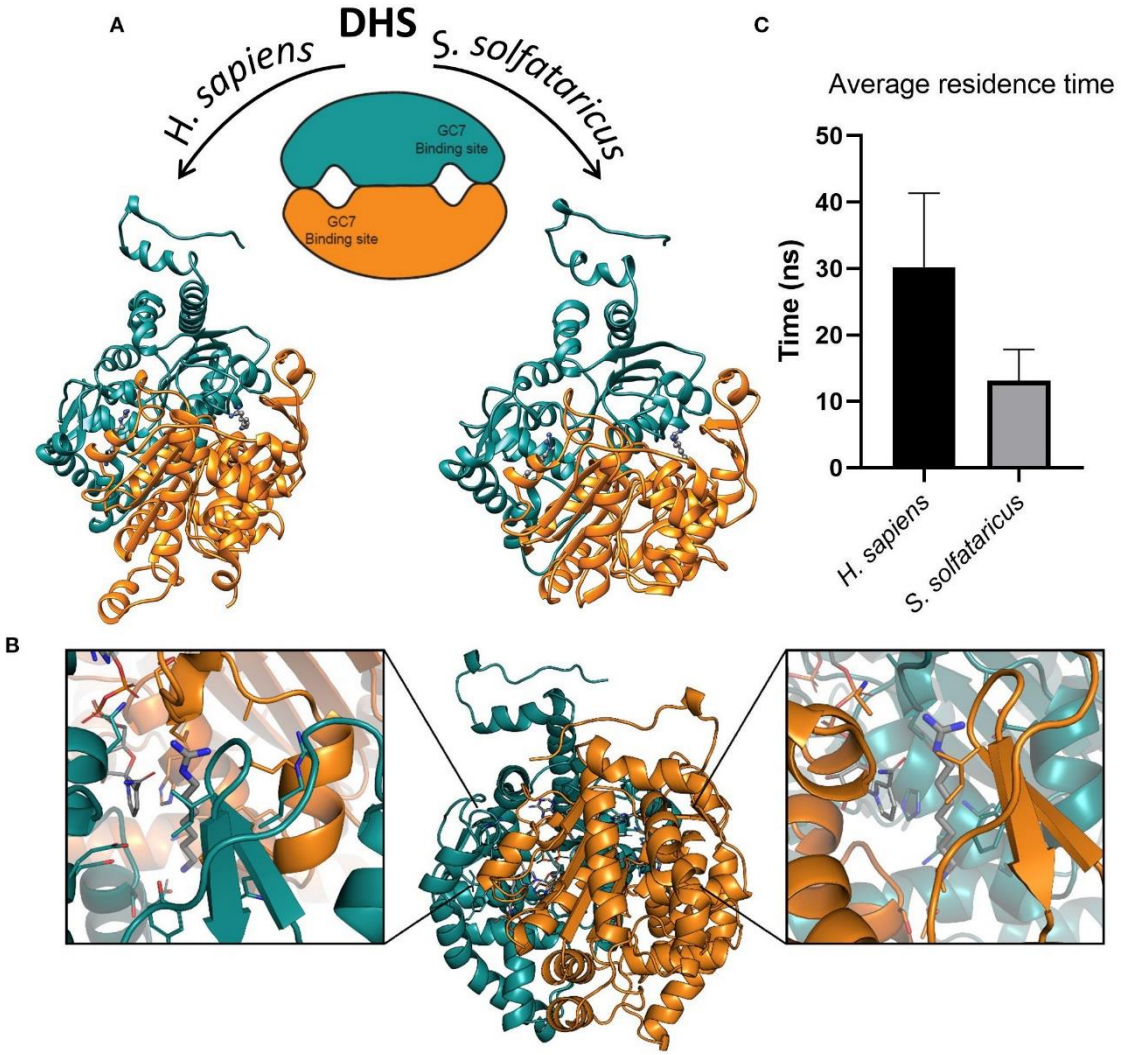

FIGURE 2 | (A) Structures of deoxyhypusine synthase in *Homo sapiens* and *Sulfolobus solfataricus.* Schematic and three-dimensional representations of symmetric dimeric structure of *H. sapiens* (PDBID:1RQD) and *S. solfataricus* DHS obtained through homology modeling. The two GC7 binding sites are shown in the interfaces between the two monomers. The two molecules of GC7 are present inside the binding pockets in both models. (B) Symmetric binding sites in the *H. sapiens* DHS dimer. Binding of GC7 occurs at the interface between the two subunits (orange and eastern-blue in figure). GC7 is shown in gray thick sticks, sidechain of residues within 5 Å from GC7 in sticks colored according to the subunit, and NAD molecule in gray sticks. (C) Average residence time measured for the unbinding of GC7 from human and archaeal DHS in metadynamic (MetaD) simulations. Average residence times are significantly different ($p < 0.05$).

are not sufficiently selective giving rise to several side effects. Furthermore, the bioavailability of these compounds is restrictedby physiological polyamine oxidases present in the blood. For these reasons they are not used in clinical trials (Turpaev, 2018) making possible further studies concerning the inhibition of the DHS function.

In light of the strong similarity between eukaryal and archaeal proteins, we thought that the archaeal could represent a model system that is able to provide structural and biochemical information, which can turn useful in the design of new inhibitors of both hypusination process and DHS–eIF5Acomplex formation. Moreover, we believe that understanding of the molecular details of the DHS inhibition in extremophiles such as *S. solfataricus* provides further insights for a more precise drug design of molecules that can be used to treat different pathologies.

In order to address this issue, we investigated the interaction between DHS and its inhibitor GC7 by comparing the human and *Sulfolobus* system. We started from the observation that, despite the enzyme conservation, GC7 shows a different behavior on different archaeal organisms (Jansson et al., 2000).

Here we have used a combination of advanced computational approaches and experimental techniques to analyze the different features of the binding mode of GC7 into the active site in both *H. sapiens* and *S. solfataricus* DHS (i.e., hDHS and aDHS).

Results from metadynamic (MetaD) simulations highlighted a different stability of the two GC7–DHS complexes, which is dueto specific interaction networks established within the binding sites. Interaction of GC7 with aDHS is significantly less stable compared to hDHS, and this result was validated by *in vivo* experiments on *S. solfataricus* cells whose growth was unaffectedby the presence of GC7.

This comparative and multidisciplinary study provided an in-depth characterization of the molecular mechanism ofinteraction of GC7 with both human and archaeal DHS paving the way for the design of new, specific, and more sensitiveDHS inhibitors.

MATERIALS AND METHODS

Sulfolobus solfataricus Cell Growth

S. solfataricus P2 cultures were grown in liquid Brock's medium (Brock's salts supplemented with 0.2% N-Z-amine, 0.2% sucrose, pH 3.0) in a shaking water bath at a speed of 150 rpm atthe temperature of 348 K (75°C). Growth was monitored by measuring the optical density at 600 nm (OD600). For a typical experiment, an *S. solfataricus* P2 culture with a starting OD600 of 0.05 was split into six different flasks of 10 ml each, and GC7 (Sigma-Aldrich) was added in the following concentrations: 0 (control), 10, 50, 100, 250, and 500 μM respectively. OD600 measurements were taken at 0 hour (h), 15, 24, 48, 72, and 96 h.At a time point of 48 h, a 1-ml aliquot from each sample was harvested and centrifuged. The resulting cell pellets were washedthree times with fresh Brock's medium and then resuspended with a resuspension buffer [20 mM Tris/HCl pH 7.8, 10 mM $Mg(CH_3COO)_2$, 40 mM NH_4Cl, 6 mM β-mercaptoethanol].Cells were lysed by six freeze and thaw cycles, and total protein concentration of each sample was determined using the Bradford reagent (Sigma-Aldrich). The levels of hypusinated aIF5A in each lysate sample were analyzed by Western blot.

Western Blot

Western blot analysis was performed as previously described (Bassani et al., 2018) with some modifications. Briefly, 15 μgof total proteins for each sample was separated on SDS-15% polyacrylamide gel using standard protocols and then transferred onto a 0.2-μm nitrocellulose membrane (GE Healthcare) using wet transfer blotting apparatus. Protein transfer was performedat 100 V for 30 min in a transfer buffer (25 mM Tris, 192 mM glycine, 20% methanol). Nonspecific binding was blocked using5% nonfat milk. The membranes were probed overnight at 4°C, either with anti-aIF5A (used at a 1:5,000 dilution in TBS-Tween containing 5% of nonfat milk) or with anti-hypusine antibody (Millipore). The detection of primary antibodies was obtained by horseradish peroxidase (HRP)-conjugated anti-rabbit IgG (Cell Signaling Technology), using the enhanced chemiluminescent reagent (EuroClone). The images were visualized with a BioRad ChemiDoc™ MP Imaging System. The quantification of the signals was obtained by the ImageLab™ software (Biorad).

Analysis of GC7 Uptake

The evaluation of the presence of GC7 inside the cells was obtained through the dansyl-chloride method as previously described (Ahmed et al., 2017), with some modifications. Briefly, 1 ml of cell cultures grown in the absence and in thepresence of 500 μM of GC7 were collected by centrifugation after 72 h; the resulting pellets were washed three times with fresh Brock's medium to avoid false positives due to free GC7 in the medium. The pellets (~40 mg) were extracted in 5% cold perchloric acid. Sample extracts were centrifuged at 27,000 g for 10 min. Dansyl derivatization was obtained, 200 μl of extracted sample was mixed with 200 μl of saturated sodium carbonate (100 mg/ml) and 400 μl of dansyl chloridein acetone (10 mg/ml). After vortexing, the mixture was incubated overnight at room temperature in the dark. Excess dansyl chloride was removed by adding 100 μl of L-proline(100 mg/ml) followed by incubation for 30 min at room temperature in the dark. The dansylated polyamines were further extracted with 350 μl of toluene. The organic phase containing polyamines and GC7 was evaporated using a speed- vac, and the residue was dissolved in 500 μl of methanol. The dansylated polyamines were separated by HPLC (YL Instrument 9300, Amaze instrument, Uttar Pradesh, India) equipped with a fluorescence detector (Nanospace-SI2, Shiseido) and a column Kinetex C18 100 A, 250 × 4.6 mm, 5 mm (Phenomenex, Torrance, CA, USA). For identification of GC7 and endogenous spermidine, standards were used (10 μl of 100 μM GC7 and 10 μl of 20 μM spermidine).

Molecular Dynamics Simulations

Crystal structures for *H. sapiens* DHS in complex with GC7 inhibitor were obtained from the Protein Data Bank (PDB) in its homodimeric state (Umland et al., 2004) (1RQD). A homology model of the *S. solfataricus* DHS was built using an HHpred toolkit (https://toolkit.tuebingen. mpg.de/tools/hhpred) (Söding et al., 2005) selecting as template the X-ray structure of the *H. sapiens* DHS (PDBID:1RQD). The overall quality of the model was assessed with PROCHECK (Laskowski et al., 1993), which providesinformation about the stereo-chemical quality, and ProSA validation method (Wiederstein and Sippl, 2007), which evaluates model accuracy and statistical significance with a knowledge-based potential. The main results are reported in**Supplementary Figure 1**.

Both structures were then pre-processed for simulation with the Schrodinger's Protein Preparation Wizard tool (MadhaviSastry et al., 2013): hydrogen atoms were added, all water molecules were removed, C and N terminal capping was added, disulfide bonds were assigned, and residue protonation states were determined by PROPKA (Bas et al., 2008) at pH = 7.0. Each system was then solvated in a cubic box with TIP3P water molecules and neutralized with Na^+/Cl^- ions using the GROMACS (Abraham et al., 2015) preparation tools. The minimal distance between the protein and the box boundaries was set to 14 Å. Simulations were run using GROMACS 2018 with Amber ff14SB force-field (Maier et al., 2015). The parameter for NAD molecule was retrieved from amber library (Walker

et al., 2002), while GC7 inhibitor was parameterized using GAFF (Wang et al., 2006). Charges were calculated with the restricted electrostatic potential (RESP) method (Bayly et al., 1993) at HF/6-31G* after *ab initio* optimization. A multistage equilibration protocol, similar to the one applied in Motta et al. (2018) was applied to all simulations to provide a reliable starting point for the production. The system was subjected to a 2,000- step of steepest descent energy minimization with positional restraints (2,000 kJ mol^{-1} nM^{-2}) on backbone and ligand atoms. Subsequently, MD simulation in an NVT ensemble was used to heat the system from 0 to 100 K in 1 ns with restraints lowered to 500 kJ mol^{-1} nM^{-2}. Temperature was controlled by the Berendsen thermostat (Berendsen et al., 1984) with a coupling constant of 0.2 ps. The system was then heated up to 300 K (27°C)[348 K (75°C) in *S. solfataricus*] in 2 ns during an NPT simulation with restraint lowered to 200 kJ mol^{-1} nM^{-2} using the V-rescale thermostat (Bussi et al., 2007) with a coupling constant of 0.1 ps.

Pressure was set to 1 bar with the Parrinello–Rahman barostat (Parrinello and Rahman, 1981) with a coupling constant of 2 ps. A time step of 1.0 fs was used during these steps, together with the LINCS algorithm (Hess et al., 1997) to constrain allthe bonds.

Finally, the system was equilibrated in two stages of NPT simulations of 5 ns each, with backbone restraints lowered to 100 and 50 kJ mol^{-1} nM^{-2} respectively. The timestep was increased to 2.0 fs in these stages and during all the production runs.

The particle mesh Ewald (Darden et al., 1993) method was usedto treat the long-range electrostatic interactions with the cutoff distances set at 12 Å. Productions runs were conducted in NPT for 600 ns for both the *H. sapiens* and *S. solfataricus* systems.

Metadynamics Simulations

Metadynamics is an enhanced sampling method based on the introduction of a history-dependent bias on a small numberof suitably chosen collective variables (Laio and Parrinello, 2002; Laio and Gervasio, 2008; Bussi and Branduardi, 2015).A large number of studies was carried out to elucidate the binding/unbinding process of ligand/protein systems (Limongelliet al., 2010; Casasnovas et al., 2017; Provasi, 2019). Morerecently, infrequent metadynamics was introduced to study the unbinding kinetic (Tiwary and Parrinello, 2015; Tiwary et al., 2015; Wang et al., 2018). In a similar manner, here, we used metadynamics to speed-up the unbinding process, usingthe number of contacts between the binding site residues ofDHS (residues at 4 Å from the native pose) and GC7 as unique CV, and performing 30 replicas to obtain a statisticson the "average residence time" of the ligand in metadynamics simulation. Hills with a height of 0.2 kJ mol^{-1} and a widthof 2.0 were deposited every 2.0 ps at 300 K (27°C) for both systems. The number of contacts in the native pose was around 650 for both the *H. Sapiens* and *S. solfataricus* systems, and we considered the ligand as exited from the binding site when the number of contacts reaches the number of 200. This number is small enough to guarantee the overcoming of the energetic barrier splitting the bound and the unbound states.

The residence time in MetaD calculation was computed as the average time required to observe the unbinding (number of contacts < 200) in the different replicas. A change in this cutoff value does not appear to affect the result of the analysis (data not shown).

RESULTS

Comparative Analysis of the hDHS andaDHS Structure

GC7 is the most potent inhibitor of DHS that represents the first enzyme involved in the two steps of the hypusination reaction. Although this molecule is effective in blocking the growth of various eukaryotic cell lines (Kaiser, 2012; Caraglia et al., 2013; Mathews and Hershey, 2015), on the other hand, it seems to have a slightly different effect in Archaea (Jansson et al., 2000),even if the enzyme is extremely conserved (Bassani et al., 2018). The structural and dynamical reasons of this discrepancy inthe GC7 activity are still unknown. In order to investigate at the molecular level the interaction between GC7 and the two conserved enzyme (i.e., hDHS and aDHS), we have first built the three-dimensional (3D) structure of the DHS from *S. solfataricus* (**Figure 2A**, right side) using as template the 3D structure from *H. sapiens* DHS (Umland et al., 2004) (**Figure 2A**, left side).

As reported in different DHS X-ray structures (Umland et al.,2004; Tanaka et al., 2020; Wator et al., 2020), the binding of GC7 occurs at the interface between the two subunits of the tetramer, in a symmetric mode that leads to the formation oftwo binding sites for each dimer (**Figure 2B**). Interestingly, GC7interacts with both monomers and with the NAD molecule that is located in a conserved pocket close to the GC7 binding site. Based on the hDHS X-ray structures bound to GC7 (Umland et al., 2004), we developed a structural model for aDHS. The GC7 binding orientation in aDHS was obtained starting from the position in hDHS and minimizing the structure. A careful equilibration protocol was introduced before the MD simulation to avoid artifacts due to a bad ligand starting position. As a result of this procedure, the ligand orientation remained unaltered, and only a few residue sidechains changed their conformation.

An in-depth comparative structural analysis of the GC7 binding site in the X-ray of hDHS and in the aDHS model highlights few differences in the residues composing the narrow pocket (**Supplementary Figure 2**). At the level of the guanidino group of GC7 into an active site, only two residues are different between hDHS and aDHS (**Supplementary Figures 2A,B**). A critical mutation is the hDHS Asp316 residue substitutedby Leu272 in aDHS. The strongest differences in the bindingsite are located in correspondence of the GC7 amine group(**Supplementary Figures 2C,D**). Here the most critical substitution is Asp243 present in hDHS (forming a salt bridge with GC7) that is substituted by Thr200 in aDHS that does not allow the formation of a specific electrostaticinteraction. Overall, only 10 over 25 residues change between

hDHS and aDHS; most of them do not significantly alter the global shape and the general chemical properties ofthe pocket.

Evaluation of GC7 Binding Stability in hDHS and aDHS Through MetadynamicSimulations

In order to characterize the binding stability of GC7 in hDHS and aDHS, we designed a MetaD protocol to evaluate the unbinding mechanism of GC7 from the conserved DHS binding pocket. We chose the number of contacts between the residues belongingto the binding site of both hDHS and aDHS and GC7 as CVto describe the energetic and structural–dynamical features of the GC7 binding stability. We have performed 30 replicas of MetaD simulation to collect a significant number of unbinding events allowing us to extract the molecular descriptors of GC7-hDHS/aDHS interaction. The simulations were stopped when the number of contacts between ligand and binding site residues were <200. This cutoff value corresponds to a confident prediction of the unbound state of the ligand as shown in two examples in **Supplementary Figure 3**. In this conformation, the GC7 centerof mass (COM) drifted from the native bound state of about 11 Å.An important parameter to evaluate the stability of a protein- ligand complex can be identified in the residence time of theligand into the protein binding site. The trajectories of the GC7 unbinding obtained through MetaD simulations allowedus to observe the entire exit path of the ligand and alsoto compare the different residence time of the ligand intothe hDHS and aDHS binding sites. Higher residence times isexpected for the more stable complex based on the number and type of interactions established by the ligand (i.e., GC7) with the residues composing the protein binding pocket. Resultsof these calculations are shown in **Figure 2C**. Surprisingly,GC7 showed a significantly higher residence time in the *H.sapiens* DHS compared to the *S. solfataricus* one. The analysisof the unbinding mechanisms revealed two different unbindingpathways for hDHS (**Supplementary Figure 3**). Path A wassampled in most of the replicas (70%). Interestingly, the replicasfollowing path A present a similar behavior, evolving through thesame intermediate state with the amine group of GC7 involved ina salt bridge with Glu136 and Glu137. On the other side, in thereplicas evolving through path B, GC7 leaves the pocket from theother side, and the amine group starts to interact with Glu180 (**Supplementary Figure 4A**). Notably, the guanidino group ofGC7 forms a salt bridge with the same two residues involvedin path A (i.e., Glu136 and Glu137). Similar pathways were also found during the aDHS MetaD simulations, with path A foundin most of the replicas (70%). Due to the substitution in aDHS ofGlu136 and Glu137 with Asp95 and His96, when GC7 leaves thebinding pocket following the path A, no stable conformation wasidentified, and the exit occurs in a single passage in most of thereplicas. On the contrary, replicas following path B always evolve forming an interaction with Glu141 (Glu180 in hDHS), but theinteraction lasts for less time, and the GC7 is rapidly released in
the solvent (**Supplementary Figure 4B**).

Although the two DHS enzymes share a significant sequence identity and similarity (i.e., 60% of identity in the binding site) as reported in the previous paragraph, the results described sofar prompted us to investigate more thoroughly the inhibition mechanism of GC7 in hDHS and aDHS.

GC7 Has No Effect on *Sulfolobussolfataricus* Cell Growth

The MetaD results highlighted a different stability of the interaction between GC7 and DHS in *H. sapiens* and *S. solfataricus.* To experimentally confirm these theoretical results, we have tested the effect of GC7 on *S. solfataricus* cellular growth.
S. solfataricus cells were grown in the absence and in the presenceof different concentrations of GC7 (0, 10, 50, 100, 250, and500 μM). Results presented in **Figure 3A** show that GC7 hasno effect on the growth of *S. solfataricus* even at the highest concentration (500 μM) of the inhibitor. These results are in contrast with those obtained on eukaryotic cells (Lee et al., 2002; Schultz et al., 2018; Martella et al., 2020) and confirm the different effect of GC7 on archaeal and eukaryotic DHS enzymes, as predicted by MetaD simulations.

GC7 Has No Effect on aIF5A Hypusinationin *Sulfolobus solfataricus*

To understand if GC7 is able to inhibit the first step of the hypusination reaction in *S. solfataricus*, we have analyzed the level of hypusinated aIF5A after 48 h of treatment with different concentrations of GC7 (0, 10, 50, 100, 250, and 500μM) by Western blot. Two primary antibodies were used: one able to recognize both modified and unmodified aIF5A (Bassani et al., 2018), and a second one specifically directed against the hypusine residue.
As shown in **Figure 3B**, the lysates from all samples contain the hypusinated version of aIF5A as demonstrated by the presence of a signal of comparable intensity in all lanes from both anti-hypusine and anti-aIF5A, confirming that GC7 is not able to inhibit the hypusination pathway in *S. solfataricus*. The hypusination levels were represented using the ratio between thehypusination signal over that of total aIF5A (**Figure 3C**). These results show that GC7 has no effect on the hypusination level, confirming data obtained by the computational approach.

Presence of GC7 Inside the Archaeal Cells

The external composition of the Archaea is characterized,in addition to the cytoplasmic membrane, by the presence of a cell wall (Albers and Meyer, 2011), which representsa structural and protective barrier that might limit uptakeof external molecule like GC7, making it not available for metabolic pathways. In order to prove that GC7 can penetrate
through *S. solfataricus* cell wall and therefore be present inthe cytoplasm, ~40 mg of wet *S. solfataricus* pellets, treated and non-treated with 500 mM GC7, were subjected to HPLC
polyamines analysis using the dansylation protocol (see materials and methods). Chromatograms showed the profile of native polyamines, visible following fluorescent derivatization, relativeto Proline, Spermidine, and Spermine. Analysis of GC7 treated cells showed two additional peaks identical in retention time

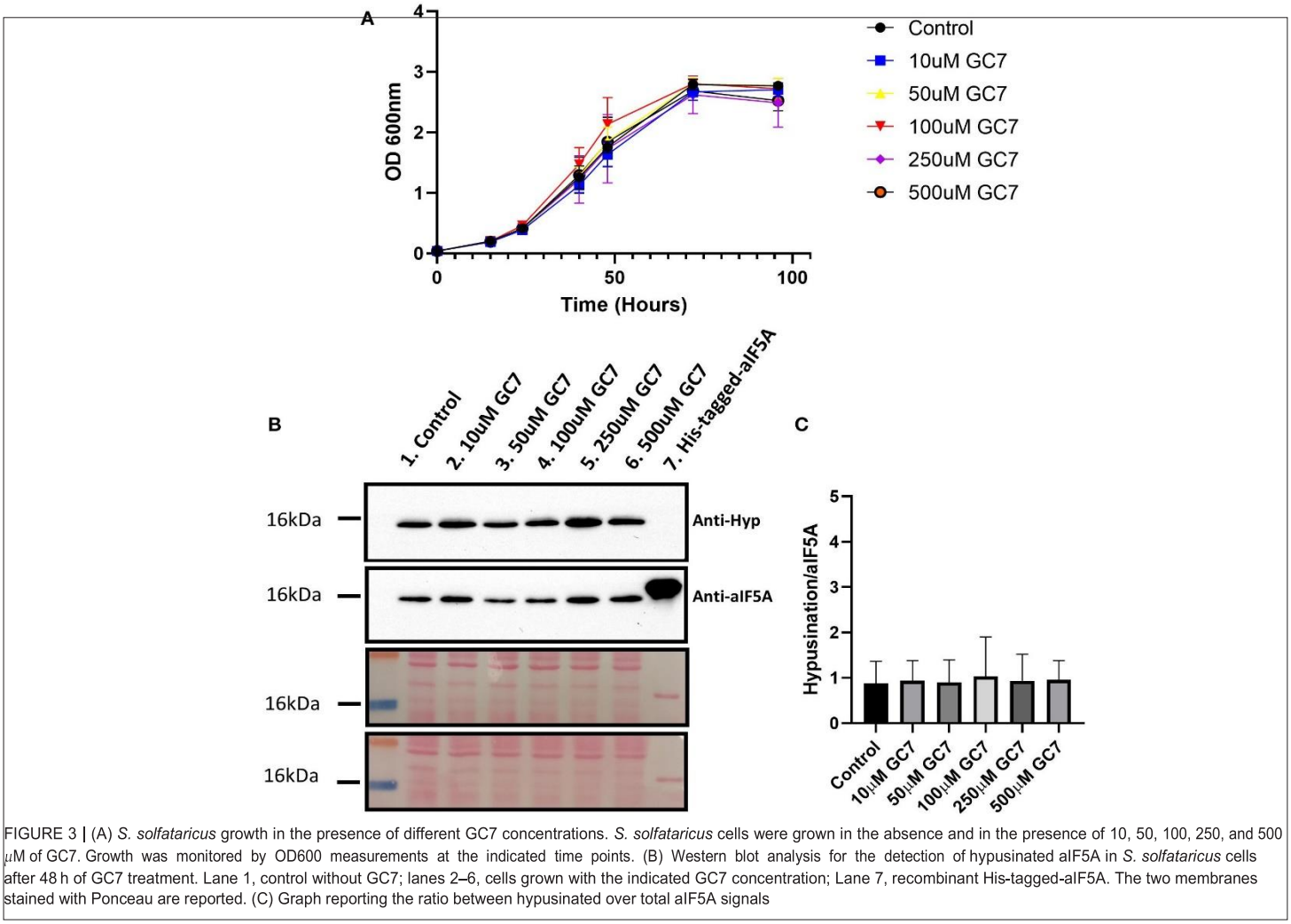

FIGURE 3 | (A) *S. solfataricus* growth in the presence of different GC7 concentrations. *S. solfataricus* cells were grown in the absence and in the presence of 10, 50, 100, 250, and 500 μM of GC7. Growth was monitored by OD600 measurements at the indicated time points. (B) Western blot analysis for the detection of hypusinated aIF5A in *S. solfataricus* cells after 48 h of GC7 treatment. Lane 1, control without GC7; lanes 2–6, cells grown with the indicated GC7 concentration; Lane 7, recombinant His-tagged-aIF5A. The two membranes stained with Ponceau are reported. (C) Graph reporting the ratio between hypusinated over total aIF5A signals

to those obtained following standard injection, suggesting that, despite the physical barrier represented by the cell wall, GC7 is efficiently incorporated into the cells (**Supplementary Figure 5**) thus confirming its inability to inhibit growth and hypusination in *S. solfataricus*.

Molecular Dynamic Simulations Highlightsthe Key Differences in the Binding Site Between hDHS and aDHS

MetaD and experimental results clearly show that the GC7 is not able to inhibit the hypusination process in *S. solfataricus*. The absence of inhibitory activity of GC7 is most likely dueto the different chemico-physical characteristics in the binding pockets between hDHS and aDHS. To further investigate the role of different residues in the two species, we performed unbiased MD simulations of both systems in the bound states (i.e., hDHS + GC7 and aDHS + GC7). The dimeric forms of DHS were simulated containing two binding pockets each bound to a GC7 molecule. We will refer to each binding pocket as binding site 1 and binding site 2. hDHS was simulated at 300 K (27°C), while aDHS was simulated at 348 K (75°C) to better reproduce the biological condition in which the two enzymes are active. The simulations show that GC7 is strongly bound to the human enzyme maintaining the original binding mode for the entire simulation time (**Figure 4A**, left side). On the contrary,in *S. solfataricus*, the GC7 does not maintain the contact with the residues in the active site during the molecular dynamic simulation, as shown in **Figure 4A** (right side) by the evident driftof the molecule within the binding pocket, immediately in the early stage of the simulation.

Such result is confirmed by the 3D scatterplots of GC7 COM coordinates that show the evident drift of the molecule during the *S. solfataricus* simulation (**Figure 4B**). Results are consistent for both GC7 molecules present in both binding sites of DHS.

Finally, to get insights on the reduced stability of GC7 within *S. solfataricus*, we compared the fluctuation of residues forminga contact with GC7 (measured as the RMSF of Cα atom of the

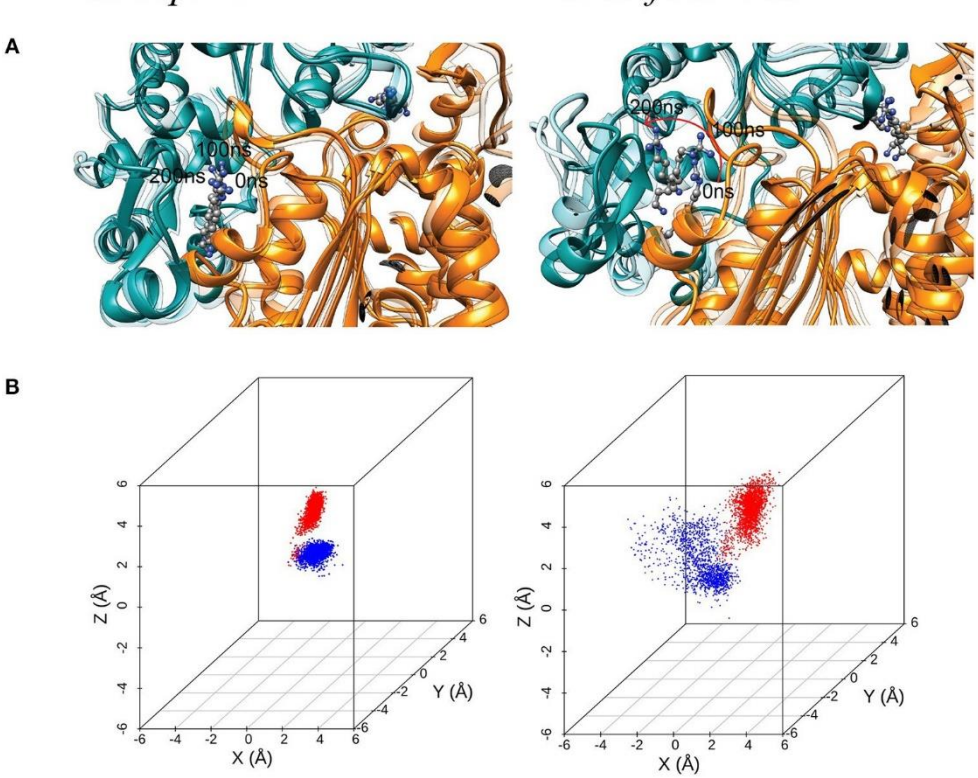

FIGURE 4 | (A) Molecular dynamic (MD) simulation of GC7 into the DHS binding site. The MD simulation of *H. sapiens* DHS, showing the strong binding of GC7 inside the binding pocket. GC7 in *S. solfataricus* DHS presents a different interaction behavior, as shown by the drift of the molecule due to its weak interactions with the enzyme residues. The red arrow follows the movement of the molecule during the first portion of the simulation. (B) 3D scatterplots of GC7 center of mass coordinates shift. *H. sapiens* and *S. solfataricus* simulations are compared. The two molecules of GC7 present in each system were analyzed and represented in red (first subunit) and blue (second subunit) in the plots.

residue). This analysis highlighted a higher fluctuation of the *S. solfataricus* binding site due to the numerous changes in the position of the ligand.

A consistent perturbation appears in the region of residues Gly196, Ser197, and Gly270, Ser271 of *S. solfataricus*, lying respectively at the two ends of GC7. This is in line with the movement of the ligand that rotate within the binding site, losingcontacts at the two ends (**Figure 4A**).

To evaluate the stability of the protein–ligand interaction, we monitored the presence of GC7 contacts with protein residues (**Figure 5B**). GC7 in hDHS maintains almost all its native contacts, while in *S. solfataricus*, GC7 loses most of them during the molecular dynamic simulation, and this is a strong indication that the DHS-GC7 interaction in *S. solfataricus* is weakand unstable.

In particular, we observed that GC7 in *S. solfataricus* seems more destabilized in the region of its charged terminal amine group. In *H. sapiens*, this group is involved in a salt bridgewith Asp243 (**Figure 5A**). This interaction is highly stable in the binding site 2 and contributes to the lower ligand RMSD value registered for this ligand (**Supplementary Figure 6**). In binding site 1, on the other side, this interaction becomes less strong after about 310 ns, due to a shift in the terminal amine group of GC7 that start interacting with Glu136 (**Figure 6B**). Interestingly, the residues Asp243 and Glu136 are mutated respectively in Thr200 and Asp95 in *S. solfataricus* (**Figure 6C**). Therefore, in this simulation, the charged amine group of GC7 immediately moves toward Asp95 in a similar manner to the one observed forthe first binding site of *H. sapiens* (**Figure 6D**). Overall, due to theshorter sidechain of Asp95 compared to the Glu136 of *H. sapiens*, the observed shift of the ligand is more drastic and destabilize thewhole ligand binding mode. Moreover, Trp248 in *S. solfataricus*presents a very bulky sidechain that creates a steric hindrance notallowing a favorable positioning of the ligand (**Figure 6C**). This residue position is indeed occupied by Asn292 in *H. sapiens* thatforms a dense network of h-bonds with GC7 and Asp243, furtherstabilizing the complex (**Figure 6A**).

DISCUSSION

Driven by the idea that knowing the molecular determinants of the GC7 binding in homologs proteins can open new frontiers for the design of inhibitors specific for either or both the hypusination process and the DHS–eIF5A complex formation,

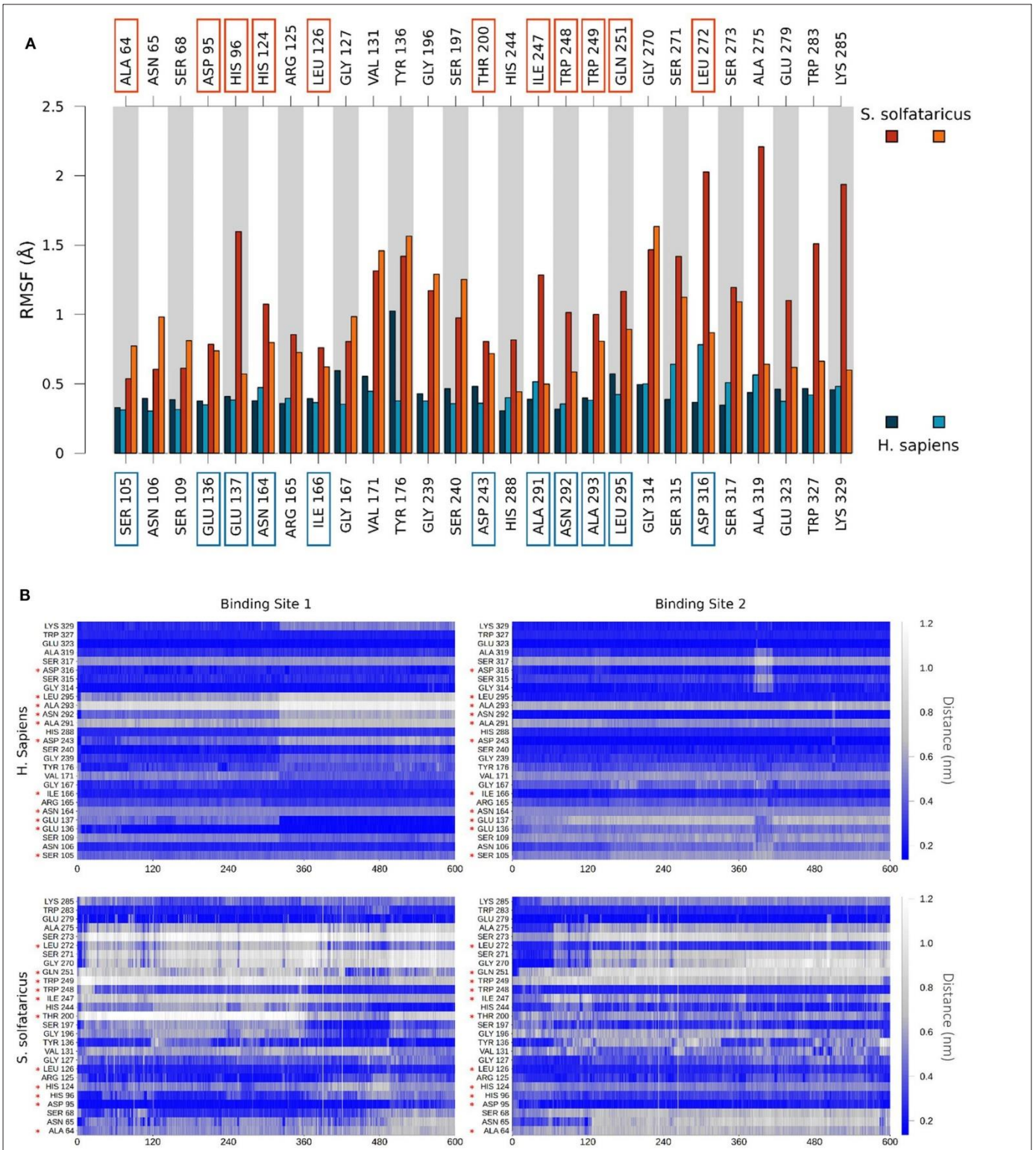

FIGURE 5 | (A) Comparison of per-residue root mean square fluctuation of binding site residues in *H. sapiens* and *S. solfataricus*. Values are drawn as barplots in different colors for the two binding sites in *H. sapiens* (shades of blue, labeled at bottom) and *S. solfataricus* (shades of red, labeled on top). Residues not conserved in the two species are highlighted with squares. (B) Protein–ligand contacts during the unbiased MD simulation. The minimum distance between atoms of the ligand and atoms of each residue of the binding site was monitored for *H. sapiens* (top) and *S. solfataricus* (bottom). The values are drawn in a colorscale with blue indicating lower distances and white higher distances. Residues not conserved in the two species are highlighted with a red star.

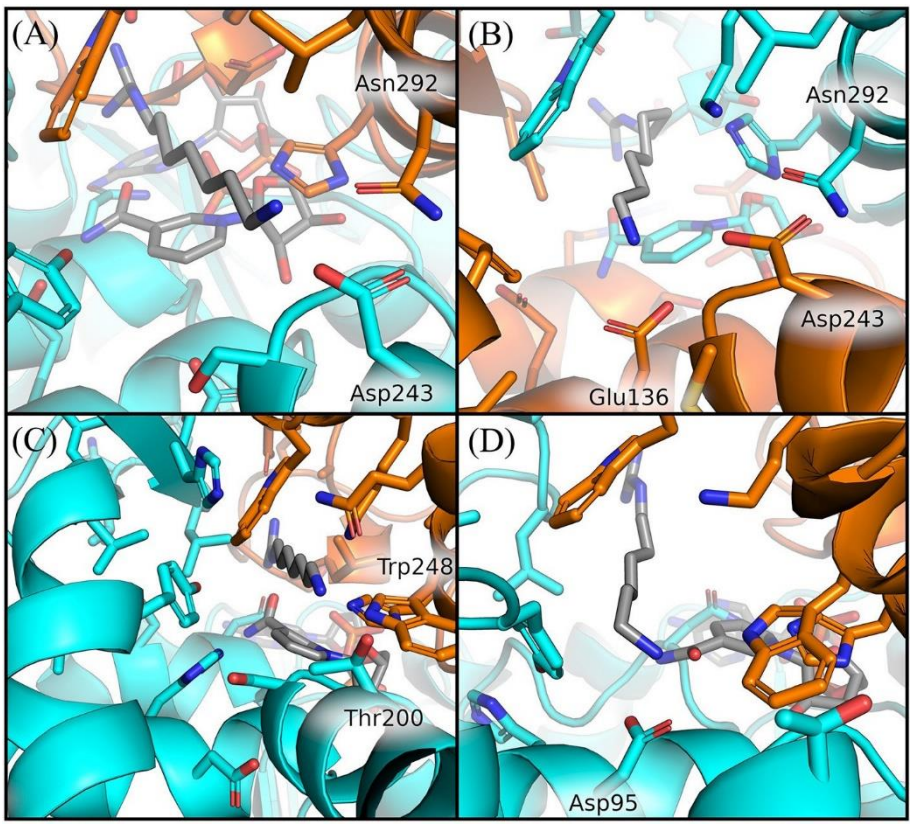

FIGURE 6 | Comparison of GC7 interactions with residues of *H. sapiens* and *S. solfataricus*. Residues of *H. sapiens* within 5 Å from ligand are shown in sticks for binding site 2 at 200 ns (A) and for binding site 1 at 350 ns (B). Residues of *S. solfataricus* within 5 Å from ligand are shown in sticks for binding site 1 at the beginning of the simulation (C) after 200 ns (D). Protein sticks and cartoon are colored in cyan for the first chain and orange for the second chain.

we applied a multidisciplinary and comparative approach to analyze the interaction between both human and thermophilic DHS enzymes and their inhibitor GC7. To reach our aim, we used advanced theoretical approaches, such as classical molecular dynamics or enhanced sampling [sampling (i.e., MetaD and others), successfully and widely used in the study of protein–protein interaction and mechanisms of inhibition exerted bysmall molecules or peptides (Di Marino et al., 2015a, Di Marinoet al., 2015b; D'Annessa et al., 2019)].

The first hypusination step involving DHS is strongly conserved among *H. sapiens* and *S. solfataricus* as well as the aminoacidic sequence of the two enzymes (Bassani et al., 2018). First, to structurally compare the two proteins, we have obtainedthe 3D structure of *S. solfataricus* DHS through homology modeling, using the human DHS structure as template (Umland et al., 2004). Similar to the human enzyme, the archaeal protein has the active site contained within a deep narrow tunnel present at a dimer interface (**Figure 2B**). Interestingly, despitethe high functional conservation between the two enzymes, the aDHS shows some different residues into the binding pocket. Two of them would seem to be relevant for the correct interaction between protein and ligand: (i) Asp316 in hDHS thatis substituted in Leu272 in aDHS destabilizing the interaction of the GC7 guanidinium moiety; (ii) Asp243 that is presents in hDHS and it is substituted by Thr200 in aDHS destabilizing the interaction of the amine portion of the ligand. Lack of Asp243 in aDHS could be relevant for the proper interaction with GC7 since Thr200 is not able to form a salt bridge with the inhibitor.

MetaD simulations allowed us to evaluate the binding stabilityof the GC7 in the two different models. The data highlighted a significantly higher residence time in the hDHS compared to the *S. solfataricus* one. This result strongly underlines a lower stability of the ligand inside the thermophilic DHS binding pocket that could be explained by a different interaction network.MetaD simulations provided two different unbinding paths ofthe ligand. The first path (path A) occurs more frequently (i.e., 70%), and it implies a protein conformational rearrangementto allow the ligand exit (i.e., the opening of loops 310–320 and 165–170) (**Supplementary Figure 4**). On the other hand, the second path (path B), which was observed with a frequency of 30%, is consistent with the one previously discussed (Umlandet al., 2004). In this pathway, the ligand exit occurs through the preformed tunnel that is already visible in the X-ray structures (Umland et al., 2004; Wator et al., 2020). Our MetaD calculationsindicate the preference of path A, despite the conformational rearrangement, but it cannot be excluded that in unbiased

simulations, binding of a ligand may occur preferentially through path B. The discovery of an alternative unbinding path may opena new possibility in the rational drug design of DHS inhibitors. The experimental approach shows that GC7 appears to be unableto inhibit *S. solfataricus* cell growth (**Figure 3A**) and aIF5A hypusination (**Figure 3B**) in contrast to what was previously described for the human enzyme (Nakanishi and Cleveland,2016; Schultz et al., 2018; Martella et al., 2020). Considering also the instability of GC7 in the aDHS model during the MD simulations, the difference in GC7 effectiveness between humanand archaeal models could depend on the different affinity for the two systems that is directly link to the diverse aminoacidic composition of the binding site. These data on an archaeal modelconfirm those on cellular growth (Jansson et al., 2000).

The MD simulations of the bound state of *S. solfataricus* show a higher mobility of the ligands in both binding sites, further evidence of a formation of an unstable complex in this cell (**Figure 4**). The origin of the lower stability of GC7 in *S. solfataricus* can be attributed mainly to three residues different in the two species: Glu 136, Asp243, and Asn292 (Asp95, Thr200, and Trp248 in *S. solfataricus*) (**Figure 6**). Interestingly, all these residues are located near the terminal amine group of GC7. Asp243 plays a key role in stabilizing the GC7 inside the active site of the hDHS but not in the binding with spermidine (Wator et al., 2020). Remarkably, the first step of the hypusination reaction in *S. solfataricus* is conserved, as well as the use of spermidine as substrate of the aDHS (Bassani et al., 2018). In *S. solfataricus*, Asp243 is substituted by Thr200. This difference could explain why GC7 is ineffective for aDHS, while spermidineis correctly used as substrate by the enzyme for the first step of the hypusination reaction (Bassani et al., 2018).

Therefore, ineffectiveness of GC7 on the archaeal model maybe due not only to the different growth conditions but also to the aminoacidic composition of the binding site compared to the *H. sapiens* enzyme.

The identification of the unbinding path of GC7, together with the comparative description of the structural and dynamicaldifferences between aDHS and hDHS, provides a broad setof crucial information for the design of a new class of inhibitors, not only able to block the hypusination process but also the formation of the DHS–eIF5A complex. In the first instance, these information can be used to filter outthe most promising potential inhibitory compounds during a virtual screening routine and, second, to drive the design of peptides/peptidomimetics, molecules highly suitable to inhibit protein–protein interactions (D'Annessa et al., 2020).

CONCLUSION

Using a multidisciplinary approach, we have in depth-analyzed the interaction mechanism between the DHS enzyme in both human and archaeal (i.e., hDHS and aDHS). We have found that, different from hDHS, GC7 does not inhibit the activity of aDHS. Comparative analysis has shown that aDHS lacks key residues for the GC7 interaction into the active site (Glu 136, Asp243, and Asn292 that are substituted by Asp95, Thr200, and Trp248 in *S. solfataricus*). Furthermore, we have confirmed the ineffectiveness of GC7 in inhibition of both cell growth and hypusination by experimental approaches. Moreover, MetaD simulations confirm the instability of the GC7 inhibitor within the aDHS binding pocket. These data provide a detailed knowledge of the DHS-GC7 interaction, laying the foundation for the design of new specific and more efficient DHS inhibitors.

DATA AVAILABILITY STATEMENT

The original contributions presented in the study are includedin the article/**Supplementary Materials**, further inquiries can be directed to the corresponding author/s.

AUTHOR CONTRIBUTIONS

This research article was conceived by DD and AL with contributions from all authors, under the supervision of DDand AL. All authors contributed to the article and approved the submitted version.

FUNDING

The work was partially supported by funding to DD by the Fondazione Marche.

ACKNOWLEDGMENTS

We also acknowledge CINECA for the availability of high-performance computing resources as part of the agreement with the University of Milano-Bicocca.

SUPPLEMENTARY MATERIAL

The Supplementary Material for this article can be found online at: https://www.frontiersin.org/articles/10.3389/fchem.2020.609942/full#supplementary-material

REFERENCES

Abraham, M. J., Murtola, T., Schulz, R., Páll, S., Smith, J. C.,Hess, B., et al. (2015). GROMACS: High performance molecular simulations through multi-level parallelism from laptops to supercomputers. *SoftwareX* 1–2, 19–25. doi: 10.1016/j.softx.2015.06.001

Ahmed, S., Ariyaratne, M., Patel, J., Howard, A. E., Kalinoski, A., Phuntumart, V., et al. (2017). Altered expression of polyamine transporters reveals a role for spermidine in the timing of flowering and other developmental response pathways. *Plant Sci.* 258, 146–155. doi: 10.1016/j.plantsci.2016.12.002

Albers, S. V., and Meyer, B. H. (2011). The archaeal cell envelope. *Nat. Rev. Microbiol.* 9, 414–426. doi: 10.1038/nrmicro2576

Bartig, I. (1992). The archaebacterial hypusine-containing protein. Structural features suggest common ancestry with eukaryotic translation initiation factor 5A. *Eur. J. Biochem.* 758, 751–758. doi: 10.1111/j.1432-1033.1992.tb16690.x

Bas, D. C., Rogers, D. M., and Jensen, J. H. (2008). Very fast prediction and rationalization of pKa values for protein-ligand complexes. *Proteins Struct. Funct. Genet.* 73, 765–783. doi: 10.1002/prot.22102

Bassani, F., Romagnoli, A., Cacciamani, T., Amici, A., Benelli, D., Londei, P., et al. (2018). Modification of translation factor aIF5A from *Sulfolobus solfataricus*. *Extremophiles* 22, 769–780. doi: 10.1007/s00792-018-1037-4

Bassani, F., Zink, I. A., Pribasnig, T., Wolfinger, M. T., Romagnoli, A., Resch, A., et al. (2019). Indications for a moonlighting function of translation factor aIF5A in the crenarchaeum *Sulfolobus solfataricus*. *RNA Biol.* 16, 675–685. doi: 10.1080/15476286.2019.1582953

Bayly, C. I., Cieplak, P., Cornell, W. D., and Kollman, P. A. (1993). A well- behaved electrostatic potential based method using charge restraints for deriving atomic charges: the RESP model. *J. Phys. Chem.* 97, 10269–10280. doi: 10.1021/j100142a004

Benelli, D., Teana, A., La, and Londei, P. (2017). RNA metabolism and gene expression in Archaea. *RNA Metab. Gene Expr. Archaea* 32, 71–88. doi: 10.1007/978-3-319-65795-0_3

Berendsen, H. J. C., Postma, J. P. M., Gunsteren, W. F., Dinola, A., and Haak, J. R. (1984). Molecular dynamics with coupling to an external bath. *J. Chem. Phys.* 81, 3684–3690. doi: 10.1063/1.448118

Bevec, D., Jaksche, H., Oft, M., Wöhl, T., Himmelspach, M., Pacher, A., et al. (1996). Inhibition of HIV-1 replication in lymphocytes by mutants of the Rev cofactor eIF-5A. *Science* 271, 1858–1860. doi: 10.1126/science.271.5257.1858

Bhat, M., Robichaud, N., Hulea, L., Sonenberg, N., Pelletier, J., and Topisirovic, I. (2015). Targeting the translation machinery in cancer. *Nat. Rev. Drug Discov.* 14, 261–278. doi: 10.1038/nrd4505

Bussi, G., and Branduardi, D. (2015). Free-energy calculations with metadynamics: theory and practice. *Rev. Comput. Chem.* 28, 1–49. doi: 10.1002/9781118889886.ch1

Bussi, G., Donadio, D., and Parrinello, M. (2007). Canonical sampling through velocity-rescaling. *J. Chem. Phys.* 126:014101. doi: 10.1063/1.2408420

Caraglia, M., Park, M. H., Wolff, E. C., Marra, M., and Abbruzzese, A. (2013). EIF5A isoforms and cancer: two brothers for two functions? *Amino Acids* 44, 103–109. doi: 10.1007/s00726-011-1182-x

Casasnovas, R., Limongelli, V., Tiwary, P., Carloni, P., and Parrinello, M. (2017). Unbinding kinetics of a p38 MAP kinase Type II inhibitor from metadynamics simulations. *J. Am. Chem. Soc.* 139, 4780–4788. doi: 10.1021/jacs.6b12950

Chen, M., Gai, Z., Okada, C., Ye, Y., Yu, J., and Yao, M. (2020). Flexible NAD+ binding in deoxyhypusine synthase reflects the dynamic hypusine modification of translation factor IF5A. *Int. J. Mol. Sci.* 21, 1–14. doi: 10.3390/ijms211 55509

D'Annessa, I., Di Leva, F. S., La Teana, A., Novellino, E., Limongelli, V., andDi Marino, D. (2020). Bioinformatics and biosimulations as toolbox for peptides and peptidomimetics design: where are we? *Front. Mol. Biosci.* 7:66. doi: 10.3389/fmolb.2020.00066

D'Annessa, I., Raniolo, S., Limongelli, V., Di Marino, D., and Colombo, G. (2019). Ligand binding, unbinding, and allosteric effects: deciphering small- molecule modulation of HSP90. *J. Chem. Theory Comput.* 15, 6368–6381. doi: 10.1021/acs.jctc.9b00319

Darden, T., York, D., and Pedersen, L. (1993). Particle mesh Ewald: An N·log(N) method for Ewald sums in large systems. *J. Chem. Phys.* 98, 10089–10092. doi: 10.1063/1.464397

Dever, T. E., Gutierrez, E., and Shin, B. S. (2014). The hypusine-containing translation factor eIF5A. *Crit. Rev. Biochem. Mol. Biol.* 49, 413–425. doi: 10.3109/10409238.2014.939608

Di Marino, D., Chillemi, G., De Rubeis, S., Tramontano, A., Achsel, T., and Bagni, C. (2015a). MD and docking studies reveal that the functional switch of CYFIP1 is mediated by a butterfly-like motion. *J. Chem. Theory Comput.* 11, 3401–3410. doi: 10.1021/ct500431h

Di Marino, D., D'Annessa, I., Tancredi, H., Bagni, C., and Gallicchio, E. (2015b).A unique binding mode of the eukaryotic translation initiation factor 4E for guiding the design of novel peptide inhibitors. *Protein Sci.* 24, 1370–1382. doi: 10.1002/pro.2708

Hess, B., Bekker, H., Berendsen, H. J. C., and Fraaije, J. G. E. M. (1997). LINCS:a linear constraint solver for molecular simulations. *J. Comput. Chem.* 18, 1463–1472.

Hoque, M., Hanauske-Abel, H. M., Palumbo, P., Saxena, D., D'Alliessi Gandolfi,D., Park, M. H., et al. (2009). Inhibition of HIV-1 gene expression by Ciclopirox and deferiprone, drugs that prevent hypusination of eukaryotic initiation factor 5A. *Retrovirology* 6:90. doi: 10.1186/1742-4690-6-90

Jakus, J., Wolff, E. C., Myung Hee, P.ark, and Folk, J. E. (1993). Features of the spermidine-binding site of deoxyhypusine synthase as derived from inhibition studies. Effective inhibition by bis- and mono- guanylated diamines and polyamines. *J. Biol. Chem.* 268, 13151–13159.

Jansson, B. P. M., Malandrin, L., and Johansson, H. E. (2000). Cell cycle arrest in archaea by the hypusination inhibitor N1-guanyl- 1,7-diaminoheptane. *J. Bacteriol.* 182, 1158–1161. doi: 10.1128/JB.182.4.1158-1161.2000

Kaiser, A. (2012). Translational control of eIF5A in various diseases. *Amino Acids* 42, 679–684. doi: 10.1007/s00726-011-1042-8

Kaiser, A., Hammels, I., Gottwald, A., Nassar, M., Zaghloul, M. S., Motaal, B. A.,et al. (2007). Modification of eukaryotic initiation factor 5A from *Plasmodium vivax* by a truncated deoxyhypusine synthase from *Plasmodium falciparum*: anenzyme with dual enzymatic properties. *Bioorganic Med. Chem.* 15, 6200–6207. doi: 10.1016/j.bmc.2007.06.026

Kyrpides, N. C., and Woese, C. R. (1998). Universally conserved translation initiation factors. *Proc. Natl. Acad. Sci. U. S. A.* 95, 224–228. doi: 10.1073/pnas.95.1.224

Laio, A., and Gervasio, F. L. (2008). Metadynamics: a method to simulate rare events and reconstruct the free energy in biophysics, chemistry and material science. *Reports Prog. Phys.* 71:126601. doi: 10.1088/0034-4885/71/12/126601

Laio, A., and Parrinello, M. (2002). Escaping free-energy minima. *Proc. Natl. Acad. Sci. U. S. A.* 99, 12562–12566. doi: 10.1073/pnas.202427399

Laskowski, M. W., MacArthur, M. W., Moss, D. S., and Thornton, J. M. (1993). *PROCHECK: a program to check the stereochemical quality of protein structures. Appl. Crystallogr.* 26, 283–291. doi: 10.1107/S0021889892009944

Lee, C. H., Um, P. Y., and Park, M. H. (2001). Structure-function studies of human deoxyhypusine synthase: identification of amino acid residues critical for the binding of spermidine and NAD. *Biochem. J.* 355, 841–849. doi: 10.1042/bj3550841

Lee, Y., Kim, H. K., Park, H. E., Park, M. H., and Joe, Y. A. (2002). Effect of N1-guanyl-1,7-diaminoheptane, an inhibitor of deoxyhypusine synthase, on endothelial cell growth, differentiation and apoptosis. *Mol. Cell. Biochem.* 237, 69–76. doi: 10.1023/A:1016535217038

Limongelli, V., Bonomi, M., Marinelli, L., Gervasio, F. L., Cavalli, A., Novellino, E., et al. (2010). Molecular basis of cyclooxygenase enzymes (COXs) selective inhibition. *Proc. Natl. Acad. Sci. U. S. A.* 107, 5411–5416. doi: 10.1073/pnas.0913377107

Madhavi Sastry, G., Adzhigirey, M., Day, T., Annabhimoju, R., Sherman, W., Sastry, G. M., et al. (2013). Protein and ligand preparation: parameters, protocols, and influence on virtual screening enrichments. *J. Comput. Aid. Mol. Des.* 27, 221–234. doi: 10.1007/s10822-013-9644-8

Maier, B., Nadler, J. L., Raghavendra, G., Maier, B., Ogihara, T., Trace, A. P., et al. (2010). *Cadeia de regulação: efeito dos parâmetros de regulação nas características da resposta Cadeia de regulação: efeito dos parâmetros de regulação nas características da resposta Problema Cadeia de regulação: efeito dos parâmetros de regulação nas caracte*. 1, 2–4. doi: 10.1172/JCI38924

Maier, J. A., Martinez, C., Kasavajhala, K., Wickstrom, L., Hauser, K. E., and Simmerling, C. (2015). ff14SB: improving the accuracy of protein side chain and backbone parameters from ff99SB. *J. Chem. Theory Comput.* 11, 3696–3713. doi: 10.1021/acs.jctc.5b00255

Martella, M., Catalanotto, C., Talora, C., La Teana, A., Londei, P., and Benelli, D. (2020). Inhibition of eukaryotic translation initiation factor 5A (eIF5A) hypusination suppress p53 translation and alters the association of eIF5A to the ribosomes. *Int. J. Mol. Sci.* 21, 1–19. doi: 10.3390/ijms21134583

Mathews, M. B., and Hershey, J. W. B. (2015). The translation factor eIF5A and human cancer. *Biochim. Biophys. Acta Gene Regul. Mech.* 1849, 836–844.doi: 10.1016/j.bbagrm.2015.05.002

Motta, S., Minici, C., Corrada, D., Bonati, L., and Pandini, A. (2018). Ligand-induced perturbation of the HIF-2 α : ARNT dimer dynamics. *PLoS Comput. Biol.* 14:e1006021. doi: 10.1371/journal.pcbi.1006021

Nakanishi, S., and Cleveland, J. L. (2016). Targeting the polyamine-hypusine circuit for the prevention and treatment of cancer. *Amino Acids* 48, 2353–2362. doi: 10.1007/s00726-016-2275-3

Olsen, M. E., and Connor, J. H. (2017). Hypusination of eIF5A as a target for antiviral therapy. *DNA Cell Biol.* 36, 198–201. doi: 10.1089/dna.2016.3611

Park, M. H., Cooper, H. L., and Folk, J. E. (1981). Identification of hypusine, an unusual amino acid, in a protein from human lymphocytes and of spermidine as its biosynthetic precursor. *Proc. Natl. Acad. Sci. U. S. A.* 78, 2869–2873. doi: 10.1073/pnas.78.5.2869

Park, M. H., Nishimura, K., Zanelli, C. F., and Valentini, S. R. (2010). Functional significance of eIF5A and its hypusine modification ineukaryotes. *Amino Acids* 38, 491–500. doi: 10.1007/s00726-009-0408-7

Park, M. H., and Wolff, E. C. (2018). Hypusine, a polyamine-derived amino acid critical for eukaryotic translation. *J. Biol. Chem.* 293, 18710–18718. doi: 10.1074/jbc.TM118.003341

Parrinello, M., and Rahman, A. (1981). Polymorphic transitions in single crystals: a new molecular dynamics method polymorphic transitions in single crystals : a new molecular dynamics method. *J. Appl. Phys.* 52, 7182–7190. doi: 10.1063/1.328693

Provasi, D. (2019). "Ligand-binding calculations with metadynamics," in *Biomolecular Simulations. Methods in Molecular Biology*, Vol. 2022, eds M. Bonomi and C. Camilloni (New York, NY: Humana). doi: 10.1007/978-1-4939-9608-7_10

Prunetti, L., Graf, M., Blaby, I. K., Peil, L., Makkay, A. M., Starosta, A. L., et al. (2016). Deciphering the translation initiation factor 5A modification pathway in halophilic archaea. *Archaea* 2016:7316725. doi: 10.1155/2016/7316725

Rajkovic, A., and Ibba, M. (2017). Elongation factor P and the control of translation elongation. *Annu. Rev. Microbiol.* 71, 117–131. doi: 10.1146/annurev-micro-090816-093629

Rossi, D., Kuroshu, R., Zanelli, C. F., and Valentini, S. R. (2014). eIF5A and EF-P: two unique translation factors are now traveling the same road. *Wiley Interdiscip. Rev. RNA* 5, 209–222. doi: 10.1002/wrna.1211

Schultz, C. R., Geerts, D., Mooney, M., El-Khawaja, R., Koster, J., and Bachmann, A. S. (2018). Synergistic drug combination GC7/DFMO suppresses hypusine/spermidine-dependent eIF5A activation and induces apoptotic cell death in neuroblastoma. *Biochem. J.* 475, 531–545. doi: 10.1042/BCJ20170597

Söding, J., Biegert, A., and Lupas, A. N. (2005). The HHpred interactive server for protein homology detection and structure prediction. *Nucleic Acids Res.* 33, 244–248. doi: 10.1093/nar/gki408

Sonenberg, N., and Hinnebusch, A. G. (2009). Regulation of translation initiation in eukaryotes: mechanisms and biological targets. *Cell* 136, 731–745. doi: 10.1016/j.cell.2009.01.042

Tanaka, Y., Kurasawa, O., Yokota, A., Klein, M. G., Ono, K., Saito, B., et al. (2020). Discovery of novel allosteric inhibitors of deoxyhypusine synthase. *J. Med. Chem.* 63, 3215–3226. doi: 10.1021/acs.jmedchem.9b01979

Tiwary, P., Limongelli, V., Salvalaglio, M., and Parrinello, M. (2015). Kinetics of protein–ligand unbinding: predicting pathways, rates, and rate-limiting steps. *Proc. Natl. Acad. Sci. U. S. A.* 112:201424461. doi: 10.1073/pnas.1424461112

Tiwary, P., and Parrinello, M. (2015). A time-independent free energy estimator for metadynamics. *J. Phys. Chem. B* 119, 736–742. doi: 10.1021/jp504920s

Turpaev, K. T. (2018). Translation factor eIF5A, modification with hypusine and role in regulation of gene expression. eIF5A as a target for pharmacological interventions. *Biochemistry* 83, 863–873. doi: 10.1134/S00062979180 80011

Umland, T. C., Wolff, E. C., Park, M. H., and Davies, D. R. (2004). A new crystal structure of deoxyhypusine synthase reveals the configuration of the active enzyme and of an enzyme·NAD·inhibitor ternary complex. *J. Biol. Chem.* 279, 28697–28705. doi: 10.1074/jbc.M404095200

Walker, R. C., De Souza, M. M., Mercer, I. P., Gould, I. R., and Klug, D. R. (2002). Large and fast relaxations inside a protein: calculation and measurementof reorganization energies in alcohol dehydrogenase. *J. Phys. Chem. B* 106, 11658–11665. doi: 10.1021/jp0261814

Wang, J., Wang, W., Kollman, P. A., and Case, D. A. (2006). Automatic atom type and bond type perception in molecular mechanical calculations. *J. Mol. Graph. Model.* 25, 247–260. doi: 10.1016/j.jmgm.2005. 12.005

Wang, Y., Valsson, O., Tiwary, P., Parrinello, M., and Lindorff-Larsen, K. (2018). Frequency adaptive metadynamics for the calculation of rare-event kinetics. *J.Chem. Phys.* 149. doi: 10.1063/1.5024679

Wator, E., Wilk, P., and Grudnik, P. (2020). Half way to hypusine—Structural basis for substrate recognition by human deoxyhypusine synthase. *Biomolecules* 10,10–12. doi: 10.3390/biom10040522

Wiederstein, M., and Sippl, M. J. (2007). ProSA-web : interactive web service for the recognition of errors in three-dimensional structures of proteins. *Nucleic Acids Res.* 35, 407–410. doi: 10.1093/nar/g km290

Conflict of Interest: The authors declare that the research was conducted in the absence of any commercial or financial relationships that could be construed as a potential conflict of interest.

4.3 Expression and purification of *Sulfolobus islandicus* [M.16.27] deoxyhypusine synthase (DHS) in *E. coli*

In order to biochemically and structurally characterize the protein-protein complex between archaeal deoxyhypusine synthase and the initiation factor 5A, we cloned and expressed both proteins in *E. coli* systems (BL21 and Rosetta strains respectively).

ORF M1627_1306 from genomic DNA of *Sulfolobus islandicus* [M.16.27] was amplified by PCR and cloned into pQE70 vector to obtain the full-length enzyme tagged with a 6xHis-tag on C-terminus (~35 kDa) (Fig. 10 A). Previous studies from our laboratory showed that the archaeal DHS produced from pETM11 and bearing the His-tag at the N-terminus is insoluble (Bassani, 2017). The selection of a different vector which introduced the 6xHis-tag at the C-terminus greatly improved the solubility of the protein but did not completely avoid precipitation of a fraction of the protein. A further improvement in solubility was obtained by addition to the different buffers used of 80 mM Imidazole which allows the proper protein folding (Effect of imidazole on the solubility of a his-tagged antibody fragment reference). A yield of ~3.5 mg of His-tagged protein from 2 L of *E. coli* BL21 culture was obtained. In figure 10 A-D all the purification steps are represented. After the purification, the sample was analysed by DLS (Fig. 10 E) (Dynamic Light Scattering) to check the diffusion behaviour of the enzyme in solution at different temperatures (30°C and 65°C considering that DHS is from an hyperthermophilic organism). As shown in figure 10 E, DHS does not appear to be monodispersed, but on the contrary, it shows some heterogeneity depending on the temperature. At 30°C the average radius of the macromolecule was 6 nm corresponding to the tetrameric form of DHS, while at 65°C DHS shows aggregates (radius around 20 nm). A possible explanation for this might reside in the presence of the 6xHis-Tag at the C-terminus of each monomer.

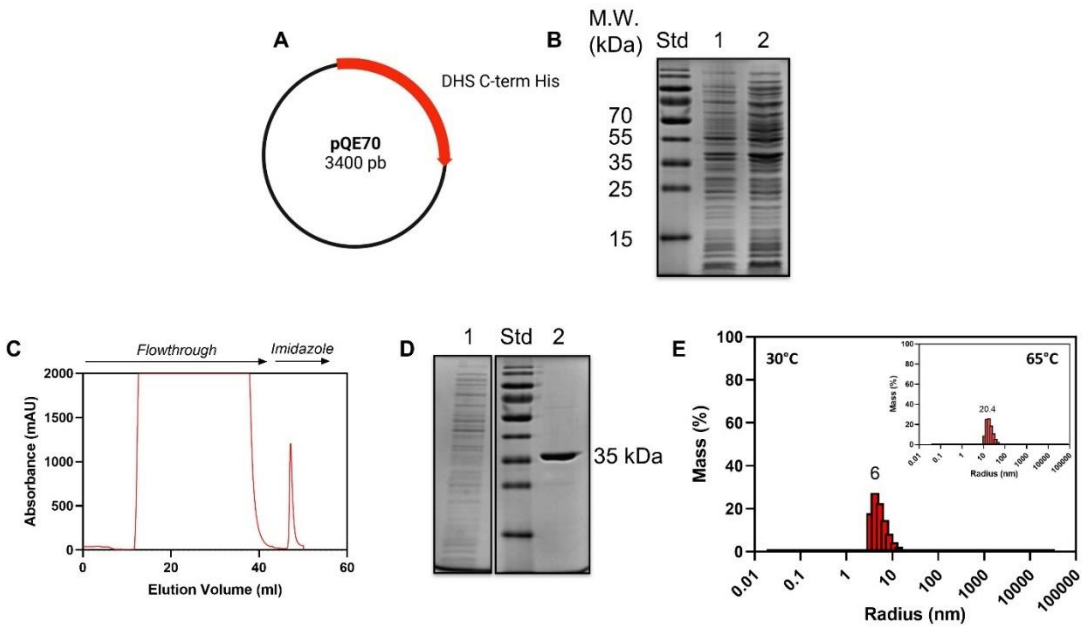

Figure 10 Expression and purification of 6xHis-DHS in E. coli.

(**A**) Schematic representation of pQE70 containing the CDS of archaeal DHS. (**B**) Lane 1: lysate before IPTG induction; lane 2: lysate after IPTG induction; 70 mOD_{600} of cells each lane, 15% SDS-PAGE gel, comassie stained. (**C**) The elution profile obtained through affinity chromatography with Ni-NTA protino (1 mL), monitored by absorbance at 280 nm, consists of two peaks, the first one is represented by the lysate flowthrough and the second one is represented by the eluted 6xHis-DHS. (**D**) Lane 1: Lysate flowthrough from the first peak in panel C; Lane 2: 3 µg of 6xHis-DHS eluate after affinity purification. (**E**) DLS analysis of the protein size distribution at 30 and 65 °C.

4.4 Expression and purification of *Sulfolobus solfataricus* [P2] initiation factor 5A (IF5A) in *E. coli*

The gene coding for the IF5A (ORF Sso0970) was PCR amplified from the *Sulfolobus solfataricus* P2 genomic DNA and it was cloned into pMCSG7 vector to obtain the full-length protein with a 6xHis-tag at the N-terminus (~15 kDa). Differently from DHS, aIF5A showed an excellent solubility both, with and without the N-terminus 6xHis-Tag. After the Ni-NTA purification (Fig. 11 C-D), 6xHis-tagged aIF5A was subjected to TEV protease digestion to cleave the 6xHis-tag (Fig. 11 E) and the protein dispersity was assessed using DLS (Fig. 11 F) at 30°C and 65°C. As shown in figure 11 F, aIF5A is almost completely monodisperse without aggregates with an average radius of 2.4 nm. In addition, at 65°C the protein has the same behaviour seen at 30°C, confirming the good quality and solubility. A yield ~20 mg of no-tagged aIF5A from 2 L of *E. coli* Rosetta culture was obtained.

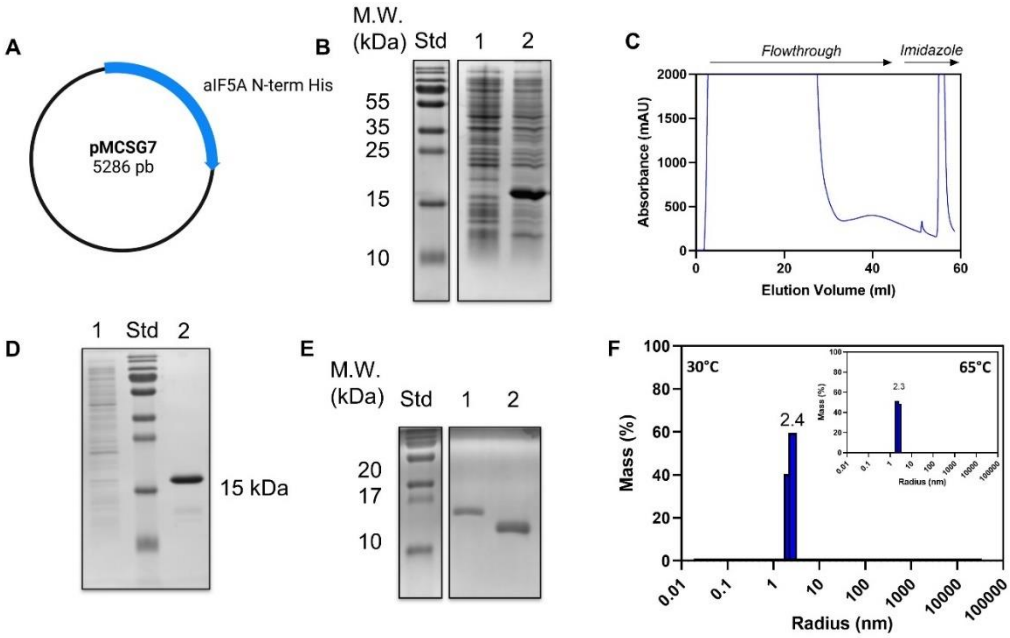

Figure 11 Expression and purification of 6xHis-aIF5A in E. coli.

(**A**) Schematic representation of pMCSG7 containing the CDS of archaeal aIF5A. (**B**) Lane 1: lysate before IPTG induction; lane 2: lysate after IPTG induction; 70 mOD_{600} of cells each lane, 15% SDS-PAGE gel, comassie stained. (**C**) The elution profile obtained through affinity chromatography with Ni-NTA protino (1 mL), monitored by absorbance at 280 nm, consists of two peaks, the first one is represented by the lysate flowthrough and the second one is represented by the eluted 6xHis-aIF5A. (**D**) Lane 1: Flowthrough from the first peak in panel C; Lane 2: 3 µg of 6xHis-aIF5A eluate after affinity purification. (**E**) Lane 1: 2 µg of 6xHis-aIF5A; Lane 2: 4 µg of digested aIF5A (**F**) DLS analysis of the protein size distribution at 30 and 65 °C.

4.5 DHS and aIF5A form a complex in vitro

Even though, the three-dimensional structure of the DHS-IF5A complex has not been solved yet, it was clearly demonstrated that the two proteins, both from Eukarya and Archaea, are able to interact forming a complex *in vitro (Bassani 2018 and Park 1999).* To confirm these data with our recombinant proteins, we have performed size-exclusion chromatography (Fig. 12 A-D) as well as, non-denaturing gel electrophoresis to see the formation of the complex under native conditions (Fig. 12 E). To confirm the complex formation, a size-exclusion chromatography was performed using a Superdex 200 increase 5/150 GL column. 6xHis-Tag-DHS and 6xHis-aIF5A were firstly loaded individually (Fig. 12 A-B), to detect their characteristic elution volume, and then loaded together after a short incubation in a molar ratio of 1:1 (Fig. 12 C). All samples were treated in the same conditions, and their elution profiles have been superimposed (Fig. 12 D). Clearly, the sample containing the two proteins pre-incubated together (green peak in figure 12 C, D) shows an elution profile with a peak corresponding to a slightly higher molecular weight position compared to the peak corresponding to the His-tagged DHS alone proving the formation of the complex. The small peak (elution volume around 2.2 ml) in the complex sample (Fig. 12 C) correspond to the excess of aIF5A.

Non-denaturing gel electrophoresis was performed to evaluate again the formation of the complex between DHS and the substrate aIF5A, (Fig. 12 D). Since the theoretical pI of the enzyme DHS (6.5) is close to that of aIF5A (6.15), molecular size should be the major factor determining the electrophoretic mobility of these proteins during the native-gel electrophoresis. As expected, the tetrameric DHS was separated from smaller aIF5A upon native gel electrophoresis (Figure 12 D). In a mixture containing the 6xHis-DHS and aIF5A at a molar ratio of 1:0.5 (DHS:aIF5A), in the lane of the

complex, a new slower migrating protein band was observed confirming the formation of the complex.

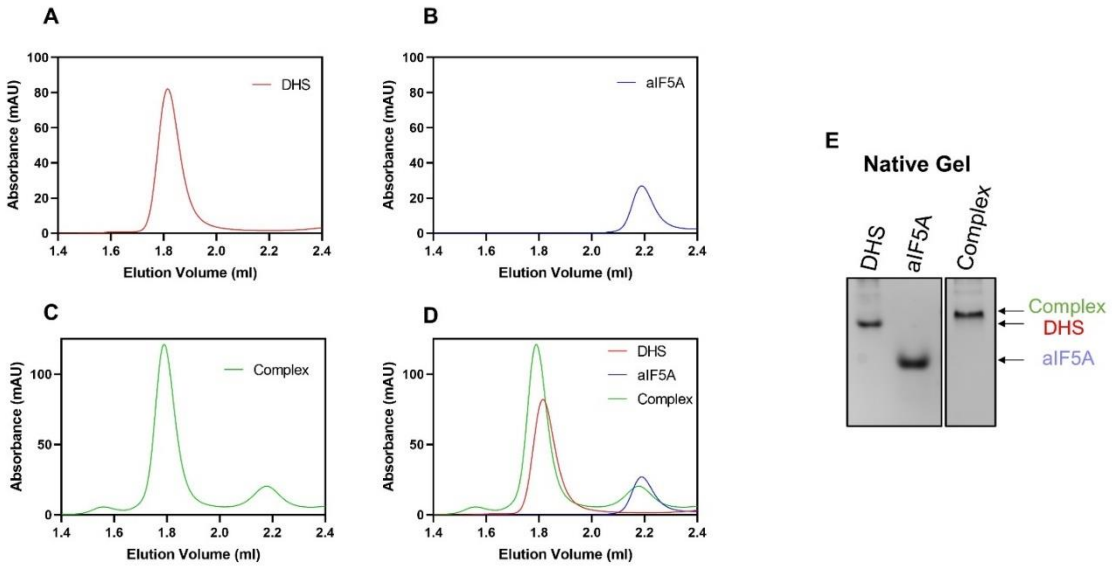

Figure 12 DHS and aIF5A form a complex in vitro.

(**A**) Elution profile obtained through size-exclusion chromatography of 6xHis-DHS (20 µg) using a Superdex 200 5/150 column. (**B**) Elution profile obtained through size-exclusion chromatography of 6xHis-aIF5A (20 µg) using a Superdex 200 5/150 column. (**C**) Elution profile obtained through size-exclusion chromatography of 6xHis-DHS (20 µg) incubated together with 6xHis-aIF5A (20 µg) using a Superdex 200 5/150 column. (**D**) Superimposition of each previous elution profiles. (**E**) Native-PAGE electrophoresis on 10% native gel. Lane 1: 6xHis-DHS alone, 2.5 µg; lane 2: aIF5A alone, 2.5 µg; lane 3: 6xHis-DHS plus aIF5A, molar ratio 1:0.5.

4.6 Isothermal Titration Calorimetry (ITC) analysis of the aIF5A-aDHS complex

In order to get insights into the binding mechanism of aDHS-aIF5A complex, we have performed ITC analysis (Fig. 13 A, E). ITC can determine all the thermodynamic parameters of a binding interaction in one experiment. ITC measurements were performed at 30°C and not at higher temperatures because of the poor stability and solubility of DHS (Fig. 11 E). Fitting of ITC binding curve (Fig. 13 A) will provide binding affinity (K_D), reaction stoichiometry (n), enthalpy (ΔH) and entropy (ΔS) of the complex (Fig. 13 B-C-E). The resulting parameters are summarized in figure 13 E and plotted in figure 13 C for an easier representation. The ITC profile in figure 13 A shows an exothermic signal and the DHS-aIF5A interaction at this temperature displays a dissociation constant (K_D) of 3.155 μM. The DHS-aIF5A binding is characterized by a favourable enthalpy change (ΔH: −13.05 ± 0.21 kcal.mol−1) and an unfavourable entropy change (−TΔS: 5.37 ± 0.29 kcal.mol−1). The favourable enthalpy (ΔH < 0) observed indicates that the binding is driven by the formation of hydrogen and other noncovalent bonds (e.g., Van Der Waals forces). In contrast, the entropic difference suggests a loss of conformational freedom (−TΔS > 0). Interestingly, the number of ligand binding sites are about 0.5 for each DHS monomers (Fig. 13 E). Considering that the active form of DHS is a tetramer, for 1 enzyme there are two aIF5A binding the DHS. Using the Affinimeter-ITC-Advanced software it was also possible to trace the association and dissociation rate constant (Kon and Koff) (Fig. 13 D) of the complex. After the ITC analyses, the sample was recovered and concentrated to ~7 mg/ml using an Amicon Ultra 10 kDa for subsequent preliminary crystallization trials.

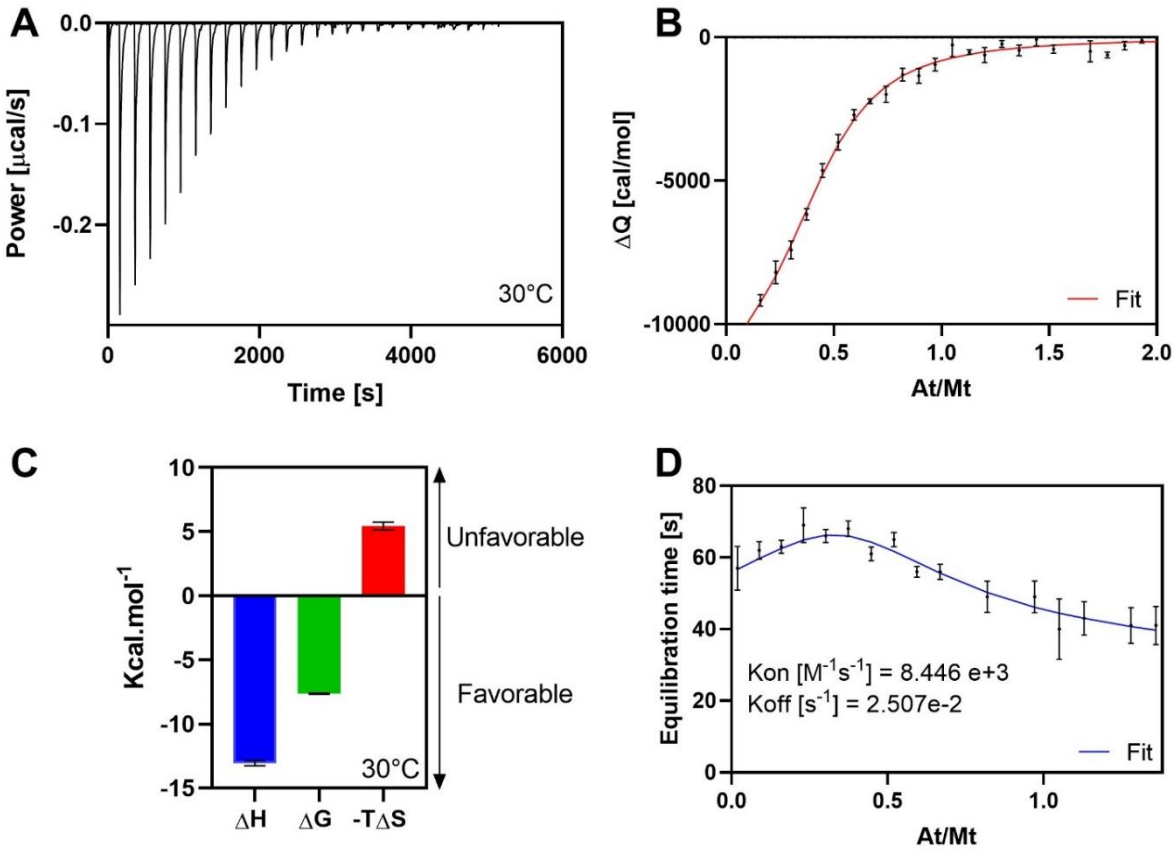

E

Thermodinamyc Parameters

Kd [µM]	ΔG [kcal/mol]	ΔH [kcal/mol]	-TΔS [kcal/mol]	n° sites
3.155 ± 0.212	-7.63 ± 0.042	-13.05 ± 0.21	5.37 ± 0.29	0.49.5 ± 0.02

Figure 13 Thermodynamic parameters of aIF5A-DHS complex.

(**A**) raw titration curve with its baseline; (**B**) Integrated heats for each injection after baseline correction and theoretical curve obtained by the "global thermodynamic treatment"; (**C**) graphical representation of thermodynamics parameters; (**D**) integrated curve showing kinetics (kon and koff) parameters; (**E**) summary of thermodynamic parameters obtained by ITC experiments. n=3.

4.7 Setting up of complex purification protocols:

Aiming at obtaining samples of the complex devoid of free proteins and which could be suitable for crystallization, we have fine-tuned two different purification protocols.

4.7.1 Protocol A

The first protocols exploit the his-tag present at the C-terminus of DHS. After the incubation of the two single proteins, aDHS and aIF5A devoid of its His-tag, and the subsequent complex formation, a Ni-NTA affinity chromatography (Fig. 14 A) was used to separate the complex (Fig. 14 B Peak II) from the excess of free aIF5A (Fig. 14 B peak I). The Ni-NTA agarose beads have retained the complex that was subsequently eluted using a high concentration of Imidazole (250 mM). Two aliquots from these fractions were loaded in an SDS-PAGE and visualized by Comassie staining (Fig. 14 C). As shown in figure 14 C, the first peak of the chromatogram mainly contains free aIF5A (the predicted M.W. of the protein without His-tag is ~14 kDa), while the second peak contained the purified complex as proved by the presence on the SDS-PAGE of both protein bands (Fig. 14 C). The purified complex was, then, analysed by DLS (Fig. 14 D). In contrast with the results obtained with the isolated DHS, at a temperature of 65°C, the complex did not show any aggregation, suggesting that the presence of the ligand aIF5A, contributes to the correct folding of the enzyme increasing its solubility. The complex was then concentrated to 10 mg/ml using an Amicon Ultra 10 kDa. This purification protocol has allowed to obtain a large amount of purified complex which has been used to conduct a preliminary crystallization screening in parallel with the sample from ITC.

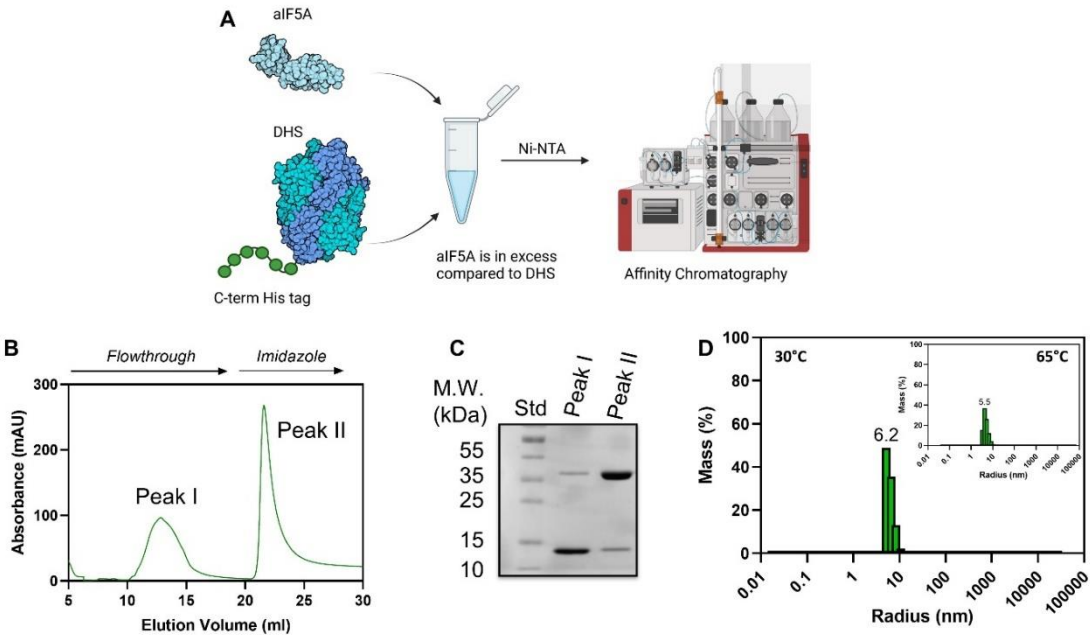

Figure 14 In-vitro purification of 6xHis-DHS-aIF5A complex.

(**A**) Schematic representation of each step of purification. (**B**) The elution profile obtained through affinity chromatography with Ni-NTA protino (1 mL), monitored by absorbance at 280 nm, consists of two peaks, the first one is represented by the excess of non-tagged aIF5A and the second one is represented by the eluted 6xHis-DHS-aIF5A complex. (**C**) Lane 1: 3 µg of peak I fraction; Lane 2: 3 µg of peak II fraction. (**D**) DLS analysis of the protein size distribution at 30 and 65 °C.

4.7.2 Protocol B

The presence of histidine tags in recombinant proteins have, often, no significant effect on the native three-dimensional conformation of a protein and, therefore, need not to be removed for crystallization (Carson et al., 2007).

In our case, however, an influence of the his-tag on the solubility of DHS was quite clear. Therefore, we thought that removing the his-tag from the enzyme would provide a complex more suitable for both crystallization and successive biochemical analyses. Considering that plasmid pQE70 is lacking a protease cleavage-site before the his-tag, we have substitute, using the QuickChange mutagenesis protocol, two nucleotides to create a stop codon (TAA) preceding the His-Tag sequence (Fig. 15 A). Two different *E. coli* cultures carrying the two recombinant plasmid (aDHS bearing the stop codon and 6xHis-aIF5A) after induction, were pooled and recovered by centrifugation forming a single cell pellet (Fig. 15 B). After disruption of the cells, the lysate was loaded into a Ni-NTA protino column using a AKTA chromatography system (Fig. 15 B-C-D) to purify 6xHis-aIF5A and all the DHS bound to it. The purified sample was then incubated overnight with TEV protease to cleave the 6xHis-tag present on aIF5A in order to get a DHS-aIF5A complex free of purification tags (Fig. 15 E, F). Finally, to obtain the purified complex without any excess of one of the two proteins, the sample was concentrated to a final volume of 500 µL and loaded into a Superdex 200 10/300. Size-Exclusion Chromatography (SEC) (see materials and methods for more details) allowed the separation of the complex (first peak in Fig. 15 G and first lane in Fig. 15 E) from the excess of aIF5A (second peak in Fig. 15 G and second lane in Fig. 15 E). The dispersity of the sample was assessed using DLS (Fig. 15 F). The purified complex was monodispersed and free of aggregates with an average radius of the particle of 5.9 nm. This protocol has represented an excellent method to purify a soluble

and monodisperse DHS-aIF5A complex suitable for next structural and biochemical analyses.

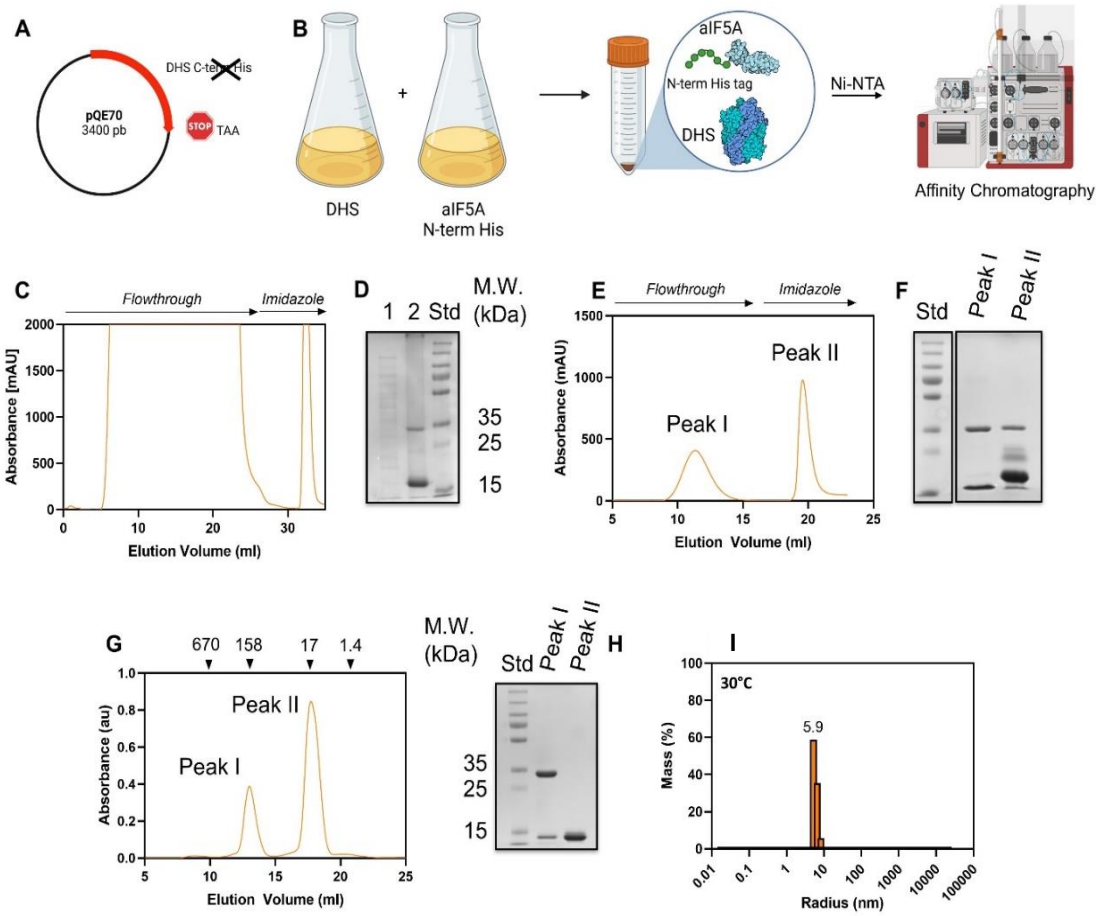

Figure 15 In-vitro purification of DHS-aIF5A complex.

(**A**) Schematic representation of pQE70 containing the CDS of archaeal DHS, his tag was excluded from the aminoacidic sequence by adding a stop codon just before the his-tag codon. (**B**) Schematic representation of each step of purification; from E. coli cultures to AKTA chromatography (**C**) The elution profile obtained through affinity chromatography with Ni-NTA protino (1 mL), monitored by absorbance at 280 nm, consists of two peaks, the first one is represented by the lysate flowthrough and the second one is represented by the eluted DHS-aIF5A-6xHis complex. (**D**) Lane 1: 3 µg of flowthrough fraction from panel C; Lane 2: 3 µg of eluted fraction from panel C. (**E**) The elution profile obtained through affinity chromatography with Ni-NTA protino (1 mL), monitored by absorbance at 280 nm, consists of two peaks, the first one is represented by the DHS-aIF5A complex and the second one is represented by the eluted 6xHis-aI5A, His-TEV and DHS. (**F**) Lane 1: 3 µg of flowthrough fraction (peak I) from panel E; Lane 2: 3 µg of eluted fraction (peak II) from panel E.

(**G**) Elution profile obtained through size-exclusion chromatography of DHS-aIF5A previously purified through affinity chromatography, using a Superdex 200 10/300 column. (**H**) Lane 1: 3 µg of peak I sample from panel G; Lane 2: 3 µg of peak II sample from panel G. (**I**) DLS analysis of the protein size distribution at 30°C.

4.8 aIF5A-DHS complex structure

The structure of aIF5A-DHS complex was determined by molecular replacement using the Protein Data Bank (PDB) ID 6XXH as a search model for DHS and PDB ID 3CPF for aIF5A and refined using the Phenix refine package to a final resolution of 2.2 Å.

aIF5A-DHS complex crystallized in the $P2_12_12_1$ space group and it is composed by a DHS tetramer with four different aIF5A bound to it (Fig. 16), one for each active site. In addition, four NAD molecules are present inside the active sites of the enzyme and were localized by Fourier difference maps (Fig. 18).

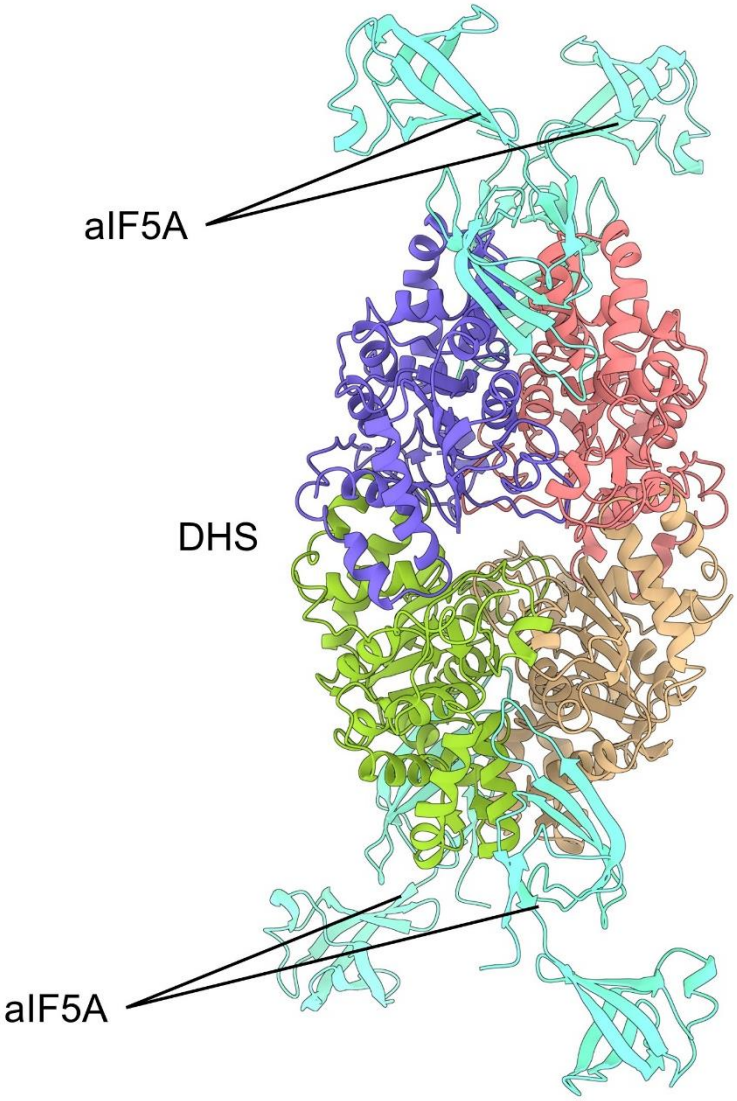

Figure 16 Three-dimensional organization of aIF5A-DHS complex.

Front view of the aIF5A-DHS complex, with each DHS monomer represented using different colour; the 4 labelled aIF5A molecules are represented by the same colour.

4.9 Overall structure of *S. islandicus* DHS

To better understand the details of the interaction occurring between aIF5A and DHS, first it is important to describe the three-dimensional structure of the two single proteins.

In agreement with all the DHS structures available (Liao et al., 1998; Umland et al., 2004; Chen et al., 2020; Wątor et al., 2020), also *S. islandicus* DHS exists as a homotetramer with four monomers related by 222 symmetry (Fig. 17). The tetramer is formed by two tightly associated dimers per asymmetric unit. The enzyme can be defined as a dimer of dimers (A1-B1, B2-A2) with two different active sites located at each dimer interface (Fig. 17). The active site is composed by residues from each of the two monomers, with one providing residues for deoxyhypusination reaction and the other providing the binding site for NAD. This organization is reported in literature as the active form of the protein (Liao et al., 1998), confirming that our structure is not a crystallization artefact (Fig. 16).

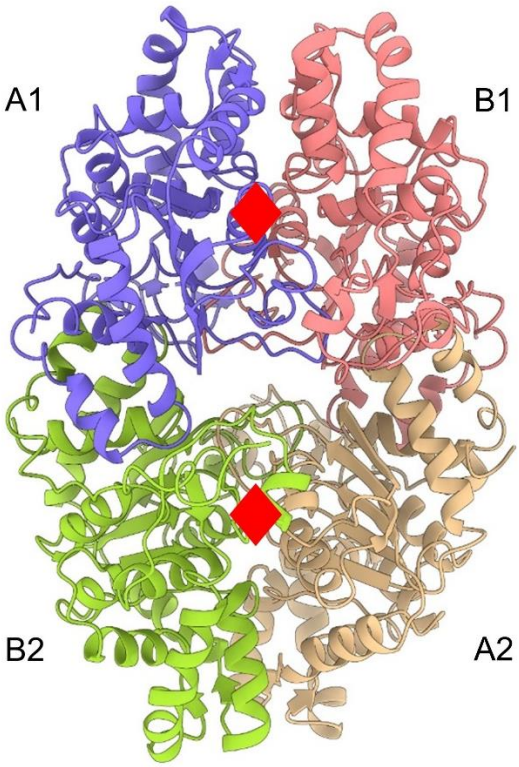

Figure 17 S. islandicus DHS crystal structures.

Front view of the DHS tetramer with red diamonds indicating the location of the active sites at each dimer interface.

The core of each monomer contains a Rossman fold, typical of most dehydrogenases (Bell et al., 1997), composed of 6 parallel β-strands (βA- βB- βC- βD- βE- βF Fig. 18), which are involved in interaction with NAD into the active site.

Moreover, there are 18 (α1-α18) helices and 4 additional β-strands (β1- β2- β3- β4) which define the ultimate organization of the structure (Fig. 18 B).

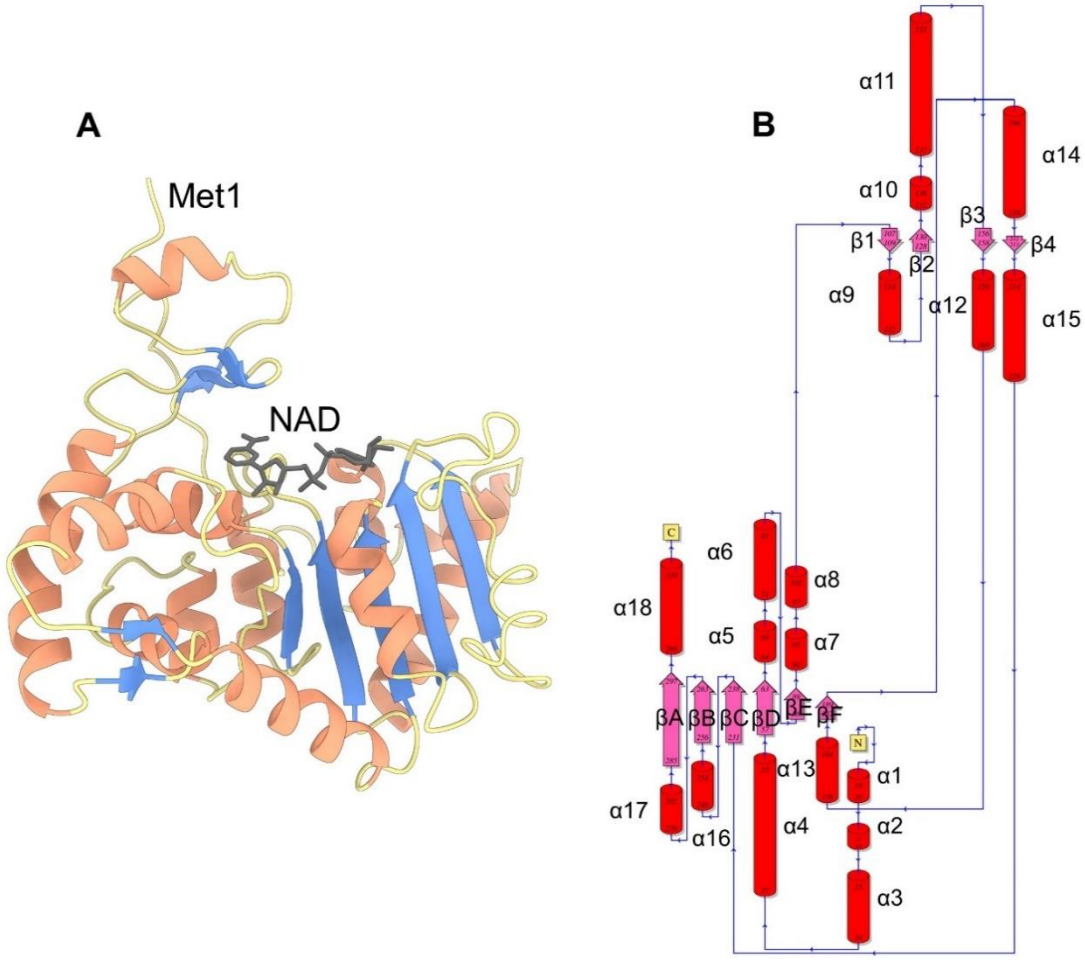

Figure 18 The topology of DHS monomer.

(**A**) Ribbon representation of the monomer of DHS with bound NAD (shown as a dark grey stick model). (**B**) Schematic diagram of the DHS monomer secondary structure. The β-strands that are part of the Rossmann fold are given sequentially with capitol letter from the N-terminal end (βA, βB, etc.), while those outside the fold are numbered (β1, β2, β3, β4); α-helix are numbered sequentially from the N-terminal.

The N-terminal end of each DHS monomer contains a two-turn α-helix (α1), composed of residues Asn3-Lys9, that represents the "ball" of the previously described ball-and-chain motif (Liao et al., 1998). Liao and colleagues (Liao et al., 1998) described for the first time the structure of the human DHS in which the ball-and-chain motif was located on the entrance of the active sites. In our case, the motif is positioned just below the active sites letting free aIF5A to bind the enzyme.

Each subunit interacts with other two monomers. For a better explanation, if we consider A1, it interacts with B1 to form the homodimer and B2, which in turn interacts with A2, to complete the tetramer organization (Fig. 17). A1-B1 interaction involved 25 hydrogen bonds and 17 salt bridges and presents a buried area of 2324.4 $Å^2$ (Fig. 19 A), while the buried surface of A1-B2 is smaller and it is 1694 $Å^2$ (Fig. 19 B) and involved 21 hydrogen bonds and 6 salt bridges.

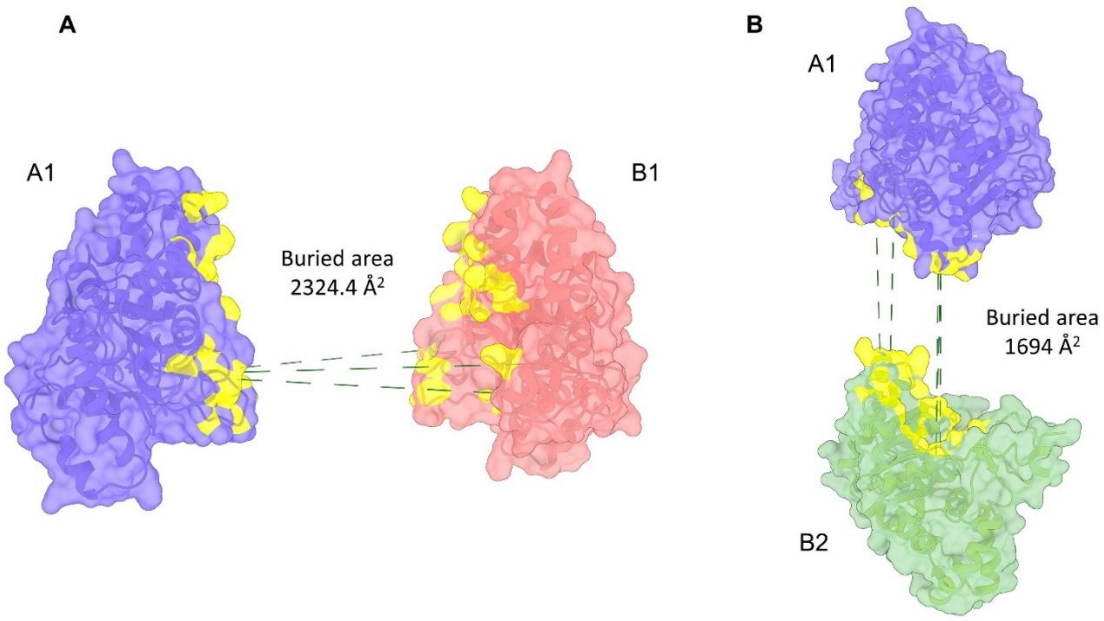

Figure 19 DHS monomers form tightly associated homodimers.

(**A**) Schematic representation of the interaction surface between A1 and B1 DHS monomers obtained by splitting the two subunits; (**B**) Schematic representation of interaction surface between A1 and B2 DHS monomers obtained by splitting the two subunits; Interaction surface is shown in yellow, and the measured buried areas are also reported for both panels.

Similarly to human enzyme, also *S. islandicus* DHS active site presents interesting features. The site is accessed from the surface by a funnel which contracts to a thin tunnel at a level corresponding to the positions of the nicotinamide ring of NAD and the sidechain of Lys288, that is equivalent to conserved Lys329 in human DHS (Umland et al., 2004; Kim et al., 2018), and then opens into a long internal and large chamber. The distance between the end of the tunnel and the surface is 23.737 Å measured from Phe233 of monomer A1 to Thr263 of monomer B1. At the end of this cavity there is the NAD-binding site where NAD is bound and completely buried into the dimer interface. In addition to NAD, the active site is supposed to allocate also one spermidine molecule.

As shown in figure 20, the two NAD molecules are very close to each other, at the mid-level of the interface located within a distance of 3.36 Å between the two O3' atoms. Each NAD molecule forms hydrogen bonds with 10 residues on one monomer A1 (or B2) and one with the monomer B1 (or A2) present on the other side of the dimer interface (Fig. 20). In detail, the adenine ring forms hydrogen bonds with Asn65, Asp298 and Ala299 of the A1 monomer. At the level of pyrophosphate, hydrogen bonds are formed with residues Ala64 and Thr90 from A1 and Leu 272 and Ser273 from B1 (Fig. 20). Interestingly, the ribose is involved in an additional hydrogen bond with the opposite NAD molecule in the same region. The nicotinamide ring forms hydrogen bonds involving His96, Gly92, Asp195 from A1 monomer (Fig. 20). The same happens in a specular way for the other pair of dimers (B2, A2) and the other two molecules of NAD.

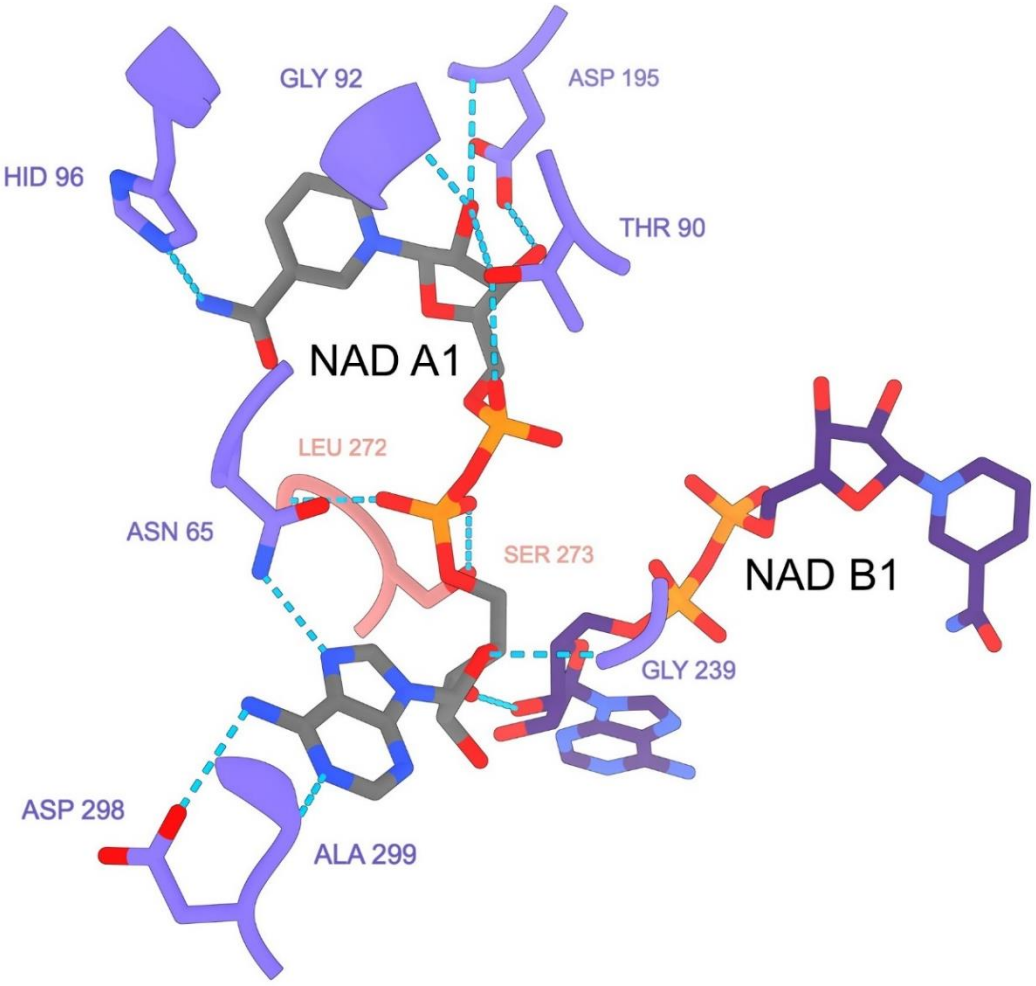

Figure 20 NAD molecule forms a dense interaction network with residues from both monomers.

Close-up view of binary DHS-nicotinamide adenine dinucleotide (NAD) complex. Two NAD molecules (NAD A1 and NAD B1) are bound symmetrically and coordinated by residues from both subunits. The co-factor, as well as residued from chain A1 and B1 are shown as sticks with different colors (Violet for A1 residues and Salmon for B1 residues).

4.10 Overall structure of *S. solfataricus* aIF5A

Eukaryotic Initiation factor 5A is reported in literature as a single protein composed of two domains linked by an inter-boundary loop (Tong et al., 2009).

C-terminal domain of our aIF5A is present (as confirmed by SDS-PAGE and Size-Exclusion Chromatography (Fig. 11 and 12)) but not visible in electron density of our complex structure. On the other hand, the N-terminal domain (from Met1 tot to Ile69) in which is located the specific lysine (Lys36) that undergoes hypusination, is clearly visible in electron density maps (Fig. 21).

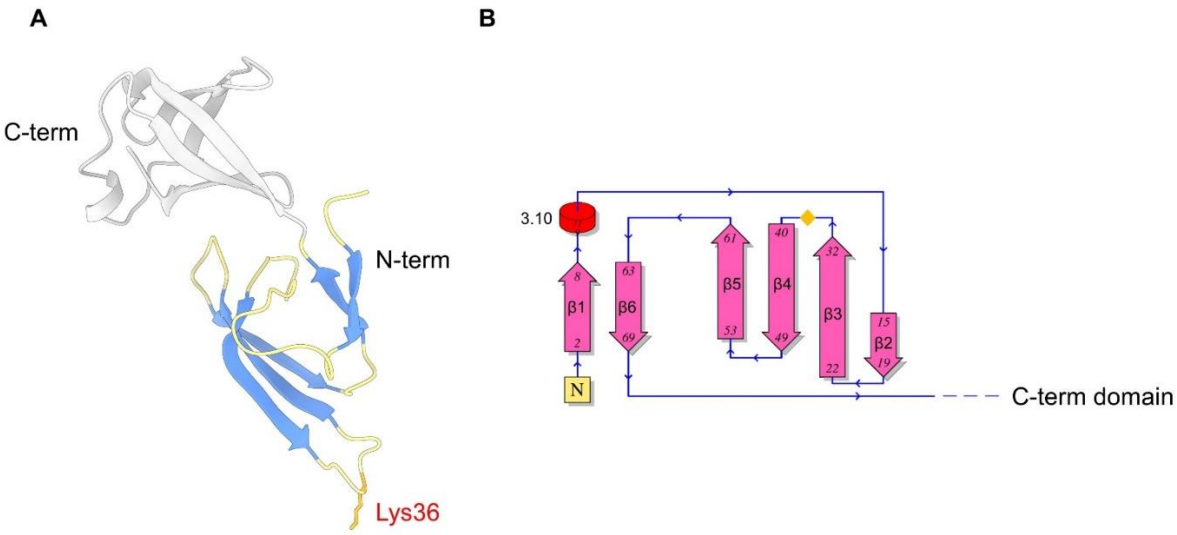

Figure 21 The topology of N-terminal domain of S. solfataricus aIF5A.

(**A**) Ribbon representation of *S. solfataricus* aIF5A coloured by secondary structure; Lys36 is in red and label; the C-terminal domain (in light grey) is a prediction. (**B**) Schematic diagram of the aIF5A secondary structure; β-strands are numbered sequentially from the N-terminal end (β1, β2, etc); Lys 36 position is represented by an orange diamond.

The N-terminal domain of *S. solfataricus* aIF5A is structurally highly conserved with the human one (RMSD 0.765 Å between our N-terminal aIF5A with N-terminal human eIF5A PDB: 3CPF) (Fig. 22) and forms a SRC Homology 3 Domain (or SH3 domain).

It is composed mainly of β-strands (Fig. 21). As shown in figure 21 strands β1 and β6 form a double stranded, anti-parallel sheet and β2- β3- β4- β5 form a four-stranded, twisted, anti-parallel sheet at the opposite side of the domain. The loop connecting β1 and β2 comprises a one-turn 3_{10}-helix (residues Val8-Glu10). The loop connecting β3 and β4 contains the hypusination site, Lys36, called hypusine-containinng loop.

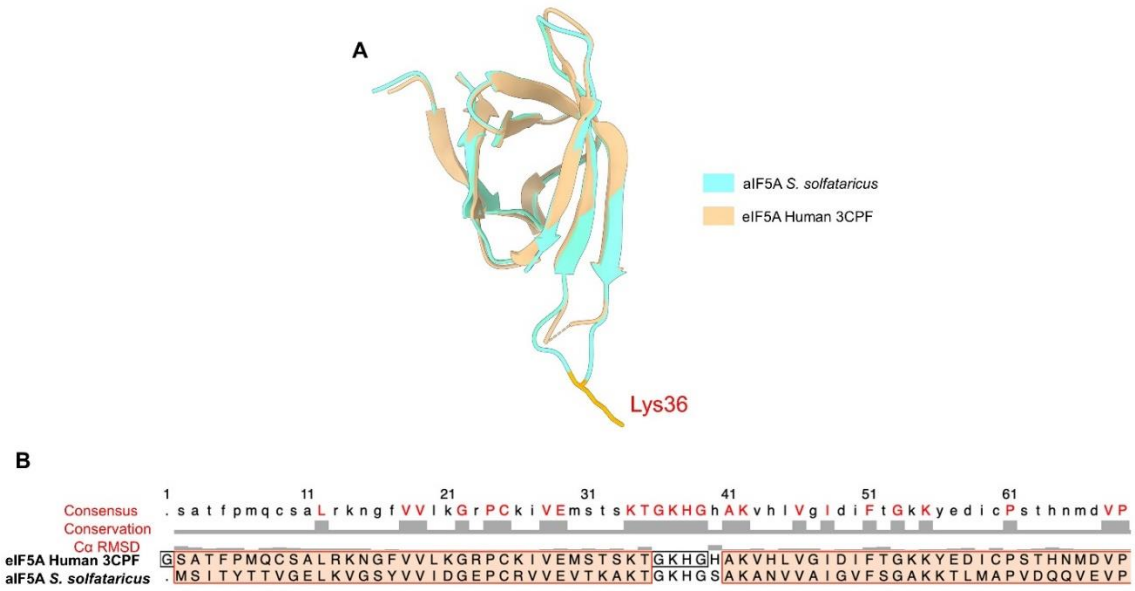

Figure 22 Structure of human eIF5A and S. solfataricus aIF5A N-terminal domains are highly conserved.

(**A**) Structural superimposition of N-terminal domain of *S. solfataricus* aIF5A (aquamarine), and human eIF5A (PDB 3CPF; khaki); (**B**) Sequence alignment of N-terminal domain of *S. solfataricus* aIF5A and human eIF5A (3CPF). The structurally conserved residues are represented into a salmon box; red letters in the consensus line represent conserved residues.

4.11 Structural details of aIF5A-DHS complex

The structures of the two proteins are highly conserved between human and other eukaryal and archaeal organisms (Umland et al., 2004; Tong et al., 2009; Chen et al., 2020; Wątor et al., 2020) and the structures of single proteins are described, anyway the aIF5A-DHS complex organization is not known yet. We describe for the first time the topological organization of aIF5A-DHS complex. As mentioned before, 4 different aIF5A molecules bind to the 4 DHS active sites situated at each dimer interface.

From a spatial point of view, aIF5A approaches the enzyme in a vertical way with the N-terminal domain leaning on the dimer interface of the enzyme (Fig. 16) and forming a buried area of 608.1 Å and 542.9 Å with A1 and B1 monomers respectively (Fig. 23 A).

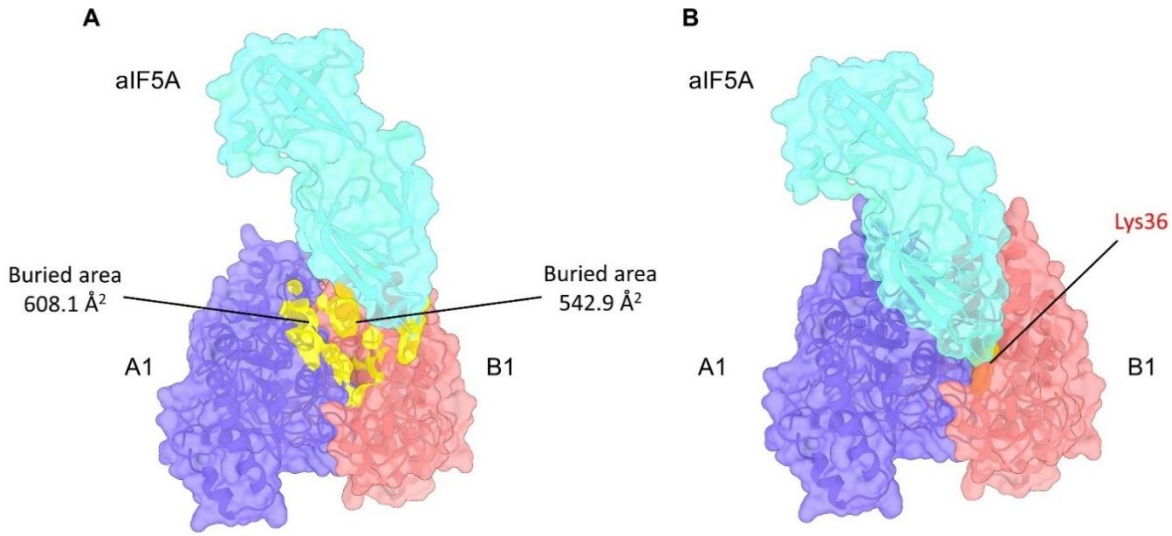

Figure 23 aIF5A bind DHS at the dimer interface.

(**A**) Schematic representation of interaction surface between DHS-dimer A1-B1 and aIF5A obtained by splitting the proteins; interaction surface is shown in yellow. (**B**) Front view of DHS-dimer A1-B1 interacting with one aIF5A; Lys36, label in red, is inserted into the cavity between the two dimers.

aIF5A anti-parallel β-sheet comprising β2- β3- β4- β5 and the hypusine-containing loop, at the base of N-terminus, form the centre of the interactions that involves two helices (α11 and α14) for DHS monomers present at dimer interface (for a total of 4 helices). More in detail, aIF5A interacts with DHS through 5 H-bonds, 3 of them involve monomer A1 (Gln251-His37; Ser282-Lys36; Asp224-Thr56), and 2 of them involve B1 (Gln 207-Met 58; Gln207-Met58) (Fig. 24).

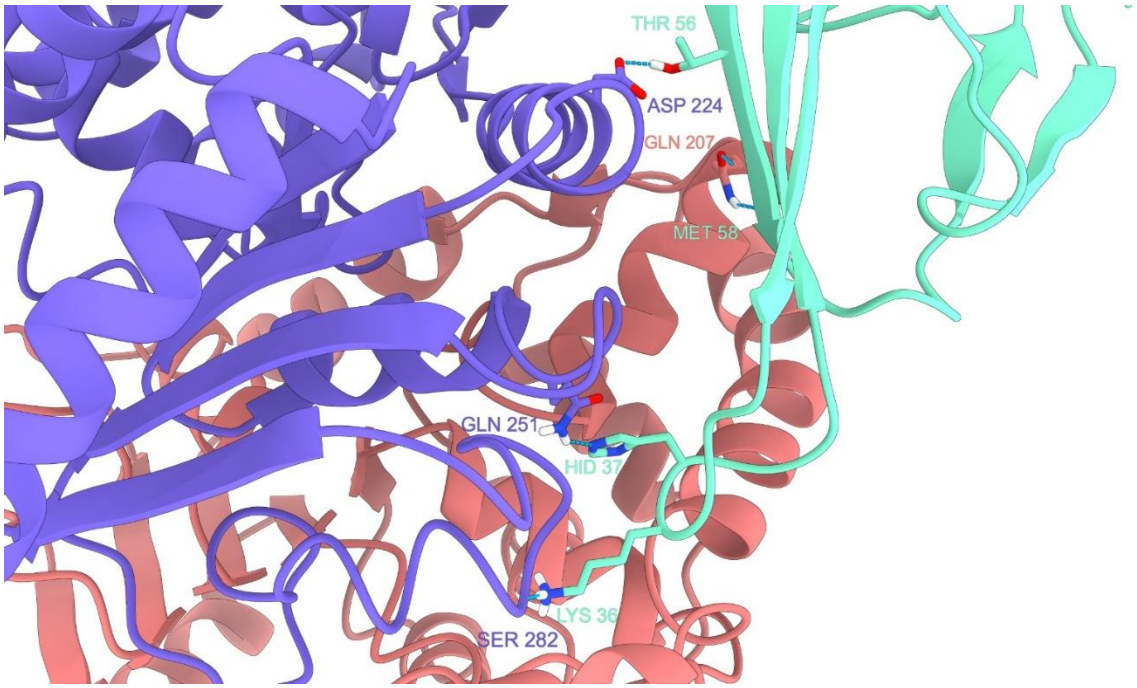

Figure 24 aIF5A interacts with DHS through a H-bond network.

Predicted hydrogen-bonding amino acids; the amino acids predicted to form hydrogen bonds are shown in a stick representation in aquamarine for aIF5A, in light red for monomer B1 and in blu for monomer A1, with the predicted hydrogen bonds shown as light blue dotted lines

This interaction leads the side chain of Lys36 (that undergoes hypusination) to enter in the narrow tunnel of the enzyme active sites through the funnel that separates the surface from the internal cavity of DHS (Fig. 23 B).

Within this funnel the specific aIF5A lysine (Lys36) will be modified in deoxyhypusine using spermidine as substrate and NAD as cofactor.

5 DISCUSSION

The aim of this work was to characterize in detail the biochemical and structural features of two proteins, the translation factor aIF5A and the first enzyme involved in its post-translational modification DHS, and of the complex between them, in order to get information useful, in the future, for the design of innovative therapeutic molecules.

Initiation factor 5A belongs to the small group of universally conserved translation factors: the protein is homologous between Eukarya and Archaea while Prokaryotes bear an orthologue protein called EF-P.

The eukaryotic protein performs functions at different levels of translation, but the main task is the promotion of the synthesis of proteins containing successive residues of proline. These types of peptide sequences would cause the ribosome to stall, while eIF5A bound on the ribosomes and interacting with the P-site tRNA, facilitates, in this way, Pro-Pro peptide bond formation.

Hypusination, its unique post-translation modification, is essential for this activity. The reaction is carried out through two different enzyme reactions, the first one catalyzed by DHS while the second one by DOHH. DHS, as well as eIF5A is conserved between Eukarya and Archaea domains.

As many other translation factors, also eIF5A is highly involved in different pathologies such as cancer, HIV-1 infection, diabetes and malaria. Considering its involvement in pathologies, together with its unique and specific post-translational modification, eIF5A and the enzymes involved in the hypusination pathway are considered very interesting therapeutic targets leading researchers to search for new inhibitory molecules. To do that, the biochemical and structural characterization of the proteins involved are strictly necessary.

In the first part of the project, we focused on the study of N1-guanyl-1,7-diaminoheptane (GC7), the most potent DHS inhibitor. This spermidine analogue is able to block hypusination but, according to several reports (to review see Turpaev, 2018), it is not sufficiently selective and specific to be used in clinical. Although its effect is well characterized on eukaryotic cells, GC7 shows a different behaviour on distinct archaeal organisms (Jansson et al., 2000), despite the enzyme conservation.

Starting from this consideration and driven by the idea that knowing the molecular determinants of the GC7 binding in homologous proteins can open new frontiers for the design of inhibitors specific for hypusination, we characterized both human and archaeal (*S. solfataricus* system) DHS-GC7 interaction. We started by using a multidisciplinary and comparative approach. The first hypusination step involving DHS is strongly conserved among *H. sapiens* and *S. solfataricus* (Bassani et al., 2018). In order to compare the structure of the two proteins, we have obtained the 3D-organization of *S. solfataricus* DHS through homology modelling, using the human DHS structure as template (PDB: IRQD). Similarly to the human enzyme (hDHS), also archaeal DHS (aDHS) presents the active site within a deep narrow tunnel at a dimer interface.

Interestingly, regardless of the functional conservation between the two enzymes, some of the residues forming the GC7 binding site in aDHS are different from the corresponding ones in hDHS. In particular, two of them would seem to be relevant for the correct interaction between protein and GC7: Asp316 in hDHS is substituted by Leu272 in aDHS in the GC7 guanidinium region and Asp243 present in hDHS is substituted by Thr200 in aDHS in the amine region of the ligand. Lack of Asp243 in aDHS could be important for

the correct interaction with GC7 since Thr200 is not able to form a salt bridge with the inhibitor.

Based on these results, we decided to evaluate the binding stability of the GC7 in the two different models using MetaD simulations. The results emphasized a significantly higher residence time of GC7 in the hDHS compared to the *S. solfataricus* one, indicating a lower stability of the complex between the inhibitor and the thermophilic enzyme, a result which could be explained by the different interaction network.

To confirm these data, we planned and performed a series of experiments with the aim to investigate if GC7 was able to inhibit *in vivo S. solfataricus* cell growth and aIF5A hypusination. The experimental data have shown that, in contrast to the human model (Nakanishi and Cleveland, 2016; Schultz et al., 2018a; Martella et al., 2020), GC7 appears to be unable to inhibit *S. solfataricus* cell growth and aIF5A hypusination confirming the computational results.

Therefore, we propose that the ineffectiveness of GC7 on the archaeal model may be due to not only to the different growth conditions but also to the aminoacidic composition of the binding site compared to *H. sapiens* model. The identification of the amino acid residues differing between the two GC7 binding sites will be of great help in the design of new inhibitors based on GC7 structure.

In addition, the MetaD simulations conducted on the human enzyme evidenced, for the first time, two different unbinding paths of the inhibitor. The first path named path A, occurs more frequently (70%) in the simulation and implies a protein conformational rearrangement to allow the ligand exit (opening of loops 310-320 and 165-170). The second path (path B), which occurs with a frequency of 30%, is in agreement with what already observed in the X-ray

structures and, in this case, the ligand exits via the preformed tunnel, already described (Umland et al., 2004; Wątor et al., 2020). Our MetaD calculations reveal the preference for path A, despite the conformational rearrangement, but it cannot be excluded that in unbiased simulations binding of ligand may occur preferentially through path B.

In conclusion, these data provide a detailed knowledge of the DHS-GC7 interaction, and all our findings, the characterization of the GC7 binding site, the comparison of the two sites (human vs archaea), as well as the discovery of an alternative unbinding path in the human enzyme, offer a fundamental contribution to the design of new specific and more efficient DHS inhibitors.

To further improve our knowledge, we focused on the characterization of the complex formed between the two proteins (IF5A-DHS), endeavouring to solve its three-dimensional structure.

In order to reach this challenging goal, we have successfully overexpressed aIF5A and DHS in *E. coli* system. Before starting with crystallization trials, we have confirmed the complex formation *in vitro* between recombinant aIF5A and DHS using size-exclusion chromatography and native-PAGE and we have set up two different protocols in order to obtain large amount of purified aIF5A-DHS complex. As clearly shown by these biochemical analyses (Fig. 12), aIF5A and DHS form a stable complex *in vitro* as it happens with eukaryotic systems (Lee et al., 1999). Information regarding chemical and biochemical features of IF5A-DHS complex are limited in literature; Park et al (Lee et al., 1999) proposed that the stoichiometry of the two components in the complex was estimated to be 1 DHS tetramer to 1 eIF5A molecule with a Kd of approximately 0.5 nM, highlighting a very high affinity. This finding seems to be somewhat in contrast with all the DHS structures solved so far (Liao et al.,

1998; Umland et al., 2004; Wątor et al., 2020), which have shown that the enzyme presents 4 distinct active sites. So, in order to verify these findings, we have used recombinant aIF5A and aDHS to perform ITC analysis and calculate the stoichiometry and all the thermodynamic parameters useful to better understand the interaction. Our results show that the stoichiometry of the complex, at a temperature of 30°C, was estimated to be two molecules of aIF5A for one DHS tetramer, with a Kd of 3.155 μM. Moreover, thermodynamic parameters have suggested that the interaction interface between these two proteins should be limited and driven mainly by hydrogen bonds and other non-covalent bonds.

The sample from the ITC experiment was recovered and used for crystallization attempts and we were able to obtain well diffracting crystals which allowed us to solve, for the first time, the three-dimensional organization of aIF5A-DHS complex.

The DHS in our structure is present as a tetramer formed by two tightly associated homodimers, in agreement with the corresponding human enzyme (Liao et al., 1998; Umland et al., 2004; Wątor et al., 2020), (Fig. 17), but in contrast with what was previously proposed (Lee et al., 1999) and with our ITC results, we could observe, in our structure, four aIF5A molecules are bound to one DHS tetramer at the same time (Fig. 16).

The interaction involves exclusively the N-terminal domain of aIF5A which is clearly visible, while the C-terminal domain is most likely endowed with a significant degree of flexibility which prevents its visualization in the electron density of the structure. As anticipated by ITC analysis, the interaction interface is limited and it includes 14 residues on aIF5A and 16 on DHS some of which are involved in hydrogen bonds (Fig. 24).

The specific lysine that undergoes hypusination (Lys36 in *S. solfataricus*) enters within the funnel of the DHS active site with a mode resembling a key with a lock.

Most of the residues inside the DHS active site are conserved if compared with the human ones. One of these is the lysine involved in the hypusination reaction (Lys288 in archaeal DHS and Lys329 in human DHS) reflecting the conservation of the enzymatic mechanism. The ball-and-chain motif described in the human enzyme (Liao et al., 1998) and proposed to block the active sites of DHS, is present also in this structure but it occupies a position that does not interfere with aIF5A binding.

Noteworthy, the N-terminal domains of the human and the archaeal proteins, (Fig. 21), are perfectly superimposable underlying the structural conservation and, consequently, the functional relevance of this domain (Fig. 22). It should be emphasized that, in the superposition, the only region which is not perfectly overlapping, regardless of its sequence identity, is the hypusination loop. The reason of this difference lies in the fact that the human structure derives from the isolated protein while the archaeal one is from the complex with the enzyme suggesting that, upon binding to the enzyme, the hypusination loop shifts to a new position to establish the correct network of interactions.

In this work the three-dimensional organization of the IF5A-DHS complex is presented for the first time. The complex, although from archaeal proteins, shows a high degree of structural conservation in the comparison with the two isolated human proteins (RMSD 0.912 Å for 232 Cα with human DHS PDB:6XXH; RMSD 0.765 Å calculated overlapping N-terminal domain of our aIF5A and the human one PDB: 3CPF) (Bassani et al., 2018, 2019).

This strong structural similarity allows us to consider this complex as a model to drive the design and developing of new deoxyhypusination inhibitors targeting, not only the DHS active site, but also the aIF5A-DHS complex formation.

SECOND PROJECT

SARS-CoV-2 graphene biosensor based on engineered dimeric ACE2 receptor

6 INTRODUCTION

6.1 Coronaviruses

Coronaviruses are a class of viruses infecting various animals causing minor to dangerous respiratory infections in humans. In 2002 and 2012, respectively, severe acute respiratory syndrome coronavirus (SARS-CoV) and Middle East respiratory syndrome coronavirus (MERS-CoV) emerged in humans and caused serious respiratory illness, making emerging coronaviruses a new public health concern in the twenty-first century (Cui et al., 2019). In December 2019, in the city of Wuhan, China, a novel coronavirus designated as SARS-CoV-2 emerged and caused an outbreak of unusual viral pneumonia called coronavirus disease 2019 (COVID-19) which has become a health emergency of global concern and still is in current diffusion all around the world (Hu et al., 2021).

6.2 SARS-CoV-2

The SARS-CoV-2 virus is a positive-strand RNA Betacoronavirus that shares 79% genome sequence identity with SARS-CoV and 50% with MERS-CoV (Lu et al., 2020). The genome is organized in six functional open reading frames (ORFs): replicase (ORF1a/ORF1b), spike (S), envelope (E), membrane (M) and nucleocapsid (N). In addition, there are other seven recognized ORFs encoding for accessory proteins that are interspersed between the six structural genes (Chan et al., 2020a). Most of the SARS-CoV-2 proteins have a similar length compared to proteins in SARS-CoV. Interestingly, if we consider the four structural genes, SARS-CoV-2 shares more than 90% amino acid identity with SARS-CoV except for the S gene, encoding for Spike, which presents several differences (Zhou et al., 2020).

The SARS-CoV-2 virion consists of four structural proteins, namely spike (S), envelope (E), membrane (M) and nucleocapsid (N). The positive-strand RNA genome (+ssRNA) is located inside the capsid formed by N, whereas M and E

ensure its incorporation in the viral particle during the final assembly process. Spike is a trimeric protein composed of three identical monomers that protrude from the viral envelope that recognize and bind the angiotensin converting enzyme 2 (ACE2) during the virus entry phase. To promote viral uptake and fusion with the cellular membrane, Spike also needs another host factor, the cell surface serine protease TMPRSS2 (V'kovski et al., 2021). Whitin the cytoplasm, genomic RNA is released and immediately subject to the translation of two open reading frames called ORF1a and ORF1b. The two resulting polyproteins, pp1a and pp1ab are subsequently processed to form the viral replication and transcription complex. After the replication of viral genomic RNA and its translation of all structural and accessory proteins the virus assembles to form a new virion ready to be secreted from the infected cell by exocytosis (Fig. 25).

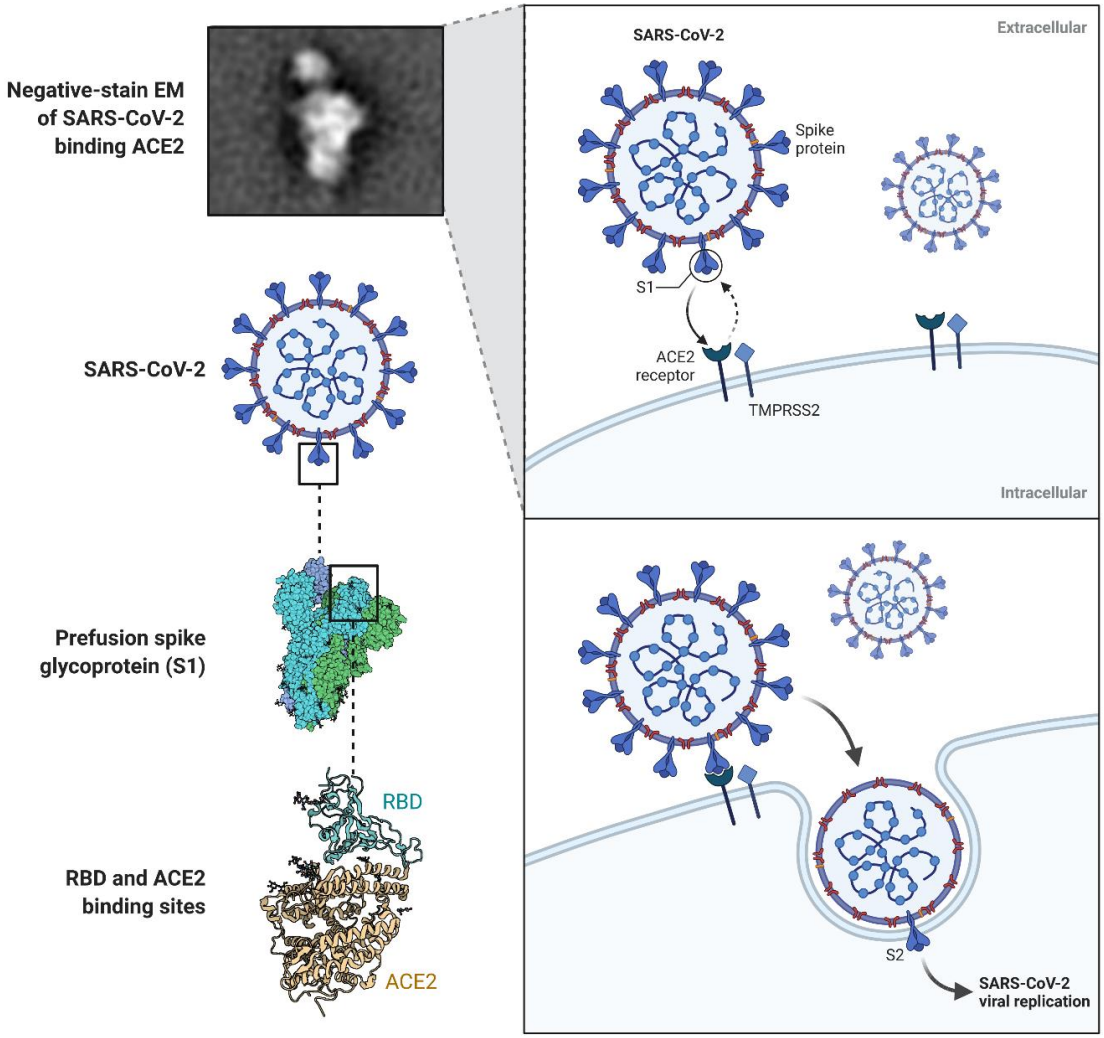

Figure 25 SARS-CoV-2 entry through host ACE2 receptor.

SARS-CoV-2 particles infect human respiratory epithelial cells through the specific interaction between Spike and human ACE2 together with another host factor, TMPRSS2, promoting viral uptake and fusion at the cellular or endosomal membrane.

6.3 COVID-19

Based on certain characteristics, such as age and state of health, the pathogenesis of COVID-19 in humans shows itself as mild symptoms to severe respiratory failure. SARS-CoV-2 binds epithelial cells in the respiratory tract, and it starts replicating and moving down to the airways to finally, enter into the lung epithelial cells where the rapid replication of the virus may trigger a very strong immune response. Stimulated immune cells respond with abnormal production of cytokines causing Cytokine storm syndrome and subsequently acute respiratory distress syndrome and respiratory failure, which is considered the main cause of death in COVID-19 patients (Huang et al., 2020a; Mehta et al., 2020).

6.4 Structural features of Spike protein

As described above, Spike protein is responsible for viral uptake and fusion at the cellular membrane. Spike is an homotrimeric class I fusion glycoproteins that are separated into two different domains, named S1 and S2 (Wrapp et al., 2020). The S1 subunit is composed by an N-terminal domain and a C-terminal domain, the latter one containing the Receptor Binding Domain (RBD) which has a vital role in virus entry and it is the main target of antibodies (Shang et al., 2020b; Walls et al., 2020). RBD contains the receptor-binding motif (RBM) which directly interacts with human ACE2 receptor. In particular, a four-residues motif (G-V-E-G) is involved in the interaction with the N-terminal helix of ACE2 (Walls et al., 2020). Interestingly, this and other structural features of the SARS- CoV-2 RBD have strengthened the binding affinity with the human receptor compared with that of SARS- CoV (Letko et al., 2020; Walls et al., 2020; Wan et al., 2020). Different three-dimensional structure of SARS-CoV-2 spike revealed that RBD has a lying-down conformation with one RBD present in open-conformation (Lan et al., 2020; Walls et al., 2020;

Wrapp et al., 2020) and this may be helpful for the virus to evade the host immune system (Shang et al., 2020a). On the other hand, the S2 subunit that is responsible for viral fusion and entry, comprises FP, HR1, HR2, TM domain, and cytoplasmic domain fusion (CT) (Huang et al., 2020a; Yang et al., 2020) (Fig. 26).

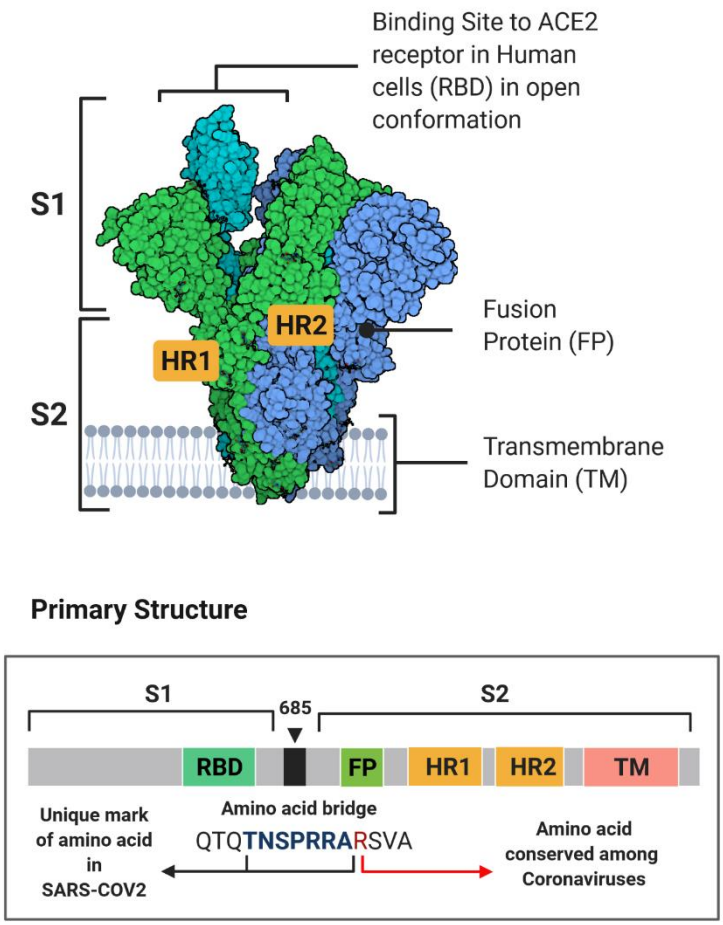

Figure 26 SARS-CoV-2 Spike protein structure.

(**upper**) Cryo-EM structure of Trimeric Spike protein in the open conformation (7FCD). The different domains of the protein are labelled; (**lower**) Schematic diagram of the Spike protein of SARS- CoV-2.

6.5 SARS-CoV-2 variants

SARS-CoV-2, as well as other viruses, tends to accumulate mutations which contribute to virus adaption and improve host-to-host infection (Harvey et al., 2021). The most dangerous SARS-CoV-2 variants have been classified as Variants of Concern (VOC) by the World Health Organization (WHO). At the time of writing this thesis, WHO have been identified five different SARS-CoV-2 VOCs since the beginning of the pandemic (March 2020): Alpha (B.1.1.7); Beta (B.1.351); Gamma (P.1); Delta (B.1.617.2); and Omicron (B.1.1.529) (https://www.who.int/en/activities/tracking-SARS-CoV-2-variants). Each of these variants contains several mutations, most of them are present on the Spike protein and result in an increase of affinity for ACE2, thus enhancing the magnitude of infection; others, instead, allow the virus to escape from the host immune response. A summary of VOCs and their changes is present in figure 27. Briefly, Alpha variant, reported for the first time in December 2020 (Aleem et al., 2022), contains 17 mutations in the genome. Of which, eight changes (Δ69-70 deletion, Δ144 deletion, N501Y, A570D, P681H, T716I, S982A, D1118H) are in the spike protein. Interestingly, N501Y also shared by other VOCs, is directly responsible for enhancing the interaction with ACE2. Beta variant, reported in January 2021 (Tegally et al., 2020), contains nine mutations (L18F, D80A, D215G, R246I, K417N, E484K, N501Y, D614G, and A701V) in the spike, of these, three mutations (K417N, E484K, and N501Y) are situated in the RBD. Gamma variant, reported in parallel with Beta during January 2021 (Aleem et al., 2022), includes ten different mutations in the spike (L18F, T20N, P26S, D138Y, R190S, H655Y, T1027I V1176, K417T, E484K, and N501Y). Three of these (L18F, K417N, E484K) are in the RBD. Delta variant was identified for the first time in December 2020 but classified as VOC in May 2021. Delta contains ten

mutations in the spike protein (T19R, (G142D*), 156del, 157del, R158G, L452R, T478K, D614G, P681R, D950N). Recently (November 2021), a new variant classified as Omicron, has rapidly surged past other variants to become the dominant SARS-CoV-2 strain with more than 30 mutations in the spike protein (N211del/L212I, Y145del, Y144del, Y143del, G142D, T95I, V70del, H69del, A67V, Y505H, N501Y, Q498R, G496S, Q493R, E484A, T478K, S477N, G446S, N440K, K417N, S375F, S373P, S371L, G339D, D796Y, 981F, N969K, Q954H), giving it the ability to effectively evade immune response and spread all around the world (Cameroni et al., 2022). All the Spike changes on different SARS-CoV-2 variants are summarized in figure 27.

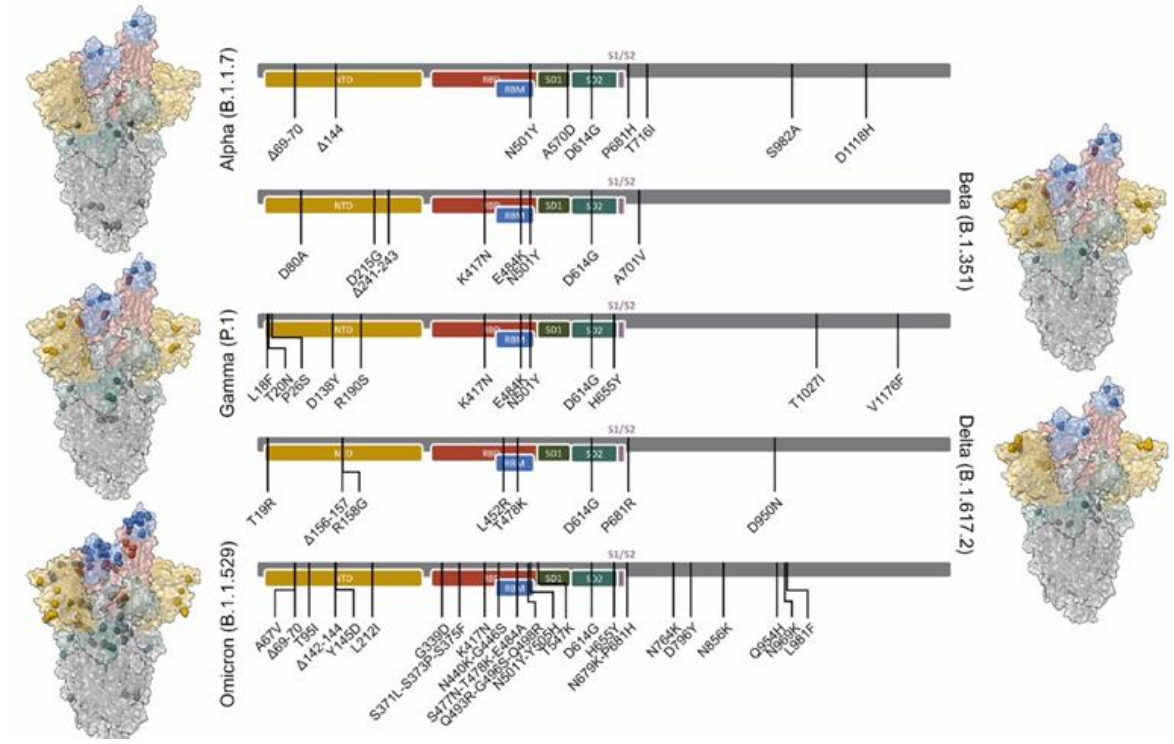

Figure 27 Schematic overview of SARS-CoV-2 variants.

Detailed amino acid mutations of SARS-CoV-2 Spike proteins in Alpha, Beta, Gamma, Delta and Omicron variants. Positions of mutations are shown both on a schematic domain representation of the protein and on the 3D model (PDB: 7DWZ).

6.6 Structural features of human ACE2

Despite the many different variants of spike, however all of them recognize ACE2 as host receptor. ACE2 is a is a type I membrane protein of 805 amino acids, expressed in lungs, heart, kidneys and intestine (Donoghue et al., 2000). In addition to being the SARS-CoV-2 receptor entry, the physiological role of ACE2 is in the maturation of angiotensin, a hormone that regulates vasoconstriction and blood pressure (Mehta and Griendling, 2007). From a structural point of view, ACE2 is reported as a dimer composed by two identical monomers that include two subunits, the Peptidase Domain (residues 19-615) and the Collectrin-Like Domain (CLD) (residues 616-768) that comprises a small extracellular domain, a long linker, and the single transmembrane helix (TM) which anchors the receptor to the cellular membrane (Fig. 28) (Yan et al., 2020). PD of a single monomer is recognized and bound by one RBD suggesting that dimeric ACE2 can accommodate two Spike protein trimers. Interestingly, biochemical experiments demonstrated that ACE2 in the dimeric form is two orders of magnitude more potent than the monomeric subunit in binding the Spike protein (Chan et al., 2020c).

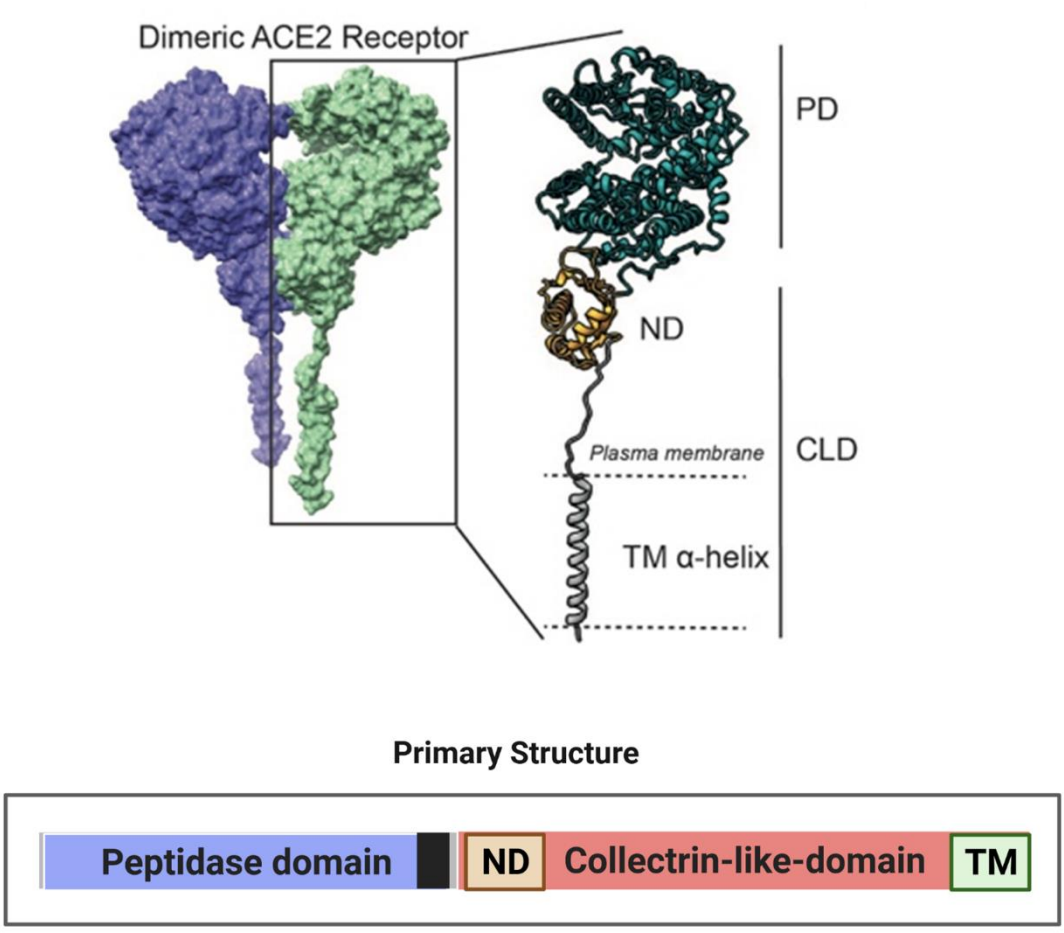

Figure 28 Cryo-EM structure of dimeric ACE2 receptor

The two subunits of a monomer are reported: Peptidase domain (PD) and Collectrin-like domain (CLD) that is composed by neck domain (ND) and transmembrane helix (TM). A schematic diagram of ACE2 structure is also reported.

6.7 COVID-19 diagnostic

To continue monitoring the spread of SARS-CoV-2, several diagnostic tests are currently available. Generally, they are classified in molecular and rapid tests. Gold-standard validation of SARS-CoV-2 infections is based on the detection of viral sequences through nucleic acid amplification, such as real-time reverse-transcription polymerase chain reaction (rRT-PCR). The assays' targets are small regions on the E, RdRP, N and S genes (Bordi et al., 2020; Chan et al., 2020b; Corman et al., 2020; Zhou et al., 2020). The limit is that it is sophisticated and requires specialized personnel in addition to the long detection time (several hours to days depending on the technology (Bordi et al., 2020). In addition, false negatives can be common when oral swabs are used. To support rRT-PCR test during the pandemic when the spread of the virus is very fast, several rapid diagnostic tests have been developed and introduced. These tests detect SARS-CoV-2 viral proteins (antigens), typically Spike's epitope, in respiratory tract specimens. Most of them are lateral flow immunoassays where an antibody recognizes a specific antigen. Even if the last ones are rapid (minutes for results), they may yield many false negatives due to the low intrinsic sensitivity (Udugama et al., 2020). In addition, the increasingly frequent onset of new variations of the spike protein, i.e., Omicron that harbours more than 30 different spike changes, leads to a failure of these tests to specifically recognize SARS-CoV-2 (Tubiana et al., 2022).

For all these reasons, it is important to find alternative methodologies capable to recognize rapidly and specifically SARS-CoV-2 and more importantly to obtain a better outbreak surveillance due to variants. Regarding this, further efforts are being made by the scientific community to propose new methods of diagnosis and screening (Huang et al., 2020c; Tian et al., 2020; Roda et al., 2021). Among these, biosensors systems and transduction technique have been

reported as very promising (Thévenot et al., 2001). In particular, field effect transistor biosenors (FET), represent a rapidly expanding field due to their high sensitivity and rapid detection (Forsyth et al., 2017; Vu and Chen, 2019).

6.8 Graphene field-effect transistor

FET biosensor transduces the interaction with biological molecules such as proteins, nucleic acids, etc., as a change in the electrical conductance of the sensor (Béraud et al., 2021). Classics FET are generally devices with three terminals, or electrodes: a semiconductor channel runs between two of these electrodes – the source and the drain – while a third, called the gate, acts as the control (Fig. 29). As semiconductor channels have been commonly used silicon nanowires, carbon nanotubes and graphene (Mu et al., 2015). Among these, graphene represents the most promising material for sensing applications, it exhibits exceptional sensitivity, high charge carrier mobility, as well as extremely high surface-to-bulk ratio environment (Brown et al., 2016; Huang et al., 2020b). Thanks to these advantages, graphene-FET sensors (gFET) are attractive in point-of-care (POC) diagnosis due to their miniaturization, potential for large-scale manufacture and no need for specialized personnel. The detection principle of gFET is based on a change in electrical performance induced by alterations in the bioelectronic interface of the sensor (Béraud et al., 2021). This principle is used to detect specific antigens, present into a solution, at the surface of the sensor. Talking more practically, in a gFET the potential is applied between source and drain electrodes generating the current (intended as flow of charge carriers) running on the graphene channel; while the third electrode, the gate acts as a control of the electric field, playing a role, also, on the current flow (Béraud et al., 2021). To achieve specificity in gFET device, the graphene surface is functionalized with molecules, called bioreceptors, able to specifically recognize and bind the target analyte into a solution. When a

bioreceptor, attached on graphene, detects a specific target molecule, there will be a perturbation of the current which will represent the electrical signal. This signal is described by the transfer curves which are obtained by sweeping the gate voltage Vg while maintaining a fixed bias Vds between the source and drain electrodes. The resulting current Ids is graphed, as a V-shaped curve, in function of the gate voltage. After a binding event on the graphene surface, the curve can shift to the right (indicating negative charge carriers (n-dope)) or to the left (represents an increasing density of positive charge carriers (p-dope)) (Béraud et al., 2021) based on different features such as pH of the ionic solution, intrinsic charge of the molecules, bioreceptors orientation, etc. The transfer curve minimum is referred to as the Dirac point, which may represent, during gFET analysis, an indication of the Ids curve position. A representative Ids transfer curve is shown in figure 29. To summarize the device principle, gFET functionalized with a bioreceptor transduces the biological signal into an electrical signal at the bioelectronics interface upon each binding event. During the COVID-19 pandemic, researchers all around the world have provided many solutions to detect the virus rapidly and specifically, based on different detection methods (Mollarasouli et al., 2022), some of them are based on graphene field-effect transistor technology; they are able to specifically detect SARS-CoV-2 through the recognition of both viral genome and structural proteins (Seo et al., 2020; Kang et al., 2021; Li et al., 2021). One of the first to be develop was published in early 2020 by Seo G. et al (Seo et al., 2020). They have proposed a COVID-19 gFET sensor in which the SARS-CoV-2 spike antibody is used as bioreceptor. Their results are very promising, being able to detect very low spike concentrations (with a limit of detection (LOD) of 1 fg/mL), highlighting the extremely sensitivity of a gFET device. However, the new SARS-CoV-2 variants, especially Omicron that harbours a set of more

than 30 spike mutations, could be able to escape SARS-CoV-2 spike antibody failing in detection of the virus. In order to slow down the COVID-19 pandemic and the insurgence of new highly infectious variants, there is a need to find variant-robust SARS-CoV-2 detection systems.

Considering this, we thought of exploiting the specific interaction between Spike and human ACE2 receptor to develop a gFET biosensor, an interaction that will never be affected by any current and future mutational changes on SARS-CoV-2 Spike protein. To reach this challenging goal, we have integrated molecular simulations, nanobiotechnology and electronic engineering in a multidisciplinary effort, to develop a point-of-care (POC) device that utilizes the human ACE2 as bioreceptor and sensing area of a gFET, aiming to mimic the viral mechanism of host cell access. Considering that most of the antigenic tests use antibody as sensing area, we have also tested an anti-Spike antibody (Ab) as bioreceptor of gFET to compare the sensing performance with ACE2 receptor.

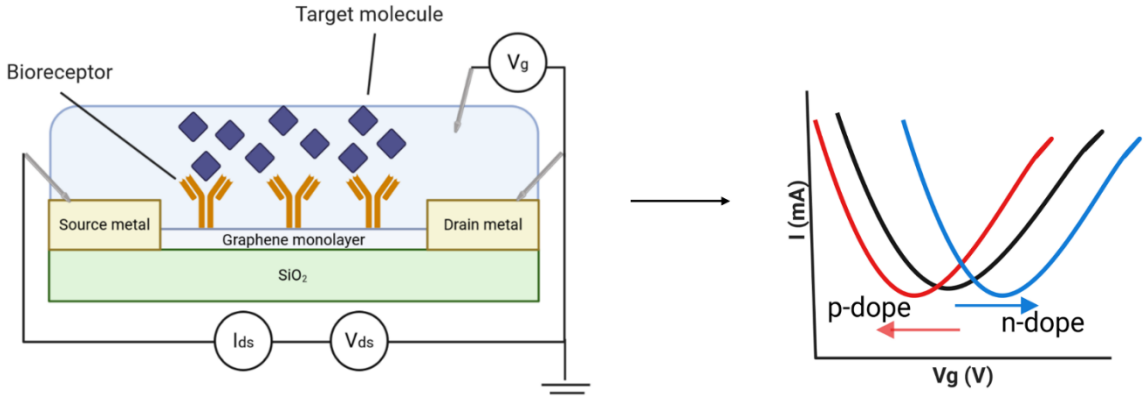

Figure 29 Schematic representation of a gFET, all the components are labelled. (**Right**) Output Ids/Vg curves before (black) and after the interaction between bioreceptor and target molecule (in red or blue depending on the charge carrier mobility).

7 MATHERIALS AND METHODS

7.1 Steered Molecular Dynamics simulations

Structures used for Steered Molecular Dynamics simulations (SMD) were first equilibrated with a multistage equilibration protocol adapted from (Motta et al., 2018).

ACE2 PD domain bound to SARS-CoV-2 Spike RBD (PDBID: 6VW1) and the three Ab-RBD binding modes (PDBID: 7BEK, 7MF1 and 6YLA) were prepared using the input generator of CHARMM-GUI (Sunhwan Jo, Taehoon Kim, Vidyashankara G. Iyer, 2012). charmm36m forcefield was utilized in all the simulations (Huang et al., 2017). The systems were then pre-aligned maintaining the direction of unbinding parallel to the x axis. Systems were then immersed in a water box with the size of 18 nm x 13.0 nm x 13.0 nm for the ACE2-RBD system, 20 nm x 12.0 nm x 12.0 nm for the 7BEK and 7MF1 systems and 18 nm x 11 nm x 11 nm for 6YLA system. The size of the box was set to accommodate the system and increasing the x dimension of about 4 nm to allow the RBD unbinding. Moreover, systems were neutralized with K+ or Cl- counterions agreeing to their total charges. GROMACS 2018.3 was used to run the simulations (Abraham et al., 2015). A multistage equilibration protocol, adapted from (Motta et al., 2018), was applied to remove unfavourable contacts and offer a consistent starting point for the SMD analyses. Firstly, the systems were subjected to 1000 step of steepest descent energy minimization with positional restraints (2000 kJ mol-1 nM-2) on all resolved atoms. Successively, a 1.0 ns NVT MD simulation was used to heat the system from 0 to 100 K with limits lowered to 400 kJ mol-1 nM-2 and then the systems were heated up to 300 K in 2.0 ns during an NPT simulation with further lowered restraint (200 kJ mol-1 nM-2). Lastly, the systems were equilibrated during an NPT simulation for 10 ns with backbone restraints reduced to 50 kJ mol-1 nM-2. SMD production runs were conducted in NPT using the V-rescale thermostat

(Bussi et al., 2007) (coupling constant of 0.1 ps) while pressure was set to 1 bar with the Parrinello-Rahman barostat (Parrinello and Rahman, 1981) (coupling constant of 2 ps). A time step of 2.0 fs was used, together with the LINCS (Hess, 2008) algorithm to restrict all the bonds. The particle mesh Ewald method (Essmann et al., 1995) was used to treat the long-range electrostatic interactions with the cut-off gap set at 12 Å. Short-range repulsive and attractive dispersion interactions were concurrently described by a Lennard-Jones potential, with a cut off at 12 Å, applying long-range dispersion corrections for energy and pressure.

With structures properly equilibrated, SMD simulations were performed by harmonically restraining the x component of the distance between the centre of mass of the backbone of the two proteins. A force constant of 10 kJ mol-1 nM-2 was used and the equilibrium value of the distance was changed at a constant velocity (two different simulations were performed for each system at 0.05 Å ns-1 and 0.02 Å ns-1). The force applied to the harmonic spring was monitored during each simulation.

7.2 Simulation of dimeric ACE2 systems

To evaluate the dynamic properties of ACE2 embedded in membrane (ACE2-Membrane), ACE2 in solution (ACE2), and ACE2 bound to Fc (ACE2-Fc) we built the three systems starting from the 6M17 structure, after the exclusion of other proteins co-crystallized with ACE2. For the ACE2-Membrane system we embedded ACE2 in a POPC:CHOL (90:10) membrane using CHARMM-GUI. For the soluble ACE2 we deleted the transmembrane helices (residues 741-768) and included a 6x-His tag at the C-terminal of each chain. For ACE2-Fc we linked the extracellular portion of ACE2 (residues 21-740) to the structure of Fc. To do this, we performed a BLAST search on PDB with the sequence of

the Fc tag provided by the manufacturer (Proteintech, UK) and used the best resulting structure (PDB: 1IGT). The resultant Fc domain was separated from the whole structure and then attached to ACE2 using Chimera (Pettersen et al., 2004). The chimeric structure was then minimized via Steepest Descent as previously described (D'Agostino et al., 2020). Solution systems (ACE2 and ACE2-Fc) were equilibrated utilizing the multistage protocol used before and explained for the SMD simulations. Differently from the previous protocol, ACE2-Fc linker were not subjected to positional restraints during the equilibration stage. A distinct lower equilibration protocol was used for the ACE2-Membrane system due to the presence of the membrane. In detail, the system was first subjected to 1000 step of steepest descent energy minimization with positional restraints. Subsequently a 1.0 ns NVT MD simulation was used to heat the system from 0 to 100 K and then the system was heated up to 300 K in 2.0 ns during an NPT simulation. Finally, four equilibration steps of 3 ns, 5 ns, 5 ns and 10 ns respectively were performed regularly lowering the restraints acting on the system. Restraints used in each step and the corresponding atoms on which they are applied are summarized in Table 1.

Correlation matrices were obtained using a modified version of g_covar, available at the GROMACS user contribution page, which computes the matrix of atomic correlation coefficients. The calculation was performed on Cα atoms of PD and CLD domains of ACE2 for all the three dimeric systems, sampling the frames every 100ps.

The first 30 ns of each simulation was discarded as a further equilibration stage, and the subsequent 500 ns were analyzed.

Step	Protein BB ($kJ\ mol^{-1}\ nM^{-2}$)	Protein SC ($kJ\ mol^{-1}\ nM^{-2}$)	Lipid Polar Head ($kJ\ mol^{-1}\ nM^{-2}$)	Lipid dihedral ($kJ\ mol^{-1}\ rad^{-2}$)
Mini	400	2000	1000	1000
Heat 1	4000	2000	1000	1000
Heat 2	2000	1000	1000	400
Equil 1	1000	500	400	200
Equil 2	500	200	200	200
Equil 3	200	50	40	100
Equil 4	50	0	0	0

Table 1. Protein BB are the protein backbone heavy atoms; Protein SC are the protein sidechain heavy atoms; Lipid polar head are the O3 cholesterol atom and the P POPC atom; Lipid dihedral is the torsional angle between C3-C1-C2-O21 and C28-C29-C210-C211 POPC atoms.

7.3 Purification of Trimeric Spike protein from FreeStyle HEK293-F cells

The plasmid for expression of the SARS-CoV-2 prefusion-stabilized Spike ectodomain in HEK293-F cells (Thermo Fisher) was a generous gift from the McLellan laboratory at the University of Texas at Austin (Hsieh et al., 2020)in). 350 μg and 1.05 mg PEI (Polysciences Inc.) were used to transfect cells at 1.2x106 cells/ml. After five days in suspension culture, the cell supernatant was collected and filtered using a 0.22 μm filter. Protein in the supernatant was bound to Nickel-NTA agarose (Qiagen) while under rotation in buffer composed of 2 mM Tris/HCl pH 8, 150 mM NaCl and 10 mM imidazole for two hours at 4°C. The resin was then washed in Tris-NaCl buffer, pH 8, with 20 mM imidazole and protein was eluted in 200 mM imidazole. Following overnight dialysis against PBS, the protein was filtered and stored as 0.2 mg/ml aliquots at -80°C.

7.4 Pull-down assay

The protein pull-down assay to validate the interaction between Spike and ACE2 or anti-Spike antibody Ab-CR3022 or ACE2-Fc was performed using a strep-tactin Sepharose resin as previously described (Cai et al., 2011), with some modifications. Briefly, 80 μl indicated strep-tactin resin were washed with phosphate-buffered saline (PBS) pH 7.4 (173 mM NaCl, 2.7 mM KCl, 10 mM Na2HPO4, 2mM KH2PO4) and incubated with 5 μg of recombinant trimeric Spike protein with a C-terminus strep-tag (Spike-strep) next to an his-tag at room temperature for 1 hour. After incubation, Spike-bound beads were washed three times with 500 μl PBST buffer (PBS and 0.05% Tween-20) and then were aliquoted into different tubes. 5 μg of ACE2 in PBS or 5 μg of anti-Spike or 5 μg of ACE2-Fc in PBS were mixed with spike-bound beads in three different 1.5 ml tubes and incubated at room temperature for 1 hour separately.

After a 1-hour incubation, beads were washed three times with 500 µl PBST buffer and the bound proteins were eluted using 50 µl of elution buffer (PBS added of 2.5 mM biotin (Sigma)). The samples were then subjected to SDS–PAGE and analysed by western blotting using an anti-histidine antibody (Thermo Scientific) to detect Spike and ACE2, an anti-rabbit antibody (Santa Cruz Biotechnology) to detect Ab-CR3022 and an anti-ACE2 antibody (EMP Millipore Corp) to detect ACE2-Fc by chemiluminescent revelation. The same protocol, using empty beads (without Spike), was performed as a negative control for each system.

7.5 gFET functionalization

ACE-Fc, ACE2 and anti-Spike antibody were covalently immobilized over the fabricated gFET chip (Graphenea gFET-S20) through PBASE. A droplet of 5 mM PBASE (Thermo Fisher Scientific, Waltham, MA) in dimethylformamide (DMF) was placed on the chip for 2h at room temperature before being rinsed several times with DMF, deionized water (DI) and dried with N2. Finally, the PBASE-functionalized devices were exposed to 250 µg/mL of ACE2-Fc (Z03484-1; GenScript Biotech), ACE2 (10108-H08B-100; Sino Biological, Inc., China) or anti-Spike (40150-R007; Sino Biological, Inc., China) separately and left overnight in a humidified environment at 4 °C. The sensor was then sequentially rinsed in PBS (pH 7.4, 1X), DI water and dried under N2 flow. The chip was subsequently treated with 100 mM glycine in PBS (pH 8.4, 1X) for 30 minutes for the termination of excess PBASE NHS groups at room temperature. After glycine treatment, samples were rinsed with PBS (pH 7.4, 1X), DI water and dried with N2.

7.6 gFET characterization using Raman and AFM

AFM measurements were performed with a SOLVER PRO from NT-MDT, RMS was evaluated by using Nova Px software. A Horiba Jobin-Yvon XploRA Raman microspectrometer, equipped with a 532-nm diode laser (~50mW laser power at the sample) was used. All measurements were acquired by using a ×100 long working distance objective (LMPLFLN, N.A. 0.8, Olympus). The spectrometer was calibrated to the 520.7 cm-1 line of silicon prior to spectral acquisition. A 2400 lines per mm grating was chosen. The spectra were dispersed onto a 16-bit dynamic range Peltier cooled CCD detector. The spectral range from 1100 to 3000 cm-1 was chosen and spectra were acquired for 3×10 seconds at each measurement spot. Chips were measured before and after PBASE functionalisation. For each sample, 10 point/spectra were acquired, and a Raman map was acquired with the same parameters on squared areas (20 μm × 20 μm), with a step size of ~3 μm, for a total number of 36 spectra. On each Raman map, the following values were calculated: intensity of the band centred at 2690 cm-1 (the 2D band), the intensity of the band at 1592 cm-1 (the G band), and the ratio between these two bands (I2D/IG). False colour images were built by using the I2D/IG ratio.

7.7 gFET electrical measurements

Sensing performances were evaluated by using a Wentworth probe station equipped with a Bausch & Lomb MicroZoom optical microscope and by using an HP4145B semiconductor parameter analyser. Current-voltage curves (Ids-Vds) have been acquired (i) by applying a Vds between –0.1 V to 0.1 V, (ii) by operating in liquid gating condition with PBS solution pH 7.4, and (iii) by using a Vg of 0 V. Transfer curves (Ids-Vg) have been obtained (i) by using Vds 0.050 V, (ii) by operating in liquid gating condition with PBS solution at pH 7.4, (iii) by applying Vg swept from 0 to 1.5 V, (iv) by carrying out a relaxation

step to obtain a constant equilibrium of ions on the surface of graphene. During this step, Vds and Vg were both applied on the gFET until no variations on the current-voltage curves were observed; in this way, the same ions screening effect was maintained during the measurements and the current-voltage curves, taken on the same gFET at different times, were completely superimposable. mPRO recombinant protein was kindly provided by Prof. Paolo Mariani from Polytechnic University of Marche (Silvestrini et al., 2021). Recombinant MERS-CoV Spike protein was purchased from Sino Biological (40069-V08B).

7.8 Non-reducing SDS-PAGE

The ACE2-Fc dimerization was assessed through SDS-PAGE and carried out under non-reducing and reducing conditions. Briefly, 2µg of ACE2-Fc or ACE2 samples were placed 10 minutes at 100 °C under denaturing conditions with Laemmli sample buffer reduced by β-mercaptoethanol or under non-reducing condition using a sample buffer without β-mercaptoethanol. 8% gel was used to correctly separate ACE2-Fc or ACE2 monomers from the dimers.

7.9 SARS-CoV-2 isolation and virus stocks

Different lineages of SARS-CoV-2 (Table 3) were isolated from RT-PCR positive nasopharyngeal swabs collected at Ospedali Riuniti, Ancona (Italy) using Vero E6 cells (ATCC n° CRL-1586), as described by Alessandrini et al. (Alessandrini et al., 2020). Vero E6 cells, seeded in 75 cm2 flasks, were subsequently infected with 2 mL of the virus from the isolation to a final volume of 12 mL to obtain a larger stock. Supernatants of the infected cells were harvested after 72 hours, centrifuged at 3000 rpm for 10 min, filtered using a 0.2 µm filter, aliquoted and stored at -80°C. Six virus stocks were sequenced and used for the present study: B.1.610 (EPI_ISL_417491), Alpha

(EPI_ISL_778869), Gamma (EPI_ISL_1118260), Beta (EPI_ISL_1118258), Delta (EPI_ISL_2975994) and Omicron (EPI_ISL_7897869).

7.10 RT-qPCR of patient samples

Clinical Samples used in this study (Table 4) were kindly provided by Dott. Simone Barocci and Prof. Stefano Menzo from U.O.C. of Clinical Pathology from the hospital of Urbino (Italy) "Santa Maria della Misericordia" and from Virology Unit from "Ospedali Riuniti", Ancona (Italy), respectively. Nasopharyngeal swabs from COVID-19 positive patients and COVID-19 negative were stored in PBS 1X and used. The positivity or negativity of these samples were determined by real-time RT-qPCR following manufacturer's specifications (ALLPLEX SARS-CoV-2 ASSAY and MDS methodologies).

7.11 RT-qPCR SARS-CoV-2 and Variants Detection

Viral RNA was extracted from nasopharyngeal swabs using the Kit QIAsymphony DSP Virus/Pathogen Midi kit on the QIAsymphony automated platform (QIAGEN, Hilden, Germany) according to manufacturer's instructions. Multiplex real-time RT-PCR assay was performed using qPCRBIO Probe 1-Step Go No-Rox (PCRBIOSYSTEMS, London, UK) on the Applied Biosystems 7500 Fast Dx Real-Time PCR Instrument (Thermo Fisher Scientific). The oligonucleotide primers and probes were designed to detect 69/70 deletion and N501Y mutation from virus Spike gene to discriminate alpha and gamma lineage respectively. Variant lineage was confirmed by sequence analysis of Spike gene using ABI Prism 3100 Genetic Analyzer (Applied Biosystems-HITACHI).

7.12 Designing the Case and Carrier units

The case of the Signal Acquisition Device was based on a 2D CAD drawing of the PCB board. In order to run virtual simulations of the assembly and check for interferences between all parts, a 3D model of the Board, Antennae and Battery was created and ultimately the case ended up being shaped around those objects. Following several iterations, the final design featured a simple rectangular shape, which allowed us to achieve very good results even with traditional 3D printing solutions such as FDM and basic materials like ABS.

The Signal Acquisition Device assembly is comprised by four main parts: an Upper Case, a Lower Case, a Window and a Button (Fig. 30 A, C). The Upper-Case features two holes in the front to host M3 screw heads, two male snap fits in the rear (in proximity of the Antennae) and a slot for fitting a transparent window. The Lower-Case acts as a rest bed for the main electric board and its battery. It features two Ø3,3 mm holes at the front (for M2 heat inserts) alongside two Ø4 mm holes (for M3 heat inserts). The M2 heat inserts, in combination with M2x5 screws, are used to keep the board in a fixed and stable position. The M3 heat inserts allow (with the use of M3x14 screws) to tightly close the Upper and Lower Case together. The lower case also presents female snap fits at the rear and holes on the sides made to access the USB Type C and the USB Micro B connector. The window allows the user to visually see LED lights (located on the board) while operating the device. It was obtained by pouring transparent epoxy resin into a 3D printed ABS mold. The button acts as an extension and allows to trigger the on/off switch located on the electrical board. In order to fully test the snap fit joints, a final prototype was 3D printed using the SLS (Selective Laser Sintering) printing technique (Fig. 30 C-D).

Alongside the main Case, the gFET Cartridge was designed (Fig. 30 B, D). This unit keeps the graphene chip and the spring-loaded contact pins together, while ensuring a stable and precise alignment between the two. It is arguably the most delicate parts of the biosensor, since any small misalignment between these two components would lead to inconsistent or unreliable measurements. The gFET Cartridge is comprised of three main parts: the Carrier 1, Carrier 2 and Carrier 3 (Fig. 30 B). The Carrier 1 houses the cartridge where the spring-loaded contact pins are encapsulated. The Carrier 2 has a slot that contains the 10.4x10.4 mm gFET chip. Early prototypes featured larger slots to take into account tolerances and the 3D printer's accuracy, however, after confirming that a high printing quality could be achieved with a traditional FDM printer, clearance was decreased by narrowing down the gFET housing slot. The result was a much higher measuring precision and reliability. The Carrier 2 also features hexagonal-shaped housings into which M3 nuts can be snapped into place. The Carrier 3 acts as a plate that holds the whole assembly together with the help of M3x12 screws. An opening allows a lab pipette to access and reach the gFET inside. Despite being part of the assembly design, final tests showed that the Carriers 1 and 2 had such a precise fit and low clearance that the device could be operated even without the Carrier 3 part installed.

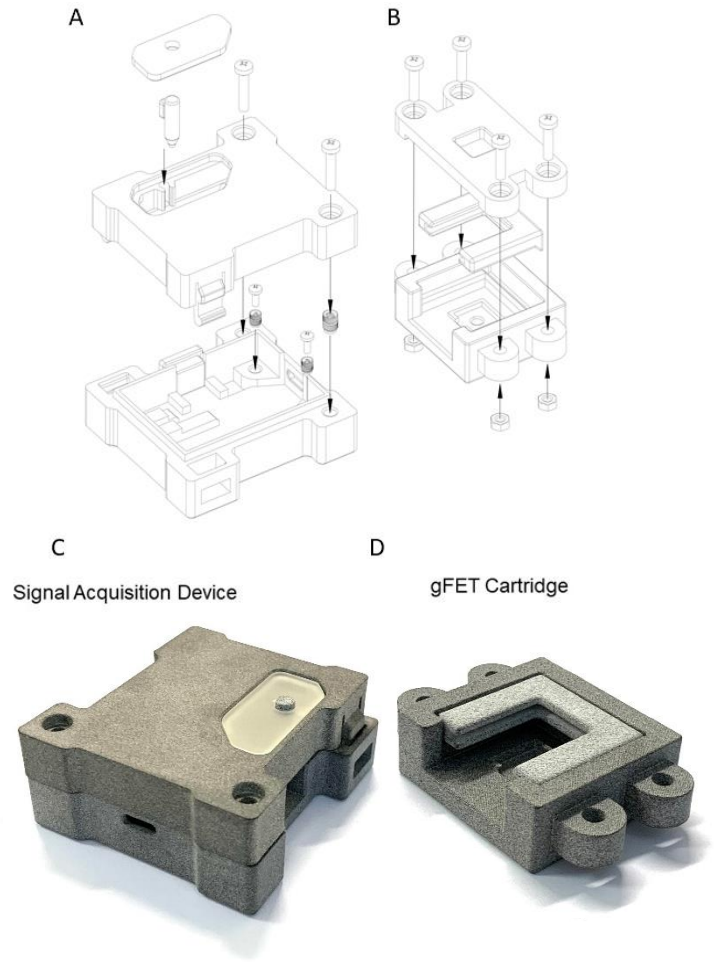

Figure 30 Point-of-Care (POC) prototype components

(**A**) Case assembly unit: Window, Button, Upper case and Lower case (from top to bottom); (**B**) Carrier assembly unit: Carrier 3, Carrier 1 and Carrier 2 (from top to bottom). Photographs of the device units: main case (**C**) and gFET carrier case (**D**). 3D printed using the SLS (Selective Laser Sintering) printing technique.

8 RESULTS

8.1 In depth characterization of the ACE2-RBD and Ab-RBD interaction is crucial for optimal design of the biosensor

Collecting information concerning the structural and dynamical features of the receptor-ligand interaction is mandatory to select the most appropriate bioreceptor to functionalize the device, in order to ensure the highest performance of the biosensor. To this aim, we have performed a series of Steered Molecular Dynamics (SMD) simulations to evaluate the strength of the interaction between the RBD and its host partner, the ACE2 receptor (Fig. 31 A) in comparison with an Ab-RBD complex (Fig. 31 B). Since Ab can bind RBD in different regions, we used for SMD three representative Ab structures (PDB: 7BEK, 7MF1 and 6YLA) obtained by structural comparison of over thirty different complexes (Fig. 31 C) summarized in table 2. Although they interact differently with RBD, the resulted force needed to separate the RBD from ACE2 or from the most stable Ab-RBD complex (group 3) is the same at both velocities tested (Fig. 31 D, E). The interaction of ACE2 and anti-Spike Ab with the trimeric spike protein, was further confirmed through pull-down assays and western blot detection (Fig. 31 F). The results in figure 31 F indeed confirm the expected interaction between spike and both bioreceptors as shown by the presence of both proteins bands in eluted lane of all western blot membranes. The mere presence of the ACE2 or Ab bands in the unbound fractions on each pull-down assay confirms that the excess of spike protein has been washed away and that the rest of this is well bound on the resin. The inputs of each tested proteins were also loaded on the gel and assessed with their specific primary antibody. Taken together, our computational and biochemical results suggest that ACE2 can be used as a bioreceptor for gFET functionalization.

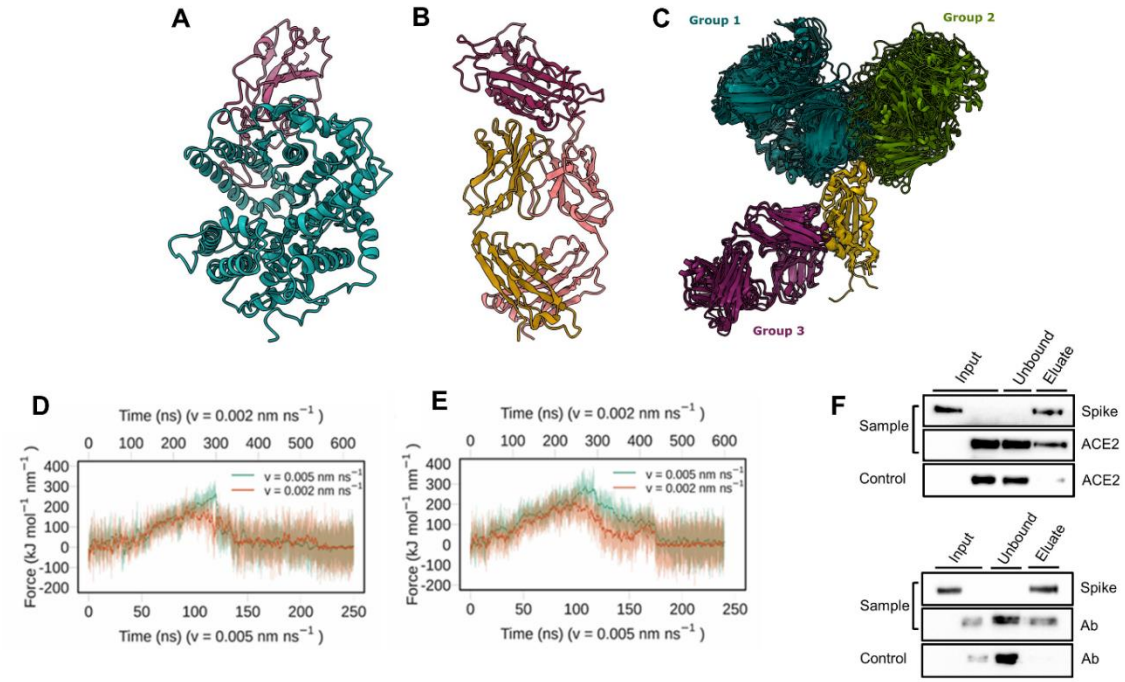

Figure 31 Interaction between Spike and its protein partners.

(**A**) Ribbon representation of the Peptidase Domain (PD) of the human ACE2 bound to the RBD of the SARS-CoV-2 Spike protein; (**B**) Ribbon representation of Antibody CR3022, bound to the SARS-CoV-2 Spike protein RBD; (**C**) Ribbon representation of three, available on PDB, groups of antibodies bound to RBD. Structures were superimposed on RBD (yellow cartoons). The first group includes twenty structures, the second group is composed by nine structures and the third 5 structures. (**D**) Force profiles from the SMD simulations of ACE2-RBD and Ab-RBD from group 3 (**E**); (**F**) Pull-down assay of Spike and ACE2 (upper), and Spike and Ab (lower). Control is represented by the same experiment excluding the Spike protein (bait) from the system. The binding of Spike with ACE2 or anti-Spike were monitored by Western blot analysis.

PDB ID	Resolution (Å)
7BEK	2.04
7MF1	2.09
7CJF	2.11
7BEH	2.30
7BEI	2.30
6XC4	2.34
7CHB	2.40
7BEJ	2.42
7KQB	2.42
6YLA	2.42
7BEN	2.50
7BEM	2.52
7BEL	2.53
6XKQ	2.55
7KN6	2.55
7K43	2.60
7BEP	2.61
7M71	2.66
7CHF	2.67
6XC3	2.70
7CH5	2.70
7CZT	2.70
7CHC	2.71
6XKP	2.72
7KN7	2.73
7ND9	2.80
7CZX	2.80
7CZW	2.80
7ZCQ	2.80
7BWJ	2.85
7C01	2.88
6XC7	2.88
7KQE	2.88
7M7B	2.95

Table 2. List of the PDB ID codes of AB-Spike structures.

Resolution and corresponding reference of all the Antibody-Spike complex structures used for the analysis of interaction patterns. The three Ab chosen for SMD are highlighted.

8.2 Characterization of the functionalized gFET

The gFET for electrical measurements was provided from Graphenea (San Sebastian, Spain) consisting of 12 separated single-layer graphene channels (90 x 90 μm^2) connected to a source and a drain electrode. It also includes a non-encapsulated electrode at the centre of the chip, which allows liquid gating through PBS solution (Fig. 32 A). To attach ACE2 or Ab to graphene we have used the bifunctional 1-pyrenebutanoic acid succinimidyl ester (PBASE) as a linker. PBASE is a heterobifunctional linker that contains a pyrene group that stacks with graphene by $\pi - \pi$ overlap and an N hydroxysuccinimide (NHS) ester that reacts with primary amines present in N-terminus or in Lysine sidechain of proteins (Li and Chen, 2018) (Fig. 32 A). To obtain an efficient coverage and avoid the formation of multiple layers of pyrene, we tried to treat the graphene with three different concentrations of PBASE in DMF solution (2.5 mM, 5 mM and 10 mM). Therefore, we characterized the bare and the different functionalized gFETs by Atomic Force Microscopy (AFM) (Fig. 32 B) in order to choose the best functionalization condition. AFM analyses have shown that 5 mM of PBASE represents the correct concentration to well-cover the graphene. The surface roughness, in terms of RMS value, increased from 0.392 nm to 0.863 nm for gFET and gFET-PBASE at 5 mM, respectively, confirming the presence of the pyrene-based linker on the top of the gate electrode surface. In the same way, Raman spectrum (Fig. 32 C) clearly show a decrease in 2D band intensity and the appearance of the D and D' bands in graphene-PBASE samples. Both D and D' bands are related to the disorder in the structure of sp2-hybridized carbon; hence, the appearance of these two bands after PBASE treatment is explained by the interaction of the vibrational modes of PBASE with the extended phonon modes of graphene. Moreover, Electrical characterization of pristine and activated gFET confirmed the

PBASE non-covalent bond to graphene (Fig. 32 D). The transfer curves (Ids-Vg) of gFET and gFET-PBASE (Fig. 32 D) were obtained (i) by fixing Vds 0.05 V, (ii) by operating in liquid gating condition with PBS solution at pH 7.4, and (iii) by applying Vg from 0.4 to 1.2 V. The curve obtained for the PBASE-functionalized gFET resulted positively shifted when compared to the one of the bare gFET; this trend is trivial and is due to the p-doping effect of the pyrene group attached to the graphene surface through π-π stacking (Thodkar et al., 2021).

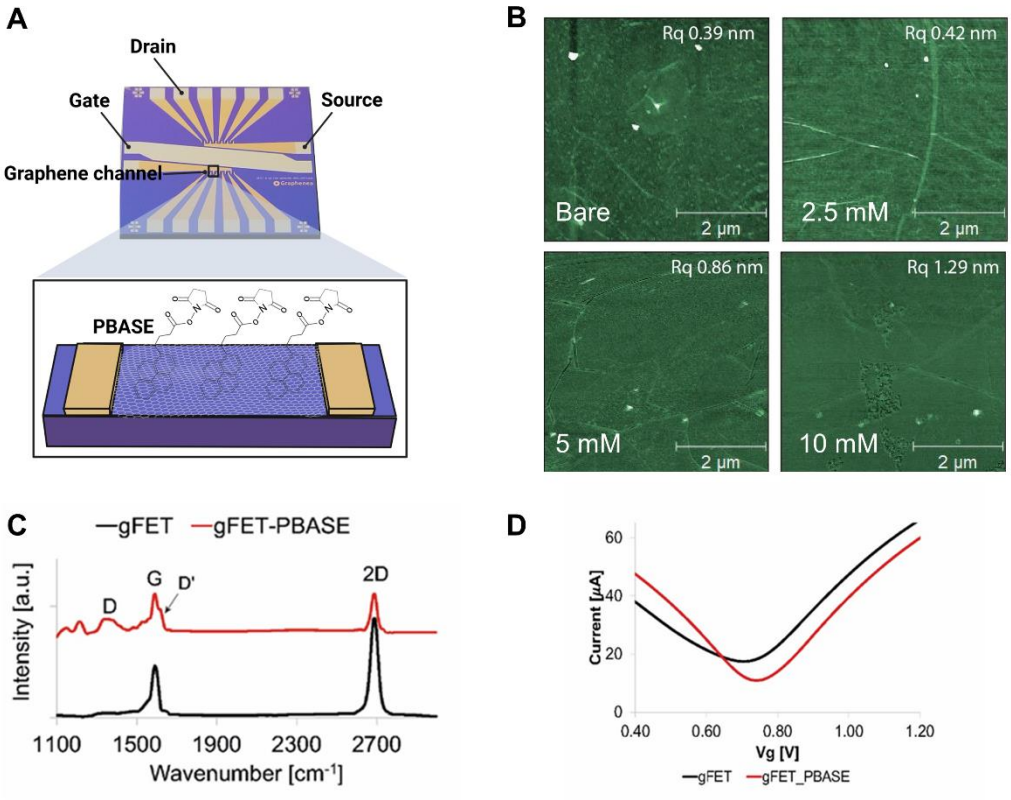

Figure 32 Characterization of functionalized-gFET.

(**A**) Picture of commercial gFET (size 10 mm x 10 mm) from Graphenea. It is composed by two source electrodes each one connected with six graphene channels and the respective drains. A single gate electrode is used for both sides of gFET. In the inset panel A is reported a schematic representation of the PBASE-modified gFET; (**B**). AFM images of untreated gFET and after treatment with 2.5 mM, 5 mM and 10 mM PBASE solution. Rq, root mean surface roughness and PBASE concentration are reported on each image; (**C**) Raman Spectra of gFET (black) and gFET-PBASE (red) (diode laser wavelength 523 nm and laser power 50 mW); (**D**) Transfer curves (Ids -Vg) of pristine gFET (black) and gFET_PBASE (red) obtained (i) by using Vds 0.050 V, (ii) by operating in liquid gating condition with PBS solution pH 7.4, and (iii) by applying Vg from 0.4 to 1.2 V.

8.3 SARS-CoV-2 Spike protein detection by ACE2_gFET and Ab _gFET

Following a first characterization of gFET-PBASE, we examined the sensing performances of the gFET functionalized with the soluble ACE2 (ACE2_gFET) (Fig. 33 A) and Ab (Ab_gFET) (Fig. 33 E) by using different concentrations of recombinant Spike protein. The working principle of gFET takes advantages of graphene band-structure in which valence and conduction bands ideally touch each other at the Dirac points. The latter can be tuned thanks to external influences: electron withdrawing groups adsorbed on the surface of graphene lead to a p-type doping effect, while electron rich molecules lead to a n-doping behaviour. The doping effect essentially produces a shift in the Dirac point to a more positive (p-doping) or more negative voltage (n-doping). The differences in terms of Dirac point, before and after the perturbation of graphene, can therefore be monitored and utilized as a means of sensing biological molecules (Matsumoto et al., 2014). Two different concentrations (2 µg/ml and 0.2 µg/ml) of Spike and the main protease (mPRO, used as negative control) from SARS-CoV-2 were tested to evaluate the sensor response and specificity. All the measurements were conducted by using a liquid gating with a PBS solution at pH 7.4, a fixed Vds of 0.05 V and a Vg swept ranging between 0.4 and 1.2 V. After the addition of either Spike protein or mPRO to the functionalized gate electrode, the system was incubated at room temperature for 30 minutes to ensure the binding with the antibody or ACE2. Then, a final washing step with PBS solution was done to remove the unbound material before recording the Ids-Vg curves. After addition of the Spike protein (2 µg/mL) to the gFET, a negative shift of the whole curve is observed for both ACE2_gFET (Fig. 33 B) and Ab_gFET (Fig. 33 F).

The gFET sensing performances were also evaluated by using an order of magnitude diluted Spike protein (0.2 µg/mL). In the case of Ab_gFET the

negative shift is still observed (Fig. 33 H) but at a lower extent than what registered with the previous concentration. Conversely, no differences were detected when testing a 0.2 µg/ml concentration of Spike protein on ACE2_gFET (Fig. 33 D). The curves obtained by testing mPRO (2 µg/ml and 0.2 µg/ml concentrations) are completely superimposable to the ones of the bioreceptors alone (Fig. 33 C, G), denoting the absence of the interaction. Figure 33 also shows bar charts representing the normalized Dirac point (Vd) before and after each antigen addition (Fig. 33 D, H).

The gFET_Ab transfer curve were also recorded after the addition of Spike protein at 0.02 µg/mL (Data not shown); in this case, no significant shift was observed (Fig. 33 H). The curves obtained by testing mPRO (0.02 µg/ml) are completely superimposable (Data not shown).

According to these results, ACE2 has shown limitations in sensitivity while antibody can detect lower spike concentration. However, SARS-CoV-2 variants could elude monoclonal antibodies recognition. Therefore, the use of ACE2 represents a more promising candidate to next-generation SARS-CoV-2 device. Since dimeric ACE2 is two orders of magnitude more potent than the monomeric subunit (Chan et al., 2020c), we have decided to still consider ACE2 as a good candidate as bioreceptor for our biosensor.

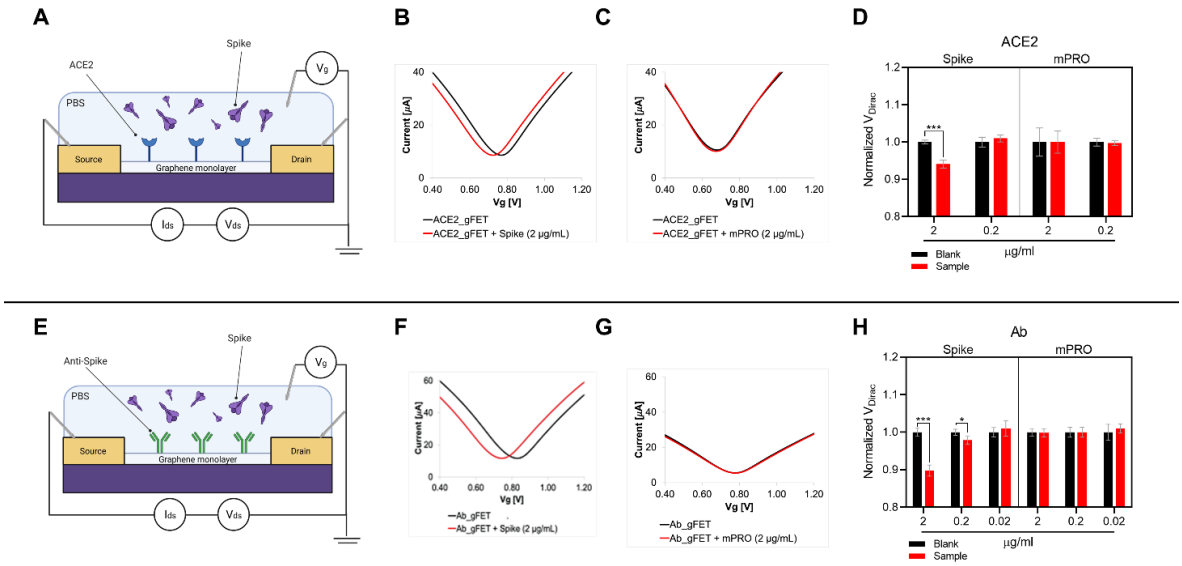

Figure 33 gFET setup and Spike recognition.

(**A**) Schematic representation of ACE2_gFET (**B-C**) Ids-Vg curves obtained as the mean of six different measurements on the same device of (**B**) ACE2_gFET (black) and ACE2_gFET-Spike (red), Spike protein was 2 µg/mL; (**C**) ACE2_gFET (black) and ACE2_gFET-mPRO (red); mPRO protein was 2 µg/mL; (**D**) Comparative bar charts of ACE2_gFET before (black bars) and after (red bars) the addition of different concentrations of Spike or mPRO. Data were normalized on Vdirac value max for each measurement average; (**E**) Schematic representation of Ab_gFET; (**F-G**) Ids-Vg curves obtained as the mean of six different measurements on the same device of (**F**) Ab_gFET (black) and Ab_gFET-Spike (red), Spike protein was 2 µg/mL, Vdirac is marked; (**G**) Ab_gFET (black) and Ab_gFET-mPRO (red), mPRO protein was 2 µg/mL; (**H**) Comparative bar charts of Ab_gFET before (black bars) and after (red bars) the addition of different concentrations of Spike or mPRO. Data were normalized on Vdirac value max for each measurement average. In (**D**) and (**H**): ***P<.001, *P>.05, mean n=6, t-test discovery determined using the Two-stage linear step-up procedure of Benjamini, Krieger and Yekutieli, with Q = 1%. Error bars represent s.d., n=6.

8.4 ACE2-Fc chimera as a new gFET bioreceptor

To prevail over the lower sensitivity of soluble ACE2_gFET with respect to Ab_gFET, we designed an engineered version of ACE2, composed by the protein fused with a Fc-tag at its C-terminus (ACE2-Fc). The Fc-tag from antibodies contains disulphide bridges and we expected that their presence would enforce the formation and stability of dimeric ACE2 complex in solution, mimicking what happens in biological conditions on the cell membrane (Yan et al., 2020). To investigate this new construct in which disulphide bridges should stabilize the dimeric conformation of ACE2, we have performed both computational and experimental techniques. Firstly, using MetaDynamic simulation (MetaD) we have characterized the three system previously described: i) a complete ACE2 system with transmembrane helices embedded in a POPC:CHOL (90:10) membrane (Fig. 34 A, B); ii) the new chimeric system composed of the soluble portion (PD, CLD, ND) of ACE2, linked to Fc (Fig. 34 D, ACE2-Fc), and iii) the soluble version of ACE2 (Fig. 34 C). In the ACE2-Fc chimeric system we observed the formation of a stable conformation after about 100 ns and retained for the rest of the 500 ns sampled (Fig. 34 E). This conformation is maintained by the interaction established between Fc and the CLD region of ACE2. (Fig. 34 D). This dimeric conformation is very similar to the membrane embedded one. Moreover, with the aim of comparing the dynamics of the three systems, we computed the RMSD between the PD domains (Fig. 34 E, F). This analysis revealed a certain degree of flexibility for all systems analyzed, most of them was due to a hinge-bending motion of the receptor. To quantify this motion, we measured the distance between the centre of mass of the PD domains (Fig. 34 H). According to our results, in physiological ACE2 and chimeric ACE2-Fc the two chains are fluctuating around the distance value of 7 nm, rarely sampling more open

conformations (up to 8 nm). On the other hand, in the soluble ACE2 the monomers tend to separate each other more widely (Fig. 34 H, grey curve). A comparison of the number of contacts occurring in the soluble part of ACE2, involving the PD and CLD regions, revealed a similar number of interactions for physiological ACE2 and ACE2-Fc, while soluble ACE2 system loses more contacts over time (Fig. 34 G). Another confirm on the more stable dimeric organization is the cross correlation of the flexibility of single residues during the simulation time. The resultant maps (Fig. 34 I, L) clearly show how the internal dynamics of ACE2-Fc seem like the membrane embedded ACE2, especially in the PD domain involved in the interaction with Spike. On the other hand, the soluble ACE2 shows more evident differences both in the profile and intensities of the correlated motions (Fig. 34 L). Next, we sought to validate the data obtained through computational investigation on the ACE2-Fc dimerization propensity, by performing non-denaturing SDS-PAGE electrophoresis with and without β-mercaptethanol to ACE2-Fc samples. β-mercaptethanol is used as a reducing agent capable of breaking disulphide bonds. As shown in figure 34 M, when ACE2-Fc is treated with β-mercaptethanol (Wβ), the disulphide bonds present in the Fc region are reduced and the protein is in monomeric conformation. On the other hand, when ACE2-Fc is loaded on the gel without β-mercaptethanol (W/o β), the protein is separated by acrylamide as a dimer, confirming the computational analysis. Figure 34 M shows also soluble ACE2 loaded in SDS-PAGE with or without β-mercaptethanol. In both conditions, ACE2 is in monomeric conformation confirming the absence of disulphide bonds able to force the protein in dimeric conformation. Similarly to ACE2 and Ab, we have confirmed, also for ACE2-Fc, the interaction with the trimeric spike protein through pull-down assay and western blot detection (Fig. 34 N).

Taken together, these results indicate that the chimeric ACE2-Fc system preserve the dynamical properties of ACE2 in membrane and gFET functionalization with this chimera could represent a successful strategy to enhance the performance of the biosensor.

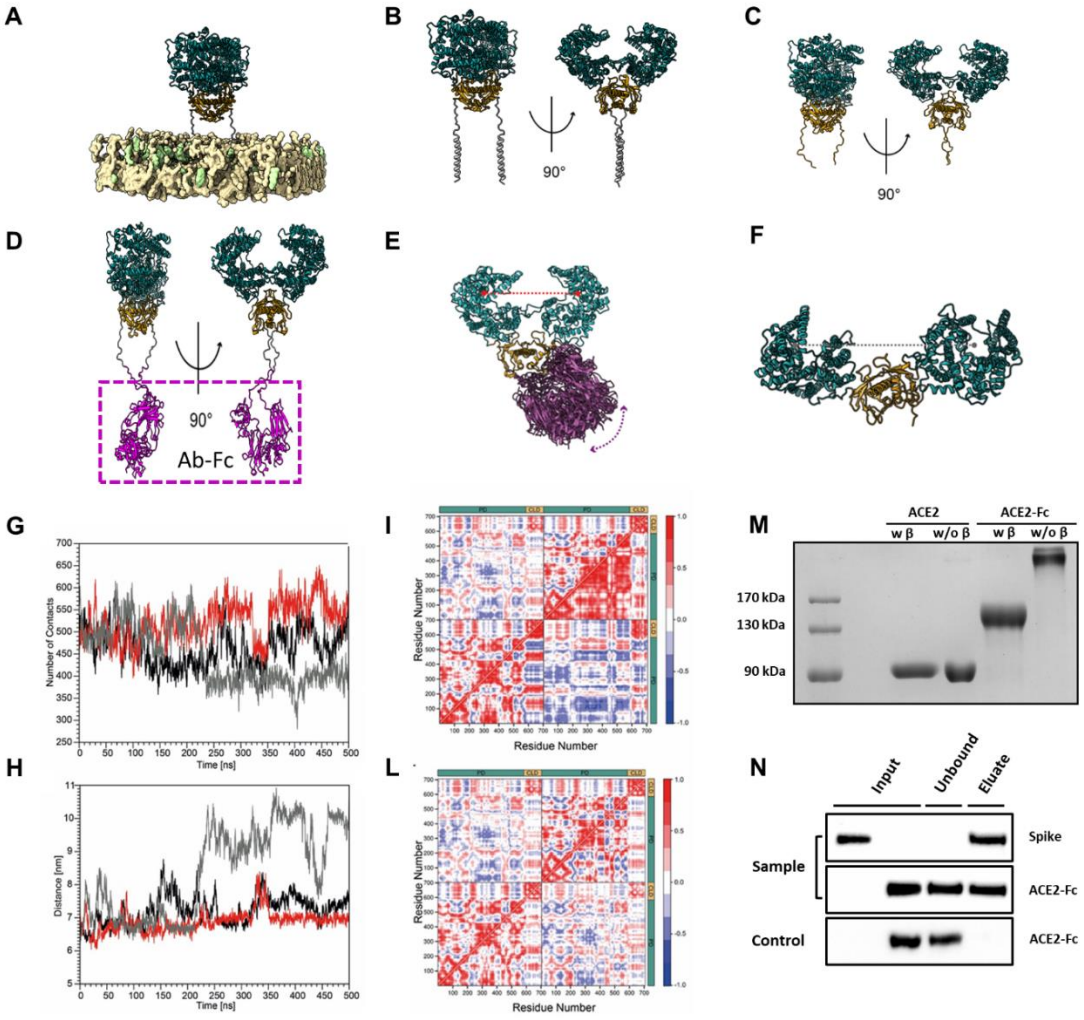

Figure 34 Design and characterization of chimeric ACE2-Fc.

(**A**) Ribbon representation of the full length ACE2 dimer embedded in a phospholipidic membrane; (**B**) Ribbon representation of full length ACE2 dimer; (**C**) Ribbon representation of truncated soluble ACE2; (**D**) Ribbon representation of chimeric ACE2-Fc dimer, Fc from antibodies is highlighted in violet; For (**B-C-D**) two orthogonal views are shown; (**E**) Representative snapshots of ACE2-Fc structures sampled during the MD trajectory. The PD centres of mass distance is shown by a dashed red line; (**F**) top view of soluble ACE2, the PD centres of mass distance is shown by a dashed black line; (**G**) Number of contacts between the two PD-CLD regions of monomers for membrane embedded full length ACE2 (in black), ACE2-Fc (red) and soluble ACE2 (grey);

(**H**) Time evolution of the intermonomer distance measured between the PD domains, colour code as in (**G**). Comparative Dynamics as reported by the cross-correlation matrices of concerted motions of the residues of our three dimeric systems during the MD simulations; In (**I**) correlations in the full length ACE2 embedded in the membrane (upper triangle) and soluble truncated ACE2 (lower triangle); (**L**) same comparison as (**I**) between full length ACE2 embedded in the membrane (upper triangle) and ACE2-Fc (lower triangle). (**M**) SDS-PAGE under reducing (w β lanes) and non-reducing (w/o β lanes) conditions of soluble ACE2 and ACE2-Fc; (**N**) Pull-down assay of Spike and ACE2-Fc. The binding of Spike with ACE2-Fc was monitored by Western blot.

8.5 SARS-CoV-2 Spike protein detection by ACE2-Fc_gFET

After confirming the ACE2-Fc dimeric propensity and ACE2-Fc-spike interaction we proceeded with the functionalization of an empty gFET with ACE2-Fc (Fig. 35 A). The ACE2-Fc-functionalized gFET (ACE2-FC_gFET) was used to test the sensor response and sensitivity using four different Spike concentrations (2 µg/ml – 0.2 µg/ml – 0.04 µg/ml – 0.02 µg/ml); the same concentrations of mPRO were used to assess the specificity of the bioreceptor binding to Spike RBD. All analyses were conducted using the same measurement protocol previously used (for more details see materials and methods section). Figure 35 (B, C) shows the comparison between ACE2-Fc_gFET and ACE2-Fc_gFET incubated with Spike and mPRO. When 2 µg/mL of Spike protein is added to the gFET functionalized with the chimeric ACE2-Fc, a negative shift of curves, comparable with the one obtained using Ab_gFET (Fig. 33 F), is observed; a negative shift is still detectable when using a Spike concentration of 0.2 µg/mL (Fig. 35 C). Of note, the intensity of the shift is higher than the signal obtained using the antibody as bioreceptor, denoting a higher sensitivity. Further reducing the spike concentration (0.04 µg/mL and 0.02 µg/mL) brings to a still appreciable curves change (Fig. 35 C, curves not shown). The signals obtained by testing four different concentrations of mPRO are mainly the same to the ones acquired with the bioreceptor alone (Fig. 35 C), denoting the absence of the interaction. Furthermore, the possible cross-reactivity between our ACE2-Fc and the Spike from MERS-CoV has been questioned. After the addition of 2 µg/mL of MERS Spike, there was no significant shift of $V_{dirac,}$ compared to the blank, meaning an absence of interaction (Fig. 35 D).

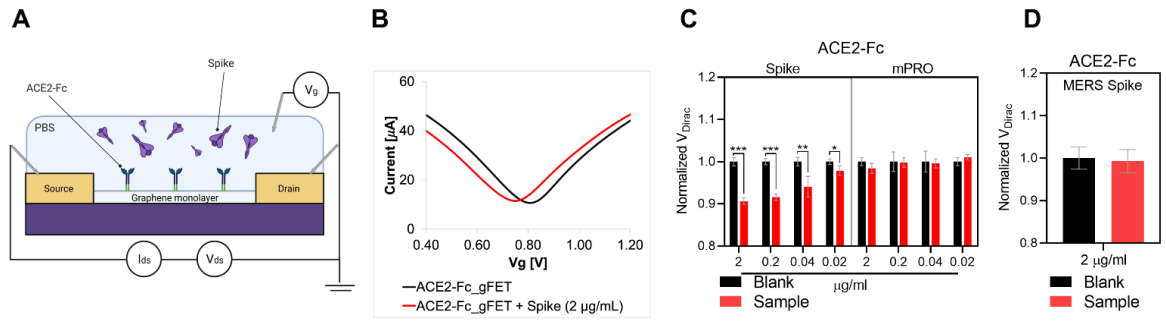

Figure 35 ACE2-Fc_gFET setup and Spike recognition.

(**A**) Schematic representation of ACE2-Fc_gFET; (**B**) Ids-Vg curves obtained as the mean of six different measurements on the same device of ACE2-Fc_gFET (black) and ACE2-Fc_gFET-Spike (red), Spike protein was 2 µg/mL; (**C**) Comparative bar chart showing the ACE2-Fc_gFET response to different concentrations of Spike (left) or mPRO (right); ***P<.001, **P<.01 and *P<.05. (**D**) Comparative bar chart showing the ACE2-Fc_gFET response to 2 µg/ml of MERS-CoV Spike protein, n=6.

8.6 Device prototyping

These electrical results were obtained using a Wentworth probe station equipped with a Bausch & Lomb MicroZoom optical microscope (Fig. 36 A) and by using an HP4145B semiconductor parameter analyser (Fig. 36 B), all bulky laboratory instruments. However, the final aim of this work was to make the biosensor accessible to a wide and non-specialized audience and make it possible to use and deploy this type of device not only in a laboratory with specialized electronic instruments available. This was achieved thanks to the collaboration with the Department of Information Engineering of Università Politecnica delle Marche (UnivPM), by designing and building a customized electronic readout device (Fig. 36 C). The designed device can analyze the electrical response of all the 12 transistors in a Graphenea gFET-S20 chip without user intervention, so as to average out possible differences in the individual transistor responses and be resilient to the presence of a few malfunctioning or deteriorated transistors on the chip (which is an occurrence which happened quite frequently in the laboratory experiments). The device is composed of signal acquisition board linked to an interchangeable gFET biosensor cartridge (Fig. 36 C). A Bluetooth Low Energy (BLE) wireless connection allows the device to communicate with a PC. Moreover, a functional yet aesthetically pleasing case for the device was designed to be 3D printed. Our new device is able to give same readouts of the lab scale probe station used during sensor implementation and testing.

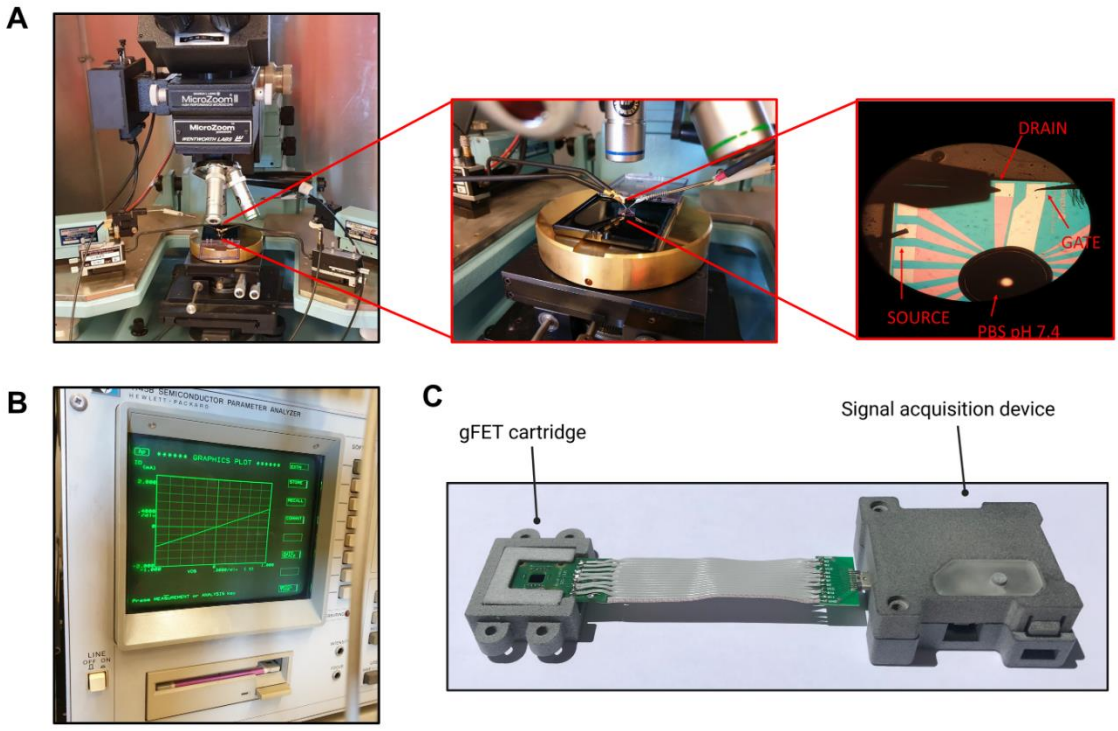

Figure 36 Old and new detect systems used during electrical measurements.

(**A**) Picture of Wentworth probe station equipped with a Bausch & Lomb MicroZoom optical microscope; In the two red insets of panel A are present respectively the pictures of Graphenea S-20 chip under electrodes and of the same chip seen from 10x magnification; (**B**) Picture of HP4145B semiconductor parameter analyser; (**C**) Picture of the gFET Cartridge Unit and the Signal acquisition module connected together to form the entire device.

8.7 Detection of SARS-CoV-2 variants from both cultured viruses and nasopharyngeal swab by point-of-care device

Thanks to the portable device (Fig. 36 C), we were able to test the electrical performance of our ACE2-Fc_gFET on different SARS-CoV-2 variants using both isolated virus and nasopharyngeal swab specimens from reals patients. Different inactivated SARS-CoV-2 variants, at the same concentration (Table 3), were assessed to evaluate the electrical performance of the biosensor (Fig. 37 A).

Variant	CT Average
B.1.610 $_1$	21.23
B.1.610 $_2$	21.32
Alpha	22.26
Beta	20.89
Gamma	20.47
Delta	19.11
Omicron	19.96

Table 3. Isolated virus samples.

The type of virus variant (detected by targeted RT-qPCR) and relative Ct value of different samples are reported. The value of CT is an average between the CT values of three SARS-CoV-2 specific genes (E gene; RdRP/S gene; N gene) evaluated with RT-qPCR.

The analysis of Pre-VOC D614G (B.1.610) and four VOC (Alpha, Beta, Gamma, Delta), including the recently emerged Omicron, have shown a shift of the Dirac point for all the variants tested (Fig. 37 A). Interestingly, the effect of whole virus particles on the response of the biosensor results in both n-dope and p-dope directions of the Dirac point highlighting that, unlike the recombinant Spike, the whole-particle virus is a more complex system. Considering this, the negative control acquires considerable importance in the experimental design and we used, for this purpose, the HSV-1 virus particle at the same concentration of SARS-CoV-2 samples. As clearly show in figure 37 A, HSV-1 does not exhibit any shift in the Dirac point, validating that the specificity of the interaction together with the strictly washing steps in our protocol yield significant differences only in presence of the correct viral target.

Next, we tested the detection performance of our ACE2-Fc_gFET using clinical samples directly to the hospital (Summarized in Table 4). Figure 37 B shows the normalized value of the gate voltage at the Dirac point of eight different patient samples.

Variant	CT Average
B.1.610	16.23
Alpha	25.3
Gamma	14.0
Delta $_1$	14.5
Delta $_2$	18.43
Omicron	20.24

Table 4. Clinical nasopharyngeal swab samples.

Different SARS-CoV-2 variants and relative Ct values in positive clinical samples.

These results demonstrate that our ACE2-Fc_gFET sensor clearly discriminates between SARS-CoV-2 positive and negative samples. RT-qPCR results have confirmed that six patients were positive to SARS-CoV-2 (Table 4), carrying B.1.610, Alpha, Gamma, two Delta and Omicron, while the other two tested were negative. These findings show that our ACE2-Fc_gFET can successfully detect SARS-CoV-2 from both isolated SARS-CoV-2 and nasopharyngeal swab specimens without any pre-processing steps.

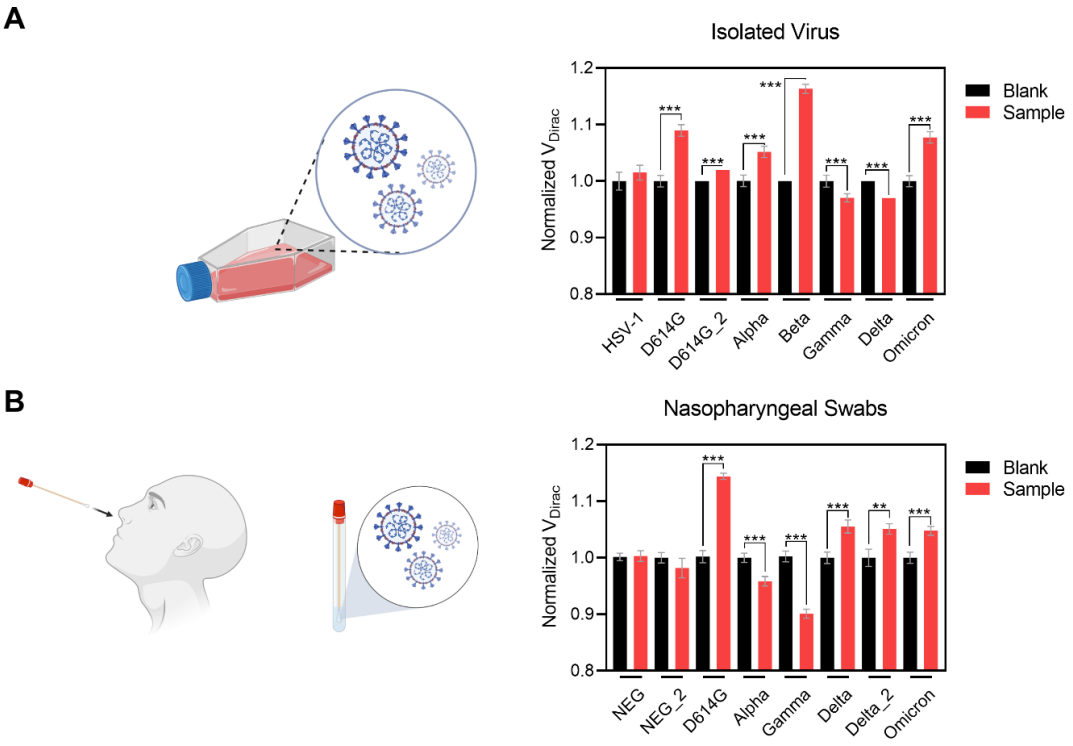

Figure 37 The portable device detects SARS-CoV-2 variants in both isolated virus and clinical samples.

(**A**) Bar graph reporting ACE2-Fc_gFET signal before (black) and after the addition of isolated and inactivated SARS-CoV-2 samples (red). ***P<.001; n=6; (**B**) Bar graph reporting ACE2-Fc_gFET signal before (black) and after the addition of nasopharyngeal swab samples from patients (red). **P<.01; ***P<.001; n=6.

9 DISCUSSION

COVID-19 pandemic is changing the world. Since the first case in Wuhan, the COVID-19 pandemic has continued to spread around the globe, with over 394.381.395 confirmed cases of COVID-19, including 5.735.179 deaths, reported to WHO as of the end of January 2022 (https://covid19.who.int/). Although the number of vaccinated is increasing day by day, the virus is far from being contained especially because of the continuous emergence of more contagious variants of concern (Mohapatra et al., 2022) capable to evade the immune system and reinfect people previously infected (Jeffery-Smith et al., 2021). Each of these variants harbours a set of specific changes located on different viral proteins, many of them being found in specific regions of the Spike protein, such as in the Receptor Binding Domain (RBD) which physically interacts with the ACE2 receptor during the early step of the host cell infection. These mutations significantly decrease neutralization and recognition of antibodies generated during previous infection or vaccination (Jeffery-Smith et al., 2021). This phenomenon has an indirect consequence also on the antibody-related antigenic tests resulting in a widespread interference and in the failure of virus detection (false negative) (Bekliz et al., 2022). On the other hand, the same mutations encourage an increase in the magnitude of infection (Harvey et al., 2021) because some of them strengthen the interaction between Spike and human host receptor ACE2.

More in detail, N501Y change has been described to increase affinity to ACE2 by 7-fold, and the additive pattern of substitutions K417N, E484A, and N501Y have shown further increased affinity to ACE2 (19-fold compared to Wuhan SARS-CoV-2) (Shrestha et al., 2021). Omicron variant presents all these residue changes (McCallum et al., 2021) and so many others, making it, as well as more contagious, also difficult to detect by standard diagnostic tests

(Cameroni et al., 2022). This might be a serious problem in the actual surveillance and containment of pandemic.

In this situation, there is a need to find new variant-robust detection systems able to recognize all SARS-CoV-2 circulating variants. Considering that the immune selection drives the virus towards the capability to skip antibodies but not the human receptor, we thought of exploiting the specific interaction between Spike and ACE2 to develop a multi-variants robust detection system based on graphene field-effect transistor technology.

Our study combined different approaches, crossing from computational techniques and biochemical assays up to engineering analyses and device prototyping.

Using steered molecular dynamics simulation, we have evaluated at the single-molecule level the binding strength of the interaction established between the RBD domain of spike and ACE2 receptor or antibody against Spike (Ab). The obtained values have shown a strong interaction in both bioreceptors. The maximum force observed in simulations at lower pulling speed was around 250 kJ mol-1 nm-1, for ACE2-RBD and Ab-RBD Group 3, a value higher than those reported in AFM experiments (Yang et al., 2020), but expected due to the large difference in the pulling speed used due to computational limitations. Both receptors have been proved to be adapted as biosensor sensing area, but since antibodies could elude spike variants, we have decided to use ACE2 exploiting its specificity in the recognition by the viral spike protein, mutated or not.

Once characterized *in-silico* the interaction between Spike and the two natural receptors, we functionalized commercial gFET chips using ACE2 and Ab in order to analyze *in-vitro* the electrical performance of both biosensors. To do

that, we exploited PBASE linker to attach the bioreceptors on graphene surface. Different concentration of PBASE (2.5, 5, 10 mM) were tested in order to obtain a homogeneous coverage of graphene and, after an *in-depth* characterization using AFM and Raman spectroscopy, 5 mM was found to be the most correct. After bioreceptor conjugation, there might be unbound PBASE which could give false negative signals during the next electrical measurement phases. According to literature, there are many ways to block the free PBASE (Béraud et al., 2021), and among these, we have chosen to use glycine at high concentration (100 mM) in PBS pH 8.4. Amine group of glycine is optimal for the termination of excess PBASE NHS groups (Kwong Hong Tsang et al., 2019). Basic pH (8.4) allows to speed-up and improve the coupling reaction between amine and PBASE NHS group, as described by manufacturers (Thermo Scientific).

First experimental measurement results of ACE2_gFET and Ab_gFET have demonstrated high specificity (no signals after the addition of SARS-CoV-2 mPRO) but very low sensitivity if compared with other gFET biosensor (Seo et al., 2020). For ACE2_gFET, after the addition of 2 μg/ml of recombinant Spike we obtained a left shift of the Dirac Point and no shift after the addition of lower Spike concentrations. On the contrary, Ab_gFET gave us a significant signal also with 0.2 μg/ml of Spike protein denoting a better sensitivity. The high specificity of the system was obtained not only through the specific interaction between the bioreceptor on graphene and its ligand into the solution but also thanks to the stringent washing protocol that we have used during all the electrical experiments. This washing protocol allows to obtain a very high specificity also with more complex samples, such as nasopharyngeal swab specimens, where there is an environment full of proteins, bacteria and other

biological compounds. Without any washing steps, they could aspecifically adsorb on graphene surface, perturbing the electrical signal.

Lack of sensitivity from ACE2_gFET did not stop us from looking for a variant-robust biosensor. As said before, SARS-CoV-2 variants could elude monoclonal antibodies recognition. Therefore, we believe that the use of ACE2 could represent a more promising candidate to next-generation SARS-CoV-2 devices.

Chan et al. in 2020 (Chan et al., 2020c) have demonstrated that stable dimeric ACE2 is two orders of magnitude more potent than monomer, indicating strong and avid interactions with Spike. Considering this, we explore the possibility to use a construct that enforces the formation and stability of dimeric ACE2 complex, mimicking what occurs in physiological conditions. This was obtained by adding to ACE2, at its C-terminus, an Fc-tag whose disulphides help to bridge homodimers, thus it would be more similar to its native state (Yan et al., 2020). ACE2-Fc has been characterized through computational and *in-vitro* biochemical analyses. From computational studies, we have analyzed the RMSD of the transmembrane ACE2 and ACE2-Fc respectively, showing a structural similarity between the native and the chimeric form. From a biochemical point of view, dimeric ACE2-Fc has proved capable to specifically bind Spike protein. Moreover, Fc-tag could improve the PBASE-Protein conjugation because of the exposition of many lysine on the surface of Fc. In fact, NHS group of PBASE reacts with amine side chains of lysine residues due to their good nucleophilicity (Nolting, 2013).

ACE2-Fc_gFET biosensor has revealed great sensitivity (0.02 µg/ml) for spike protein differently from Ab_gFET and ACE2_gFET which have lower limit of detection. In addition, all the conditions tested have exhibited no response to

mPRO, indicating that our biosensor is specific for the SARS-CoV-2 spike protein. Notably, our sensitivity is comparable to that of lateral flow-based devices in which the antibody represents the sensing area of the biosensor (Lee et al., 2021). The non-recognition of mPRO by our ACE2-Fc_gFET biosensor certifies high specificity but possible cross-reactivity with other coronaviruses cannot be excluded. In order to further confirm the specificity of the interaction between ACE2-Fc and the SARS-CoV-2 Spike protein, we tested also the MERS-CoV Spike protein. We did not observe a significant difference using the MERS-CoV Spike protein in solution at 2 μg/ml.

Moreover, since ACE2 is the receptor for only three coronaviruses, one of which is contained and the other, HCoV-NL63, has low binding affinity, specificity is reasonably assured for coronavirus that use ACE2 as host receptor (Beacon et al., 2021).

One of the disadvantages of gFET is the need of bulky instruments to perform electrical measurements. In our case, we used a Wentworth probe station equipped with a Bausch & Lomb MicroZoom optical microscope and by using an HP4145B semiconductor parameter analyser. However, one of the main goals of this project was to achieve portability and to do that, we designed and developed a point-of-care device able to give a response after few minutes. The prototype is easy to use thanks to a practical software directly linked with the device through Bluetooth connection. Moreover, our graphene-based biosensor is reusable producing less plastic waste which results in a more environmentally-friendly system.

After *in-vitro* characterization of the electrical performances of ACE2-Fc_gFET, the biosensor was successfully tested also on complex samples such

as isolated viruses and clinical samples from patients infected by five different virus variants: B.1.610, Alpha, Beta, Gamma, Delta and Omicron.

Considering that highly sensitive PCR-based molecular tests still require a few hours for the result, whereas antigen-detecting rapid diagnostic tests are characterized by lower accuracy, our biosensor could be a valid alternative to the tests currently on the market being able to correctly detect all circulating variants. Accuracy studies coupled with PCR-based molecular tests as a benchmark will be, of course, needed to verify the performance of our POC biosensor with different and upcoming virus variants.

In addition, to further improve sensitivity of ACE2-Fc_gFET, the next step will be to increase the spike binding, according to Chan et al. results (Chan et al., 2020c), with the introduction of specific mutations in the in ACE2 peptidase domain.

In conclusion, another advantage of our system is the versatility. In fact, such a system can be routinely implemented in the design of biosensors, which properly functionalized, could be prominent for the detection of essential biomarkers such as proteins, circulating tumour cells, nucleic acids, and a new class of biomarkers called exosomes, which are gaining prominence. Moreover, a future challenging goal could be adapting the biosensor to even more complex system, such as wastewater and aerosol, in order to detect many pollutants such as chemicals and drugs in both the atmosphere and water.

10REFERENCES

Abbruzzese, A., Hanauske-Abel, H. M., Park, M. H., Henke, S., and Folk, J. E. (1991). The active site of deoxyhypusyl hydroxylase: use of catecholpeptides and their component chelator and peptide moieties as molecular probes. *Biochim. Biophys. Acta (BBA)/Protein Struct. Mol.* 1077, 159–166. doi:10.1016/0167-4838(91)90053-3.

Abraham, M. J., Murtola, T., Schulz, R., Páll, S., Smith, J. C., Hess, B., et al. (2015). GROMACS: High performance molecular simulations through multi-level parallelism from laptops to supercomputers. *SoftwareX* 1–2, 19–25. doi:10.1016/j.softx.2015.06.001.

Afanador, G. A., Tomchick, D. R., and Phillips, M. A. (2018). Trypanosomatid Deoxyhypusine Synthase Activity Is Dependent on Shared Active-Site Complementation between Pseudoenzyme Paralogs. *Structure* 26, 1499-1512.e5. doi:https://doi.org/10.1016/j.str.2018.07.012.

Aleem, A., Akbar Samad, A. B., and Slenker, A. K. (2022). "Emerging Variants of SARS-CoV-2 And Novel Therapeutics Against Coronavirus (COVID-19).," in (Treasure Island (FL)).

Alessandrini, F., Caucci, S., Onofri, V., Melchionda, F., Tagliabracci, A., Bagnarelli, P., et al. (2020). Evaluation of the Ion AmpliSeq SARS-CoV-2 Research Panel by Massive Parallel Sequencing. *Genes* 11. doi:10.3390/genes11080929.

Balibar, C. J., Iwanowicz, D., and Dean, C. R. (2013). Elongation factor P is dispensable in escherichia coli and pseudomonas aeruginosa. *Curr. Microbiol.* 67, 293–299. doi:10.1007/s00284-013-0363-0.

Bartig, I. (1992). The archaebacterial hypusine-containing protein. Structural

features suggest common ancestry with eukaryotic translation initiation factor 5A. 758, 751–758.

Bassani, F. (2017). New functions for an archaeal translation factor.

Bassani, F., Romagnoli, A., Cacciamani, T., Amici, A., Benelli, D., Londei, P., et al. (2018). Modification of translation factor aIF5A from Sulfolobus solfataricus. *Extremophiles* 22, 769–780. doi:10.1007/s00792-018-1037-4.

Bassani, F., Zink, I. A., Pribasnig, T., Wolfinger, M. T., Romagnoli, A., Resch, A., et al. (2019). Indications for a moonlighting function of translation factor aIF5A in the crenarchaeum Sulfolobus solfataricus. *RNA Biol.* 16, 675–685. doi:10.1080/15476286.2019.1582953.

Beacon, T. H., Delcuve, G. P., and Davie, J. R. (2021). Epigenetic regulation of ACE2, the receptor of the SARS-CoV-2 virus(1). *Genome* 64, 386–399. doi:10.1139/gen-2020-0124.

Bekliz, M., Perez-Rodriguez, F., Adea, K., Stéfane Marques Melancia, S. B., Corvaglia, A.-R., Jacquerioz-Bausch, F., et al. (2022). Sensitivity of SARS-CoV-2 antigen-detecting rapid tests for Omicron variant. 1–17. doi:https://doi.org/10.1101/2021.12.18.21268018.

Bell, C. E., Yeates, T. O., and Eisenberg, D. (1997). Unusual conformation of nicotinamide adenine dinucleotide (NAD) bound to diphtheria toxin: A comparison with NAD bound to the oxidoreductase enzymes. *Protein Sci.* 6, 2084–2096. doi:10.1002/pro.5560061004.

Benelli, D., La Teana, A., and Londei, P. (2016). “Evolution of Translational

Initiation: From Archaea to Eukarya," in, 61–79. doi:10.1007/978-3-319-39468-8_4.

Benne, R., Brown-Luedi, M. L., and Hershey, J. W. (1978). Purification and characterization of protein synthesis initiation factors eIF-1, eIF-4C, eIF-4D, and eIF-5 from rabbit reticulocytes. *J. Biol. Chem.* 253, 3070–3077.

Béraud, A., Sauvage, M., Bazán, C. M., Tie, M., Bencherif, A., and Bouilly, D. (2021). Graphene field-effect transistors as bioanalytical sensors: Design, operation and performance. *Analyst* 146, 403–428. doi:10.1039/d0an01661f.

Bevec, D., Jaksche, H., Oft, M., Wöhl, T., Himmelspach, M., Pacher, A., et al. (1996). Inhibition of HIV-1 replication in lymphocytes by mutants of the Rev cofactor eIF-5A. *Science* 271, 1858–1860. doi:10.1126/science.271.5257.1858.

Bordi, L., Nicastri, E., Scorzolini, L., Di Caro, A., Capobianchi, M. R., Castilletti, C., et al. (2020). Differential diagnosis of illness in patients under investigation for the novel coronavirus (SARS-CoV-2), Italy, February 2020. *Euro Surveill. Bull. Eur. sur les Mal. Transm. = Eur. Commun. Dis. Bull.* 25. doi:10.2807/1560-7917.ES.2020.25.8.2000170.

Brown, M. A., Crosser, M. S., Leyden, M. R., Qi, Y., and Minot, E. D. (2016). Measurement of high carrier mobility in graphene in an aqueous electrolyte environment. *Appl. Phys. Lett.* 109. doi:10.1063/1.4962141.

Bullwinkle, T. J., Zou, S. B., Rajkovic, A., Hersch, S. J., Elgamal, S., Robinson, N., et al. (2013). (R)-β-lysine-modified elongation factor p functions in translation elongation. *J. Biol. Chem.* 288, 4416–4423.

doi:10.1074/jbc.M112.438879.

Bussi, G., Donadio, D., and Parrinello, M. (2007). Canonical sampling through velocity-rescaling. *J. Chem. Phys.* 126, 014101.

Cai, X., Wang, R., Filloux, A., Waksman, G., and Meng, G. (2011). Structural and functional characterization of Pseudomonas aeruginosa CupB chaperones. *PLoS One* 6, e16583. doi:10.1371/journal.pone.0016583.

Cameroni, E., Bowen, J. E., Rosen, L. E., Saliba, C., Zepeda, S. K., Culap, K., et al. (2022). Broadly neutralizing antibodies overcome SARS-CoV-2 Omicron antigenic shift. *Nature* 602, 664–670. doi:10.1038/s41586-021-04386-2.

Caraglia, M., Marra, M., Giuberti, G., D'Alessandro, A. M., Baldi, A., Tassone, P., et al. (2003). The eukaryotic initiation factor 5A is involved in the regulation of proliferation and apoptosis induced by interferon-alpha and EGF in human cancer cells. *J. Biochem.* 133, 757–765. doi:10.1093/jb/mvg097.

Carson, M., Johnson, D. H., McDonald, H., Brouillette, C., and Delucas, L. J. (2007). His-tag impact on structure. *Acta Crystallogr. D. Biol. Crystallogr.* 63, 295–301. doi:10.1107/S0907444906052024.

Chan, J. F.-W., Kok, K.-H., Zhu, Z., Chu, H., To, K. K.-W., Yuan, S., et al. (2020a). Genomic characterization of the 2019 novel human-pathogenic coronavirus isolated from a patient with atypical pneumonia after visiting Wuhan. *Emerg. Microbes Infect.* 9, 221–236. doi:10.1080/22221751.2020.1719902.

Chan, J. F.-W., Yip, C. C.-Y., To, K. K.-W., Tang, T. H.-C., Wong, S. C.-Y., Leung,

K.-H., et al. (2020b). Improved Molecular Diagnosis of COVID-19 by the Novel, Highly Sensitive and Specific COVID-19-RdRp/Hel Real-Time Reverse Transcription-PCR Assay Validated In Vitro and with Clinical Specimens. *J. Clin. Microbiol.* 58. doi:10.1128/JCM.00310-20.

Chan, K. K., Dorosky, D., Sharma, P., Abbasi, S. A., Dye, J. M., Kranz, D. M., et al. (2020c). Engineering human ACE2 to optimize binding to the spike protein of SARS coronavirus 2. *Science (80-.).* 369, 1261–1265. doi:10.1126/SCIENCE.ABC0870.

Chen, M., Gai, Z., Okada, C., Ye, Y., Yu, J., and Yao, M. (2020). Flexible NAD+ binding in deoxyhypusine synthase reflects the dynamic hypusine modification of translation factor IF5A. *Int. J. Mol. Sci.* 21, 1–14. doi:10.3390/ijms21155509.

Clement, P. M. J., Henderson, C. A., Jenkins, Z. A., Smit-McBride, Z., Wolff, E. C., Hershey, J. W. B., et al. (2003). Identification and characterization of eukaryotic initiation factor 5A-2. *Eur. J. Biochem.* 270, 4254–4263. doi:10.1046/j.1432-1033.2003.03806.x.

Clement, P. M. J., Johansson, H. E., Wolff, E. C., and Park, M. H. (2006). Differential expression of eIF5A-1 and eIF5A-2 in human cancer cells. *FEBS J.* 273, 1102–1114. doi:10.1111/j.1742-4658.2006.05135.x.

Corman, V. M., Landt, O., Kaiser, M., Molenkamp, R., Meijer, A., Chu, D. K., et al. (2020). Detection of 2019 novel coronavirus (2019-nCoV) by real-time RT-PCR. *Euro Surveill. Bull. Eur. sur les Mal. Transm. = Eur. Commun. Dis. Bull.* 25. doi:10.2807/1560-7917.ES.2020.25.3.2000045.

Cougnon, M., Carcy, R., Melis, N., Rubera, I., Duranton, C., Dumas, K., et al.

(2021). Inhibition of eIF5A hypusination reprogrammes metabolism and glucose handling in mouse kidney. *Cell Death Dis.* 12, 283. doi:10.1038/s41419-021-03577-z.

Cui, J., Li, F., and Shi, Z.-L. (2019). Origin and evolution of pathogenic coronaviruses. *Nat. Rev. Microbiol.* 17, 181–192. doi:10.1038/s41579-018-0118-9.

D'Agostino, M., Romagnoli, A., Di Marino, D., and La Teana, A. (2020). Insights in the Binding Mechanism of GC7 in Sulfolobus solfataricus: Toward the Design of New Inhibitors of the Deoxyhypusine Synthase. *Biophys. J.* 118, 361a. doi:10.1016/j.bpj.2019.11.2077.

Doerfel, L. K., Wohlgemuth, I., Kothe, C., Peske, F., Urlaub, H., and Rodnina, M. V (2013). EF-P is essential for rapid synthesis of proteins containing consecutive proline residues. *Science* 339, 85–88. doi:10.1126/science.1229017.

Donoghue, M., Hsieh, F., Baronas, E., Godbout, K., Gosselin, M., Stagliano, N., et al. (2000). UltraRapid Communication A Novel Angiotensin-Converting Enzyme – Related to Angiotensin 1-9. *Circ Res* 87, e1–e9.

Essmann, U., Perera, L., Berkowitz, M. L., Darden, T., Lee, H., and Pedersen, L. G. (1995). A smooth particle mesh Ewald method. *J. Chem. Phys.* 103, 8577–8593. doi:10.1063/1.470117.

Forsyth, R., Devadoss, A., and Guy, O. J. (2017). Graphene Field Effect Transistors for Biomedical Applications: Current Status and Future Prospects. *Diagnostics (Basel, Switzerland)* 7. doi:10.3390/diagnostics7030045.

Gäbel, K., Schmitt, J., Schulz, S., Näther, D. J., and Soppa, J. (2013). A comprehensive analysis of the importance of translation initiation factors for haloferax volcanii applying deletion and conditional depletion mutants. *PLoS One* 8. doi:10.1371/journal.pone.0077188.

Gutierrez, E., Shin, B.-S., Woolstenhulme, C. J., Kim, J.-R., Saini, P., Buskirk, A. R., et al. (2013). eIF5A promotes translation of polyproline motifs. *Mol. Cell* 51, 35–45. doi:10.1016/j.molcel.2013.04.021.

Hanawa-Suetsugu, K., Sekinet, S. I., Sakai, H., Hori-Takemoto, C., Terada, T., Unzai, S., et al. (2004). Crystal structure of elongation factor P from Thermus thermophilus HB8. *Proc. Natl. Acad. Sci. U. S. A.* 101, 9595–9600. doi:10.1073/pnas.0308667101.

Harvey, W. T., Carabelli, A. M., Jackson, B., Gupta, R. K., Thomson, E. C., Harrison, E. M., et al. (2021). SARS-CoV-2 variants, spike mutations and immune escape. *Nat. Rev. Microbiol.* 19, 409–424. doi:10.1038/s41579-021-00573-0.

Hauber, I., Bevec, D., Heukeshoven, J., Krätzer, F., Horn, F., Choidas, A., et al. (2005). Identification of cellular deoxyhypusine synthase as a novel target for antiretroviral therapy. *J. Clin. Invest.* 115, 76–85. doi:10.1172/JCI21949.

Hess, B. (2008). P-LINCS: A Parallel Linear Constraint Solver for Molecular Simulation. *J. Chem. Theory Comput.* 4, 116–122. doi:10.1021/ct700200b.

Hsieh, C.-L., Goldsmith, J. A., Schaub, J. M., DiVenere, A. M., Kuo, H.-C., Javanmardi, K., et al. (2020). Structure-based design of prefusion-stabilized SARS-CoV-2 spikes. *Science* 369, 1501–1505.

doi:10.1126/science.abd0826.

Hu, B., Guo, H., Zhou, P., and Shi, Z.-L. (2021). Characteristics of SARS-CoV-2 and COVID-19. *Nat. Rev. Microbiol.* 19, 141–154. doi:10.1038/s41579-020-00459-7.

Huang, C., Wang, Y., Li, X., Ren, L., Zhao, J., Hu, Y., et al. (2020a). Clinical features of patients infected with 2019 novel coronavirus in Wuhan, China. *Lancet (London, England)* 395, 497–506. doi:10.1016/S0140-6736(20)30183-5.

Huang, J., Rauscher, S., Nawrocki, G., Ran, T., Feig, M., de Groot, B. L., et al. (2017). CHARMM36m: an improved force field for folded and intrinsically disordered proteins. *Nat. Methods* 14, 71–73. doi:10.1038/nmeth.4067.

Huang, X. M., Liu, L. Z., Zhou, S., and Zhao, J. J. (2020b). Physical properties and device applications of graphene oxide. *Front. Phys.* 15. doi:10.1007/s11467-019-0937-9.

Huang, Z., Tian, D., Liu, Y., Lin, Z., Lyon, C. J., Lai, W., et al. (2020c). Ultra-sensitive and high-throughput CRISPR-p owered COVID-19 diagnosis. *Biosens. Bioelectron.* 164, 112316. doi:10.1016/j.bios.2020.112316.

Igarashi, K., and Kashiwagi, K. (2018). Effects of polyamines on protein synthesis and growth of Escherichia coli. *J. Biol. Chem.* 293, 18702–18709. doi:10.1074/jbc.TM118.003465.

Jakus, J., Wolff, E. C., Park, M. H., and Folk, J. E. (1993). Features of the spermidine-binding site of deoxyhypusine synthase as derived from inhibition studies. Effective inhibition by bis- and mono-guanylated

diamines and polyamines. *J. Biol. Chem.* 268, 13151–13159.

Jansson, B. P. M., Malandrin, L., and Johansson, H. E. (2000). Cell cycle arrest in archaea by the hypusination inhibitor N1-guanyl- 1,7-diaminoheptane. *J. Bacteriol.* 182, 1158–1161. doi:10.1128/JB.182.4.1158-1161.2000.

Jao, D. L.-E., and Chen, K. Y. (2006). Tandem affinity purification revealed the hypusine-dependent binding of eukaryotic initiation factor 5A to the translating 80S ribosomal complex. *J. Cell. Biochem.* 97, 583–598. doi:10.1002/jcb.20658.

Jeffery-Smith, A., Rowland, T. A. J., Patel, M., Whitaker, H., Iyanger, N., Williams, S. V, et al. (2021). Reinfection with new variants of SARS-CoV-2 after natural infection: a prospective observational cohort in 13 care homes in England. *Lancet. Heal. Longev.* 2, e811–e819. doi:10.1016/S2666-7568(21)00253-1.

Joe, Y. A., Wolff, E. C., Lee, Y. B., and Park, M. H. (1997). Enzyme-substrate intermediate at a specific lysine residue is required for deoxyhypusine synthesis. The role of Lys329 in human deoxyhypusine synthase. *J. Biol. Chem.* 272, 32679–32685. doi:10.1074/jbc.272.51.32679.

Jones, T., Sheer, D., Kapetanopoulos, A., Hauber, J., Bevec, D., and Steinkasserer, A. (1996). The gene coding for human deoxyhypusine synthase (DHPS) maps to chromosome 19p13.11-p13.12. *Genomics* 35, 635–637. doi:10.1006/geno.1996.0416.

Kaiser, A., Hammels, I., Gottwald, A., Nassar, M., Zaghloul, M. S., Motaal, B. A., et al. (2007). Modification of eukaryotic initiation factor 5A from Plasmodium vivax by a truncated deoxyhypusine synthase from

Plasmodium falciparum: An enzyme with dual enzymatic properties. *Bioorganic Med. Chem.* 15, 6200–6207. doi:10.1016/j.bmc.2007.06.026.

Kang, H. A., and Hershey, J. W. (1994). Effect of initiation factor eIF-5A depletion on protein synthesis and proliferation of Saccharomyces cerevisiae. *J. Biol. Chem.* 269, 3934–3940.

Kang, H., Wang, X., Guo, M., Dai, C., Chen, R., Yang, L., et al. (2021). Ultrasensitive Detection of SARS-CoV-2 Antibody by Graphene Field-Effect Transistors. *Nano Lett.* 21, 7897–7904. doi:10.1021/acs.nanolett.1c00837.

Kang, K. R., and Chung, S. I. (1999). Characterization of yeast deoxyhypusine synthase: PKC-dependent phosphorylation in vitro and functional domain identification. *Exp. Mol. Med.* 31, 210–216. doi:10.1038/emm.1999.34.

Kemper, W. M., Berry, K. W., and Merrick, W. C. (1976). Purification and properties of rabbit reticulocyte protein synthesis initiation factors M2Bα and M2Bβ. *J. Biol. Chem.* 251, 5551–5557. doi:10.1016/s0021-9258(17)33095-8.

Kim, D. H., Oh, H. G., Park, W. H., Jeon, D. C., Lim, K. M., Kim, H. J., et al. (2018). Detection of alpha-fetoprotein in hepatocellular carcinoma patient plasma with graphene field-effect transistor. *Sensors (Switzerland)* 18. doi:10.3390/s18114032.

Kwong Hong Tsang, D., Lieberthal, T. J., Watts, C., Dunlop, I. E., Ramadan, S., del Rio Hernandez, A. E., et al. (2019). Chemically Functionalised Graphene FET Biosensor for the Label-free Sensing of Exosomes. *Sci. Rep.* 9, 2–11. doi:10.1038/s41598-019-50412-9.

Lan, J., Ge, J., Yu, J., Shan, S., Zhou, H., Fan, S., et al. (2020). Structure of the SARS-CoV-2 spike receptor-binding domain bound to the ACE2 receptor. *Nature* 581, 215–220. doi:10.1038/s41586-020-2180-5.

Lee, J.-H., Choi, M., Jung, Y., Lee, S. K., Lee, C.-S., Kim, J., et al. (2021). A novel rapid detection for SARS-CoV-2 spike 1 antigens using human angiotensin converting enzyme 2 (ACE2). *Biosens. Bioelectron.* 171, 112715. doi:10.1016/j.bios.2020.112715.

LEE, Y. B., JOE, Y. A., WOLFF, E. C., DIMITRIADIS, E. K., and PARK, M. H. (1999). Complex formation between deoxyhypusine synthase and its protein substrate, the eukaryotic translation initiation factor 5A (eIF5A) precursor. *Biochem. J.* 340, 273–281. doi:10.1042/bj3400273.

Letko, M., Marzi, A., and Munster, V. (2020). Functional assessment of cell entry and receptor usage for SARS-CoV-2 and other lineage B betacoronaviruses. *Nat. Microbiol.* 5, 562–569. doi:10.1038/s41564-020-0688-y.

Levasseur, E. M., Yamada, K., Piñeros, A. R., Wu, W., Syed, F., Orr, K. S., et al. (2019). Hypusine biosynthesis in β cells links polyamine metabolism to facultative cellular proliferation to maintain glucose homeostasis. *Sci. Signal.* 12. doi:10.1126/scisignal.aax0715.

Li, J., Wu, D., Yu, Y., Li, T., Li, K., Xiao, M.-M., et al. (2021). Rapid and unamplified identification of COVID-19 with morpholino-modified graphene field-effect transistor nanosensor. *Biosens. Bioelectron.* 183, 113206. doi:10.1016/j.bios.2021.113206.

Li, Z., and Chen, G. Y. (2018). Current conjugation methods for

immunosensors. *Nanomaterials* 8, 1–11. doi:10.3390/nano8050278.

Liang, Y., Piao, C., Beuschel, C. B., Toppe, D., Kollipara, L., Bogdanow, B., et al. (2021). eIF5A hypusination, boosted by dietary spermidine, protects from premature brain aging and mitochondrial dysfunction. *Cell Rep.* 35, 108941. doi:10.1016/j.celrep.2021.108941.

Liao, D. I., Wolff, E. C., Park, M. H., and Davies, D. R. (1998). Crystal structure of the NAD complex of human deoxyhypusine synthase: An enzyme with a ball-and-chain mechanism for blocking the active site. *Structure* 6, 23–35. doi:10.1016/s0969-2126(98)00004-5.

Lu, R., Zhao, X., Li, J., Niu, P., Yang, B., Wu, H., et al. (2020). Genomic characterisation and epidemiology of 2019 novel coronavirus: implications for virus origins and receptor binding. *Lancet* 395, 565–574. doi:10.1016/S0140-6736(20)30251-8.

Luchessi, A. D., Cambiaghi, T. D., Hirabara, S. M., Lambertucci, R. H., Silveira, L. R., Baptista, I. L., et al. (2009). Involvement of eukaryotic translation initiation factor 5A (eIF5A) in skeletal muscle stem cell differentiation. *J. Cell. Physiol.* 218, 480–489. doi:10.1002/jcp.21619.

Maier, B., Ogihara, T., Trace, A. P., Tersey, S. A., Robbins, R. D., Chakrabarti, S. K., et al. (2010). The unique hypusine modification of eIF5A promotes islet beta cell inflammation and dysfunction in mice. *J. Clin. Invest.* 120, 2156–2170. doi:10.1172/JCI38924.

Manjunath, H., Zhang, H., Rehfeld, F., Han, J., Chang, T.-C., and Mendell, J. T. (2019). Suppression of Ribosomal Pausing by eIF5A Is Necessary to Maintain the Fidelity of Start Codon Selection. *Cell Rep.* 29, 3134-3146.e6.

doi:10.1016/j.celrep.2019.10.129.

Martella, M., Catalanotto, C., Talora, C., La Teana, A., Londei, P., and Benelli, D. (2020). Inhibition of Eukaryotic Translation Initiation Factor 5A (eIF5A) Hypusination Suppress p53 Translation and Alters the Association of eIF5A to the Ribosomes. *Int. J. Mol. Sci.* 21. doi:10.3390/ijms21134583.

Mathews, M. B., and Hershey, J. W. B. (2015). The translation factor eIF5A and human cancer. *Biochim. Biophys. Acta - Gene Regul. Mech.* 1849, 836–844. doi:10.1016/j.bbagrm.2015.05.002.

Matsumoto, K., Maehashi, K., Ohno, Y., and Inoue, K. (2014). Recent advances in functional graphene biosensors. *J. Phys. D. Appl. Phys.* 47. doi:10.1088/0022-3727/47/9/094005.

McCallum, M., Bassi, J., De Marco, A., Chen, A., Walls, A. C., Di Iulio, J., et al. (2021). SARS-CoV-2 immune evasion by the B.1.427/B.1.429 variant of concern. *Science (80-.).*, eabi7994. doi:10.1126/science.abi7994.

Mehta, P. K., and Griendling, K. K. (2007). Angiotensin II cell signaling: physiological and pathological effects in the cardiovascular system. *Am. J. Physiol. Cell Physiol.* 292, C82-97. doi:10.1152/ajpcell.00287.2006.

Mehta, P., McAuley, D. F., Brown, M., Sanchez, E., Tattersall, R. S., and Manson, J. J. (2020). COVID-19: consider cytokine storm syndromes and immunosuppression. *Lancet (London, England)* 395, 1033–1034. doi:10.1016/S0140-6736(20)30628-0.

Melis, N., Rubera, I., Cougnon, M., Giraud, S., Mograbi, B., Belaid, A., et al. (2017). Targeting eIF5A Hypusination Prevents Anoxic Cell Death through

Mitochondrial Silencing and Improves Kidney Transplant Outcome. *J. Am. Soc. Nephrol.* 28, 811–822. doi:10.1681/ASN.2016010012.

Melnikov, S., Mailliot, J., Shin, B. S., Rigger, L., Yusupova, G., Micura, R., et al. (2016). Crystal Structure of Hypusine-Containing Translation Factor eIF5A Bound to a Rotated Eukaryotic Ribosome. *J. Mol. Biol.* 428, 3570–3576. doi:10.1016/j.jmb.2016.05.011.

Mohapatra, R. K., Kuppili, S., Kumar Suvvari, T., Kandi, V., Behera, A., Verma, S., et al. (2022). SARS-CoV-2 and its variants of concern including Omicron: looks like a never ending pandemic. *Chem. Biol. Drug Des.* doi:10.1111/cbdd.14035.

Mollarasouli, F., Zare-Shehneh, N., and Ghaedi, M. (2022). A review on corona virus disease 2019 (COVID-19): current progress, clinical features and bioanalytical diagnostic methods. *Mikrochim. Acta* 189, 103. doi:10.1007/s00604-022-05167-y.

Motta, S., Minici, C., Corrada, D., Bonati, L., and Pandini, A. (2018). Ligand-induced perturbation of the HIF-2 α : ARNT dimer dynamics. *PLoS Comput. Biol.* 14, e1006021.

Mu, L., Chang, Y., Sawtelle, S. D., Wipf, M., Duan, X., and Reed, M. A. (2015). Silicon Nanowire Field-Effect Transistors—A Versatile Class of Potentiometric Nanobiosensors. *IEEE Access* 3, 287–302. doi:10.1109/ACCESS.2015.2422842.

Nakanishi, S., and Cleveland, J. L. (2016). Targeting the polyamine-hypusine circuit for the prevention and treatment of cancer. *Amino Acids* 48, 2353–2362. doi:10.1007/s00726-016-2275-3.

Navarre, W. W., Zou, S. B., Roy, H., Xie, J. L., Savchenko, A., Singer, A., et al. (2010). PoxA, yjeK, and elongation factor P coordinately modulate virulence and drug resistance in Salmonella enterica. *Mol. Cell* 39, 209–221. doi:10.1016/j.molcel.2010.06.021.

Nishimura, K., Bum Lee, S., Hwan Park, J., and Hee Park, M. (2010). Essential role of eIF5A-1 and deoxyhypusine synthase in mouse embryonic development. *Amino Acids* 48, 1–6. doi:10.1097/MPG.0b013e3181a15ae8.Screening.

Nishimura, K., Ohki, Y., Fukuchi-Shimogori, T., Sakata, K., Saiga, K., Beppu, T., et al. (2002). Inhibition of cell growth through inactivation of eukaryotic translation initiation factor 5A (eIF5A) by deoxyspergualin. *Biochem. J.* 363, 761–768. doi:10.1042/0264-6021:3630761.

Nolting, B. (2013). Linker technologies for antibody-drug conjugates. *Methods Mol. Biol.* 1045, 71–100. doi:10.1007/978-1-62703-541-5_5.

Park, J. H., Wolff, E. C., Folk, J. E., and Park, M. H. (2003). Reversal of the deoxyhypusine synthesis reaction: Generation of spermidine or homospermidine from deoxyhypusine by deoxyhypusine synthase. *J. Biol. Chem.* 278, 32683–32691. doi:10.1074/jbc.M304247200.

Park, M. H., Cooper, H. L., and Folk, J. E. (1981). Identification of hypusine, an unusual amino acid, in a protein from human lymphocytes and of spermidine as its biosynthetic precursor. *Proc. Natl. Acad. Sci. U. S. A.* 78, 2869–2873. doi:10.1073/pnas.78.5.2869.

Park, M. H., and Wolff, E. C. (2018a). Hypusine, a polyamine-derived amino acid critical for eukaryotic translation. *J. Biol. Chem.* 293, 18710–18718.

doi:10.1074/jbc.TM118.003341.

Park, M. H., and Wolff, E. C. (2018b). Hypusine, a polyamine-derived amino acid critical for eukaryotic translation. *J. Biol. Chem.* 293, 18710–18718. doi:10.1074/jbc.TM118.003341.

Park, M. H., and Wolff, E. C. (2018c). Hypusine, a polyamine-derived amino acid critical for eukaryotic translation. *J. Biol. Chem.* 293, 18710–18718. doi:10.1074/jbc.TM118.003341.

Parreiras-e-Silva, L. T., Luchessi, A. D., Reis, R. I., Oliver, C., Jamur, M. C., Ramos, R. G. P., et al. (2010). Evidences of a role for eukaryotic translation initiation factor 5A (eIF5A) in mouse embryogenesis and cell differentiation. *J. Cell. Physiol.* 225, 500–505. doi:10.1002/jcp.22229.

Parrinello, M., and Rahman, A. (1981). Polymorphic transitions in single crystals: A new molecular dynamics method. *J. Appl. Phys.* 52, 7182–7190. doi:10.1063/1.328693.

Pegg, A. E., and McCann, P. P. (1982). Polyamine metabolism and function. *Am. J. Physiol.* 243, C212-21. doi:10.1152/ajpcell.1982.243.5.C212.

Peil, L., Starosta, A. L., Virumäe, K., Atkinson, G. C., Tenson, T., Remme, J., et al. (2012). Lys34 of translation elongation factor EF-P is hydroxylated by YfcM. *Nat. Chem. Biol.* 8, 695–697. doi:10.1038/nchembio.1001.

Pelechano, V., and Alepuz, P. (2017). eIF5A facilitates translation termination globally and promotes the elongation of many non polyproline-specific tripeptide sequences. *Nucleic Acids Res.* 45, 7326–7338. doi:10.1093/nar/gkx479.

Pettersen, E. F., Goddard, T. D., Huang, C. C., Couch, G. S., Greenblatt, D. M., Meng, E. C., et al. (2004). UCSF Chimera--a visualization system for exploratory research and analysis. *J. Comput. Chem.* 25, 1605–1612. doi:10.1002/jcc.20084.

Prunetti, L., Graf, M., Blaby, I. K., Peil, L., Makkay, A. M., Starosta, A. L., et al. (2016). Deciphering the Translation Initiation Factor 5A Modification Pathway in Halophilic Archaea. *Archaea* 2016. doi:10.1155/2016/7316725.

Puleston, D. J., Buck, M. D., Klein Geltink, R. I., Kyle, R. L., Caputa, G., O'Sullivan, D., et al. (2019). Polyamines and eIF5A Hypusination Modulate Mitochondrial Respiration and Macrophage Activation. *Cell Metab.* 30, 352-363.e8. doi:10.1016/j.cmet.2019.05.003.

Roda, A., Cavalera, S., Di Nardo, F., Calabria, D., Rosati, S., Simoni, P., et al. (2021). Dual lateral flow optical/chemiluminescence immunosensors for the rapid detection of salivary and serum IgA in patients with COVID-19 disease. *Biosens. Bioelectron.* 172, 112765. doi:10.1016/j.bios.2020.112765.

Saini, P., Eyler, D. E., Green, R., and Dever, T. E. (2009). Hypusine-containing protein eIF5A promotes translation elongation. *Nature* 459, 118–121. doi:10.1038/nature08034.

Schmidt, C., Becker, T., Heuer, A., Braunger, K., Shanmuganathan, V., Pech, M., et al. (2016). Structure of the hypusinylated eukaryotic translation factor eIF-5A bound to the ribosome. *Nucleic Acids Res.* 44, 1944–1951. doi:10.1093/nar/gkv1517.

Schuller, A. P., Wu, C. C.-C., Dever, T. E., Buskirk, A. R., and Green, R. (2017). eIF5A Functions Globally in Translation Elongation and Termination. *Mol. Cell* 66, 194-205.e5. doi:10.1016/j.molcel.2017.03.003.

Schultz, C. R., Geerts, D., Mooney, M., El-Khawaja, R., Koster, J., and Bachmann, A. S. (2018a). Synergistic drug combination GC7/DFMO suppresses hypusine/spermidine-dependent eIF5A activation and induces apoptotic cell death in neuroblastoma. *Biochem. J.* 475, 531–545. doi:10.1042/BCJ20170597.

Schultz, C. R., Geerts, D., Mooney, M., El-Khawaja, R., Koster, J., and Bachmann, A. S. (2018b). Synergistic drug combination GC7/DFMO suppresses hypusine/spermidine-dependent eIF5A activation and induces apoptotic cell death in neuroblastoma. *Biochem. J.* 475, 531–545. doi:10.1042/BCJ20170597.

Seo, G., Lee, G., Kim, M. J., Baek, S. H., Choi, M., Ku, K. B., et al. (2020). Rapid Detection of COVID-19 Causative Virus (SARS-CoV-2) in Human Nasopharyngeal Swab Specimens Using Field-Effect Transistor-Based Biosensor. *ACS Nano* 14, 5135–5142. doi:10.1021/acsnano.0c02823.

Shang, J., Wan, Y., Luo, C., Ye, G., Geng, Q., Auerbach, A., et al. (2020a). Cell entry mechanisms of SARS-CoV-2. *Proc. Natl. Acad. Sci. U. S. A.* 117, 11727–11734. doi:10.1073/pnas.2003138117.

Shang, J., Ye, G., Shi, K., Wan, Y., Luo, C., Aihara, H., et al. (2020b). Structural basis of receptor recognition by SARS-CoV-2. *Nature* 581, 221–224. doi:10.1038/s41586-020-2179-y.

Shiba, T., Mizote, H., Kaneko, T., Nakajima, T., and Kakimoto, Y. (1971).

Hypusine, a new amino acid occurring in bovine brain. Isolation and structural determination. *Biochim. Biophys. Acta* 244, 523–531. doi:10.1016/0304-4165(71)90069-9.

Shrestha, L. B., Tedla, N., and Bull, R. A. (2021). Broadly-Neutralizing Antibodies Against Emerging SARS-CoV-2 Variants. *Front. Immunol.* 12, 752003. doi:10.3389/fimmu.2021.752003.

Silvestrini, L., Belhaj, N., Comez, L., Gerelli, Y., Lauria, A., Libera, V., et al. (2021). The dimer-monomer equilibrium of SARS-CoV-2 main protease is affected by small molecule inhibitors. *Sci. Rep.* 11, 9283. doi:10.1038/s41598-021-88630-9.

Slowinska, B., Zagulska, S., Wilson, R. C., Staiano-coico, L., Hanauske, A., Mccaffrey, T., et al. (1995). Detection of a sub-set of polysomal mRNAs associated with modulation of hypusine formation at the G1-S boundary t Proposal of a role for eIF-5A in onset of D N A replication. *FEBS Lett.* 366, 92–98.

SUNHWAN JO, TAEHOON KIM, VIDYASHANKARA G. IYER, W. I. (2012). CHARMM-GUI: A Web-Based Graphical UserInterface for CHARMM. *J. Comput. Chem.* 32, 174–182. doi:10.1002/jcc.20945.

Tauc, M., Cougnon, M., Carcy, R., Melis, N., Hauet, T., Pellerin, L., et al. (2021a). The eukaryotic initiation factor 5A (eIF5A1), the molecule, mechanisms and recent insights into the pathophysiological roles. *Cell Biosci.* 11, 1–23. doi:10.1186/s13578-021-00733-y.

Tauc, M., Cougnon, M., Carcy, R., Melis, N., Hauet, T., Pellerin, L., et al. (2021b). The eukaryotic initiation factor 5A (eIF5A1), the molecule,

mechanisms and recent insights into the pathophysiological roles. *Cell Biosci.* 11, 219. doi:10.1186/s13578-021-00733-y.

Tegally, H., Wilkinson, E., Giovanetti, M., Iranzadeh, A., Fonseca, V., Giandhari, J., et al. (2020). Emergence and rapid spread of a new severe acute respiratory syndrome-related coronavirus 2 (SARS-CoV-2) lineage with multiple spike mutations in South Africa. *medRxiv* 2. doi:10.1101/2020.12.21.20248640.

Thévenot, D. R., Toth, K., Durst, R. A., and Wilson, G. S. (2001). Electrochemical biosensors: Recommended definitions and classification. *Biosens. Bioelectron.* 16, 121–131. doi:10.1016/S0956-5663(01)00115-4.

Thodkar, K., Cazade, P. A., Bergmann, F., Lopez-Calle, E., Thompson, D., and Heindl, D. (2021). Self-Assembled Pyrene Stacks and Peptide Monolayers Tune the Electronic Properties of Functionalized Electrolyte-Gated Graphene Field-Effect Transistors. *ACS Appl. Mater. Interfaces*. doi:10.1021/acsami.0c18485.

Tian, B., Gao, F., Fock, J., Dufva, M., and Hansen, M. F. (2020). Homogeneous circle-to-circle amplification for real-time optomagnetic detection of SARS-CoV-2 RdRp coding sequence. *Biosens. Bioelectron.* 165, 112356. doi:10.1016/j.bios.2020.112356.

Tong, Y., Park, I., Hong, B. S., Nedyalkova, L., Tempel, W., and Park, H. W. (2009). Crystal structure of human eIF5A1: Insight into functional similarity of human eIF5A1 and eIF5A2. *Proteins Struct. Funct. Bioinforma.* 75, 1040–1045. doi:10.1002/prot.22378.

Tubiana, J., Xiang, Y., Fan, L., Wolfson, H. J., Chen, K., Schneidman-Duhovny,

D., et al. (2022). Reduced antigenicity of Omicron lowers host serologic response. *bioRxiv Prepr. Serv. Biol.* doi:10.1101/2022.02.15.480546.

Turpaev, K., Krizhanovskii, C., Wang, X., Sargsyan, E., Bergsten, P., and Welsh, N. (2019). The protein synthesis inhibitor brusatol normalizes high-fat diet-induced glucose intolerance in male C57BL/6 mice: role of translation factor eIF5A hypusination. *FASEB J. Off. Publ. Fed. Am. Soc. Exp. Biol.* 33, 3510–3522. doi:10.1096/fj.201801698R.

Turpaev, K. T. (2018). Translation Factor eIF5A, Modification with Hypusine and Role in Regulation of Gene Expression. eIF5A as a Target for Pharmacological Interventions. *Biochem.* 83, 863–873. doi:10.1134/S0006297918080011.

Udugama, B., Kadhiresan, P., Kozlowski, H. N., Malekjahani, A., Osborne, M., Li, V. Y. C., et al. (2020). Diagnosing COVID-19: The Disease and Tools for Detection. *ACS Nano* 14, 3822–3835. doi:10.1021/acsnano.0c02624.

Umland, T. C., Wolff, E. C., Park, M. H., and Davies, D. R. (2004). A new crystal structure of deoxyhypusine synthase reveals the configuration of the active enzyme and of an enzyme·NAD·inhibitor ternary complex. *J. Biol. Chem.* 279, 28697–28705. doi:10.1074/jbc.M404095200.

V'kovski, P., Kratzel, A., Steiner, S., Stalder, H., and Thiel, V. (2021). Coronavirus biology and replication: implications for SARS-CoV-2. *Nat. Rev. Microbiol.* 19, 155–170. doi:10.1038/s41579-020-00468-6.

Vu, C.-A., and Chen, W.-Y. (2019). Field-Effect Transistor Biosensors for Biomedical Applications: Recent Advances and Future Prospects. *Sensors (Basel).* 19. doi:10.3390/s19194214.

Walls, A. C., Park, Y.-J., Tortorici, M. A., Wall, A., McGuire, A. T., and Veesler, D. (2020). Structure, Function, and Antigenicity of the SARS-CoV-2 Spike Glycoprotein. *Cell* 181, 281-292.e6. doi:10.1016/j.cell.2020.02.058.

Wan, Y., Shang, J., Graham, R., Baric, R. S., and Li, F. (2020). Receptor Recognition by the Novel Coronavirus from Wuhan: an Analysis Based on Decade-Long Structural Studies of SARS Coronavirus. *J. Virol.* 94. doi:10.1128/JVI.00127-20.

Wang, F., Guan, X., and Xie, D. (2013). Roles of eukaryotic initiation factor 5A2 in human cancer. *Int. J. Biol. Sci.* 9, 1013–1020. doi:10.7150/ijbs.7191.

Wątor, E., Wilk, P., and Grudnik, P. (2020). Half way to hypusine—Structural basis for substrate recognition by human deoxyhypusine synthase. *Biomolecules* 10, 10–12. doi:10.3390/biom10040522.

Wolff, E. C., Kang, K. R., Kim, Y. S., and Park, M. H. (2007). Posttranslational synthesis of hypusine: evolutionary progression and specificity of the hypusine modification. *Amino Acids* 33, 341–350. doi:10.1007/s00726-007-0525-0.

Wolff, E. C., Park, M. H., and Folk, J. E. (1990). Cleavage of spermidine as the first step in deoxyhypusine synthesis. The role of NAD+. *J. Biol. Chem.* 265, 4793–4799. doi:10.1016/s0021-9258(19)34042-6.

Wrapp, D., Wang, N., Corbett, K. S., Goldsmith, J. A., Hsieh, C.-L., Abiona, O., et al. (2020). Cryo-EM structure of the 2019-nCoV spike in the prefusion conformation. *Science* 367, 1260–1263. doi:10.1126/science.abb2507.

Yan, R., Zhang, Y., Guo, Y., Xia, L., and Zhou, Q. (2020). Structural basis for the

recognition of the 2019-nCoV by human ACE2. 2762, 1–10. doi:10.1101/2020.02.19.956946.

Yanagisawa, T., Sumida, T., Ishii, R., Takemoto, C., and Yokoyama, S. (2010). A paralog of lysyl-tRNA synthetase aminoacylates a conserved lysine residue in translation elongation factor P. *Nat. Struct. Mol. Biol.* 17, 1136–1143. doi:10.1038/nsmb.1889.

Yang, J., Petitjean, S. J. L., Koehler, M., Zhang, Q., Dumitru, A. C., Chen, W., et al. (2020). Molecular interaction and inhibition of SARS-CoV-2 binding to the ACE2 receptor. *Nat. Commun.* 11. doi:10.1038/s41467-020-18319-6.

Zhang, H., Alsaleh, G., Feltham, J., Sun, Y., Napolitano, G., Riffelmacher, T., et al. (2019). Polyamines Control eIF5A Hypusination, TFEB Translation, and Autophagy to Reverse B Cell Senescence. *Mol. Cell* 76, 110-125.e9. doi:10.1016/j.molcel.2019.08.005.

Zhou, P., Yang, X.-L., Wang, X.-G., Hu, B., Zhang, L., Zhang, W., et al. (2020). A pneumonia outbreak associated with a new coronavirus of probable bat origin. *Nature* 579, 270–273. doi:10.1038/s41586-020-2012-7.

11ACKNOWLEDGEMENT

First, I am extremely grateful to my supervisors, Prof. La Teana and Prof. Di Marino for their invaluable advice, continuous support, and patience during my PhD study. Their immense knowledge and plentiful experience have encouraged me in all the time of my academic research and daily life.

I would also like to thank Dr. Alice Romagnoli and all the Molecular Biology Lab and MaSBiC members for the friendship and for their technical and mental support on my project.

I would like to thank Dr. Stefano Motta, for all the support with computational analyses.

Prof. Ennifar, Dr. Angelita Simonetti and Dr. Stefano Marsi for the big help with the structural part of the project, the advice and their kind help and support that have made my study and life in France a wonderful time.

My gratitude extends to the Department of Informational Engineering and Department of Biomedical Sciences and Public Health for the beautiful collaboration on the COVID-19 biosensor project, especially Dr. Eleonora Pavoni.